C.P. No. 345
(18,657)
A.R.C. Technical Report

C.P. No. 345
(18,657)
A.R.C. Technical Report

MINISTRY OF SUPPLY

AERONAUTICAL RESEARCH COUNCIL

CURRENT PAPERS

Some Further Jet Flap Experiments

By

N. A. Dimmock

LONDON . HER MAJESTY'S STATIONERY OFFICE

1957

NINE SHILLINGS NET

C.P. No. 345

ADDENDUM

For Reference 2, reference may be made to:

(a) B. S. Stratford — Early thoughts on the jet flap. The Aeronautical Quarterly, Vol. VII. February, 1956.

(b) I. M. Davidson — The Jet Flap. The Journal of the R. Ae. Soc. January, 1956.

See also:

B. S. Stratford — Mixing and the jet flap. The Aeronautical Quarterly, Vol. VII. May, 1956.

B. S. Stratford — A further discussion on mixing and the jet flap. The Aeronautical Quarterly, Vol. VII. August, 1956.

DB 62270/2/R.72 301 7/57 R

U.D.C. No.533.691.152:533.691.13

C.P. No. 345

NATIONAL GAS TURBINE ESTABLISHMENT

Some further jet flap experiments

- by -

N. A. Dimmock

SUMMARY

This paper, which may be considered as an addendum to the N.G.T.E. Report No. R.175[1], records the results of tests on the same two-dimensional aerofoil which was used for the earlier work and which had a 12.5 per cent thick elliptical cross section with a narrow full span jet slot. This time, however, the jet deflection is 58.1° from the chord line. In addition to the measurement of the forces and moments acting on the model, the flow pattern in the vicinity of the aerofoil was revealed with smoke filaments and was recorded photographically. A comparison with the theory of Reference 2 is drawn where appropriate and additional support is given to the thrust hypothesis. A check on the effects of Reynolds number variation and of the addition of transition wires to the model confirmed the results of the previous experiments, whilst the influence of ground proximity on the lift, centre of lift position and the thrust was investigated and found to be substantial, although a reason is suggested why these results might be pessimistic.

CONTENTS

TABLES

APPENDICES

ILLUSTRATIONS

Fig. No.	Title
1(a)	The model - external
1(b)	View showing the construction of the model
2	Section of model
3	Arrangement of wind tunnel
4	Working section with model
5	The thrust balance
6	Variation of jet slot
7	The smoke generator
8	Variation of jet deflection angle with jet total pressure
9	Thrust calibration curves for model with jet deflected 58.1°
10(a)	Flow pattern at C_J = 0.10
10(b)	Flow pattern at C_J = 0.30
11(a)	Flow pattern at C_J = 0.50
11(b)	Flow pattern at C_J = 0.75
12(a)	Flow pattern at C_J = 1.50
12(b)	Flow pattern at C_J = 3.0
13	Pressure distribution at zero incidence ($R_N = 1.28 \times 10^5$)
14	Pressure distribution at zero incidence (C_J = 0.30; (a) $R_N = 1.28 \times 10^5$ and (b) $R_N = 4.25 \times 10^5$)
15	Pressure distribution at zero incidence ($R_N = 1.28 \times 10^5$)
16	Pressure distribution at zero incidence ($R_N = 1.28 \times 10^5$)
17	Pressure distribution at zero incidence ($R_N = 1.28 \times 10^5$)

ILLUSTRATIONS (Cont'd)

ILLUSTRATIONS (Cont'd)

1.0 Introduction

This paper completes the record of the experimental results obtained from a series of simple jet flap model aerofoils and thereby extends the N.G.T.E. Report No. R.175[1]. In addition to tests similar in scope to those already reported, the flow pattern around the aerofoil, having a 60° flap, is illustrated with photographs of smoke filaments; from tests at the same Reynolds numbers information is provided which can be related directly to the effects shown in the illustrations.

2.0 The equipment

2.1 General remarks

Whilst a full description of the model aerofoil, the wind tunnel, the thrust balance and the compressed air supply will be found in Reference 1, a recapitulation is afforded by Figures 1 to 5, and Figure 6 shows the variation, along the span, of the width of the jet slot. Two modifications were made to the wind tunnel before the testing of the 60° model, the first being the removal of bulges in the side walls at the outlet from the contraction, so that the thickness of the boundary layer on the working section walls in the region of the aerofoil leading edge was reduced, at a tunnel speed of 100 ft/sec, from about 0.75 in. to about 0.56 in. The latter value agrees quite well with an estimate of 0.53 in. obtained by assuming that transition to a turbulent boundary layer occurs 7 in. upstream from the join of the contraction and working section, as was indicated by an inflection in the curve of normal pressure measured by static holes spaced along the centre of the side walls of the contraction and the first part of the working section. The other modification was the replacement of the two large transparent plastic panels, in either side of the working section, by plates of aluminium alloy, one being kept substantially flat and rigid by the addition of tee-section members and the other having a small window framing the aerofoil. This window was of plastic for general purposes and of plate glass for photography. The screw adjusters (Figure 4) for setting the clearances between the model and the tunnel walls were retained on this side only.

2.2 The apparatus for flow visualization

A simple smoke generator (similar in principle to that developed by Preston and Sweeting[3]) was constructed in which kerosine was boiled and the jet of vapour condensed by two cold air jets to give a dense mist (Figure 7). The "smoke" entered the tunnel through a vertical probe of streamlined tubing carrying ten, short tappings of 2 mm diameter tubing. By trial and error it was found that the most distinct smoke filaments resulted when these tappings were 'L' shaped and inserted in the side of the main tube so that the exit of the tapping pointed downwind, although an exact alignment downwind was less satisfactory than with the whole rake set at a few degrees of incidence.

The smoke trails were illuminated by two 250 watt aircraft landing lamps with their beams directed along the wind tunnel working section from the top and bottom of its open end, and the electrical traversing mechanism of the lamps was used to cover the field of view adequately during a total photographic exposure of 1 sec at an aperture of f.8. The exposure was usually divided into two or sometimes three periods, thus permitting the adjustment of the lighting in between to show each individual flow pattern to its best advantage, although the overall time for the process was kept short - about 3 sec. With the observation window of the wind tunnel fitted in the side adjacent to the manometers and controls, a lack of space prevented the use of a distant camera and telephoto lens combination. Thus the effect of perspective was objectionable

but unavoidable, although it was diminished by the use of a surface silvered mirror, which increased the lens-object distance to about 7 ft - a limit imposed by the size of the mirror and the maximum dimension from the wind tunnel to the wall of the room. The arrangement of the smoke filaments in a plane only about one third of the span from the window gave some further improvement. A 12 in. telephoto lens was used at f.8 with a 5 in. x 4 in. plate camera and a fast panchromatic emulsion was necessary to keep the exposure time reasonably brief.

3.0 The calibration of jet angle and thrust

As for the earlier models[1], the jet angle, θ, was found by using fine strands of cotton affixed to the trailing edge close to and on either side of the jet slot; the model was then turned until a reference line scribed on the tunnel wall bisected the (small) angle between the strands, which took up a position near the edge of the jet boundary. The angle of incidence of the aerofoil, read off a protractor fixed to one of the model support arms, then gave the jet deflection angle directly. In the early calibrations, before the flow visualisation work, the jet angle was accepted as being 55.4°, but there was some doubt about this. Another calibration, made before the main tests were started, gave an average value of $\theta = 58.1^{\circ}$, although it appeared that the angle varied with the jet total pressure. A further check on this aspect produced the result illustrated in Figure 8 which shows that this variation was small. Some doubt remained, however, since the low values of θ seemed to be due to the large weight/drag ratio of the tufts with small jet flows (remember that the model was inverted), whilst with large jet flows, entrainment effects could give erroneous, large values of jet angle.

In computing the force and moment coefficients etc., the apparent variation of θ was ignored, a constant value of 58.1° being taken and the results of the earlier tests being corrected accordingly.

The jet total pressure was measured at a point within the body of the aerofoil and the corresponding jet reaction, J, was determined from a balance measurement of thrust with the model at a negative angle of incidence equal to the jet deflection angle, together with a measurement of the pressure force arising from the airflow induced by the jet[1]. Thus, for the first and second calibrations the model was set at -55.4° incidence, but at $\alpha = -58.1^{\circ}$ for the final measurements. The thrust calibration curves are shown in Figure 9 where it can be seen that the thrust increased by about 3.5 per cent between the first and final calibrations, this discrepancy being far more than the 0.1 per cent which would result from the change in calibration angle from one test to the other. It was considered unlikely that the thrust measurements were unreliable and so, although a constant jet angle was assumed for all tests, the jet reaction appropriate to the groups of tests was used, since it seemed probable that the trailing edge piece had been deformed by internal pressure sufficiently to cause the change in thrust. (Note in Reference 1 that a similar effect was found with the 0° model trailing edge, but to a greater extent and in the opposite sense).

A further check on the jet angle was made by measuring the thrust for several values of jet total pressure with the model at zero incidence, by adding the pressure drag correction, and then dividing the sum by the corrected jet reaction obtained from the final calibration. While the result is added to Figure 8, an inversion of this check is shown in Figure 9.

4.0 Flow patterns and corresponding tests at zero incidence

A tunnel speed of 30 ft/sec permitted reasonable delineation of the ten smoke trails, although the low value for the chordal Reynolds number, R_N, of 1.28×10^5 suggested that the flow pattern could not be compared directly with the performance measured at the higher Reynolds numbers of the "standard" test. For this reason pressure distributions and thrusts were measured at all values of the jet coefficient, C_J, at which the flow visualisation photographs had been taken - and under nominally identical conditions, the model having no trip wires fitted. (See Section 5.2 for the effect of trip wires and Reynolds number variation). Six of the flow visualisation photographs are reproduced in Figures 10, 11 and 12 and they illustrate the following points:

Figure 10a	The very rapid turning of the small jet sheet.
Figure 10b	Shows clearly the curvature of the jet and adjacent mainstream.
Figure 11a	Shows the onset of a separation bubble at the leading edge,
and in Figure 11b	A longer bubble is apparent, as is the more rapid entrainment of the mainstream beneath and close to the aerofoil.
Figure 12a	Very large bubble with rapid entrainment of the mainstream and unsteady flow behind the model.
Figure 12b	Separation bubble almost 100 per cent of the chord. Very large displacement of the mainstream flow. Front stagnation point at about 25 per cent chord from the leading edge. Sink effect drawing mainstream towards the jet slot before entrainment.

It should be noted that the smoke probe was fixed so that, with 'no blow' the smoke filament second from the top was divided by the aerofoil. The corresponding pressure distributions will be found amongst those shown in Figures 13 to 18, whilst Figure 14 affords a comparison of the pressure distributions at a constant value of C_J obtained for the model without trip wires at two values of R_N and, at the higher Reynolds number, with trip wires. Further reference to these pressure distributions will be made in Section 5.2. The coefficients of both the total and the pressure lift, C_{L_0} and C_{L_p} are plotted in Figure 19, the magnification factor, γ_0, in Figure 20 and the centre of lift position in Figure 21. The jet shape factor, k, and the measured thrust are plotted in Figures 24 and 38. (See Appendix I and Figure 48 for nomenclature).

5.0 "Standard" tests at zero incidence

5.1 Lift

As in the earlier experiments[1] the total lift, L_0, was obtained from the sum of the vertical component of the jet thrust, $J \sin \theta$, and the graphical integration of the chordwise pressure distribution, L_p. Nomenclature is given in Appendix I and Figure 48, whilst all the working formulae are collected together in Appendix II.

Figure 22 shows both the total and pressure lift coefficients, C_{L_0} and C_{L_p}, plotted against the jet coefficient C_J, whilst the values of the chordal

Reynolds number are added since, with a jet total pressure limited by the strength of the model to 15 p.s.i. gauge, jet coefficients above 0.50 could be obtained only by reducing the tunnel speed. Also included for comparison are the coefficients for the test at a Reynolds number of 1.28×10^5 without transition wires (Section 4.0). The variation with C_J of the magnification factor, M_o, and the jet shape factor, k, is shown in Figures 23 and 24, and the significance of the latter is mentioned briefly in Reference 1, whilst its experimental value was obtained through Equations (2) and (5) of Appendix II and the known values of C_L and C_J.

A representative selection of pressure distribution curves is given in Figures 25 to 31 some of these being used to illustrate certain Reynolds number effects discussed in Section 5.2.

5.2 Some Reynolds number effects

The "standard" tests were made with a transition wire 0.034 in. diameter fitted at a station 0.82 chord from the leading edge on both the upper and the lower surface, as was found effective in the earlier tests on the 30° model[1]. As before, the Reynolds number, R_N, was constant at 4.25×10^5 until a jet coefficient of 0.50 was reached, when the pressure within the model was the safe maximum and a further increase in C_J could be obtained only by decreasing the tunnel speed. A comparative test at $R_N = 4.25 \times 10^5$ but without the trip wires was also made up to $C_J = 0.07$, whilst additional data resulted from the test corresponding to the flow visualisation conditions at a (constant) Reynolds number of 1.28×10^5.

The argument for the interpretation of these results is given at length in Reference 1 and will not be repeated here, except for a summary of the main points of agreement or difference.

Agreement

(i) Indication of laminar separation near the trailing edge, without trip wires, until the peak pressure coefficient, C_p, near the leading edge reached about -1.0. See Figure 25, where the normal pressure decreases at the trailing edge in (a) and (b), but in (c) shows a recovery.

(ii) Addition of trip wires near the trailing edge gave this pressure recovery at low values of C_J - Figure 26(a), (b) and (c) - and gave larger values of C_{L_o}, M_o and k until C_J reached between 0.05 and 0.07 - Figures 32, 33 and 34 - corresponding to a C_p value at the leading edge of between -1.0 and -1.25. Hence,

(iii) the deduction that transition to a turbulent boundary layer occurred near the leading edge when a C_p of -1.0 to -1.2 was obtained in that region, although in these tests no inflection in the pressure distribution curve could be detected (although see (v)).

(iv) Leading edge separation occurred after a C_p of -7.5 was attained. This was a higher suction peak than the -6.7 obtained in the earlier tests - a result which may be due to the thinner boundary layer on the tunnel walls (see Section 2.1).

Differences

(v) At a chordal Reynolds number of only 1.28×10^5 the C_p required for transition near the leading edge appeared to be above -2.5 - Figures 13(a) and (b) - but an indication that transition had occurred at $C_J = 0.30$ - Figure 14(a) - was afforded by the marked inflection in the curve at about 4 per cent chord[1], 4 and 5.

(vi) Leading edge separation at $R_N = 1.28 \times 10^5$ occurred at $0.30 < C_J < 0.50$, when the highest recorded suction was about $C_p = -4.0$. Although it is possible that a higher suction peak was reached in between the two values of C_J at which pressure readings were taken, it is not surprising that, at this low Reynolds number, separation should have taken place at the low value.

From general interest, a few measurements were made of the "no blow" drag on the model fitted with trip wires and covering a range of tunnel speeds from 35 to 100 f.p.s. The result is shown - in coefficient form - in Figure 36, with some points added from the other tests without trip wires.

5.3 Centre of lift

The first moment of area of the pressure distribution curves about the mid-chord point was obtained by graphical integration, and the addition of the moment due to the jet reaction gave the total pitching moment on the aerofoil and hence the position of the centre of lift.

As in the tests on the 30° model[1] only sample plots of pressure against thickness (y) were made in order to satisfy the assumption that the contribution by these to the total pitching moment was small enough to be neglected, these plots also being used for the pressure thrust computation - Section 6.0.

The errors introduced by the neglect of the "y" pressure moment varied from 1.5 per cent of the sum of the other two moments at $C_J = 0.15$, to 0.23 per cent at $C_J = 1.50$, but this represents a fairly constant rearward shift of the centre of lift position of only 0.04 per cent of the chord.

The position of the centre of lift is shown plotted against C_J in Figure 37 together with the theoretical curve given by Equation (7) in Appendix II, the value taken for k being that obtained experimentally as described in Section 5.1.

6.0 Thrust

The thrust and drag of a jet flapped aerofoil with a deflected jet is discussed fully in References 2 and 6, and briefly in Reference 1. The net thrust experienced by the model was measured by the balance for both the "standard" test and that at $R_N = 1.28 \times 10^5$, whilst the pressure thrust was computed for the more interesting values of C_J, i.e. those on either side of the point of leading edge separation for the "standard" test only, the horizontal component of the jet reaction being added to give the total thrust.

Figure 38 shows a plot of C_{T_0}/C_J against C_J, with the horizontal component of the jet reaction indicated by a line drawn at $C_{T_0}/C_J = \cos\theta$. Here, C_{T_0} is defined as,

$$C_{T_0} = \frac{\text{measured thrust at zero incidence}}{\frac{1}{2}\rho U_0^2 \times (\text{wing area})}$$

It can be seen that the effective thrust increased rapidly as the jet coefficient rose to several times the "no blow" drag coefficient, C_{D_0}, then increased more gradually but still quite steeply until separation occurred at the leading edge - at $0.30 < C_J < 0.50$ for the test at $R_N = 1.28 \times 10^5$ and at $0.50 < C_J < 0.75$ for the "standard" test, although in this instance the Reynolds number also changed here. In both tests net thrusts greater than $J \cos \theta$ were measured by the balance whilst the maximum pressure thrust from the static pressure measurements realised more than half the amount nominally possible. An alternative method of presentation is adopted in Figure 39 where the effective drag coefficient, $C_{D_{eff}}$, given by $C_{D_{eff}} = C_J - C_{T_0}$ is plotted against C_J for all the models so far tested.

It should be remembered that the measurements giving C_{T_0} included all the drag on the model which, for the results obtained from pressure plotting, may be taken as

(i) Form drag.

(ii) Jet drag or sink effect[1], D and 6.

(iii) Part of the induced drag due to the boundary layer on the tunnel walls.

In addition the balance measurements contained

(iv) All the induced drag of (iii) plus that due to the end clearances of about 0.05 in. necessary for the free movement of the model. This effect could be largely due to the large lift coefficients and the small aspect ratio of 1.50.

(v) Skin friction

7.0 Lift at incidence

The total lift on the aerofoil at incidence was taken as the sum of the (pressure force in the direction y).cos α and the (jet reaction).sin $(\theta + \alpha)$, - Figure 48 - the very small component, (pressure force in the direction x).sin α being neglected to save time in plotting and computation. The resulting values of the lift coefficient, C_L, are plotted against incidence in Figure 40, the broken lines being given by

$$C_L = C_{L_0} + \alpha \left[\frac{\partial C_L}{\partial \alpha} \right]_{\alpha = 0}$$

and $\left[\frac{\partial C_L}{\partial \alpha} \right]_{\alpha=0}$ by Equation (8) in Appendix II with $k = 1.0$ since the

equation is insensitive to quite large changes in k. As for the 30° and 90° models[1] the locus of the stalling point $\left(\frac{\partial C_L}{\partial \alpha}\right) = 0$ is a curve, the stalling incidence decreasing with increasing C_J and tending to a minimum of about -1°. Since stalling is due to the failure of the jet to capture the mainstream above the aerofoil, so closing the bubble of separation, it is felt that the stalling, of this model, at such an incidence with high values of C_J, is in part due to the trailing edge shape combined with the position of the jet slot. The latter is well round the "corner" of the trailing edge, as can be seen in Figure 2, the centre line of the jet slot passing through the centre of the trailing edge radius. The theoretical curve for $\left[\frac{\partial C_L}{\partial \alpha}\right]_{\alpha=0}$ is plotted in Figure 41, but the experimental points shown there cover a range of interpretation. For the values of C_J 0.05, 0.20 and 0.50 the straightforward values of $\left[\frac{\partial C_L}{\partial \alpha}\right]_{\alpha=0}$ have been taken but for $C_J > 1.0$ the point $\alpha = o$ is near to or greater than the stalling incidence and the slope of the lift incidence curve would be misleading. The value of $\left[\frac{\partial C_L}{\partial \alpha}\right]_{\alpha=0}$ is plotted as the strict but pessimistic view and gives the lower limit of possible choice; the upper limit represents the determination of $\frac{\partial C_L}{\partial \alpha}$ at an incidence before the occurrence of leading edge separation and is optimistic.

8.0 Longitudinal stability

The pitching moment on the aerofoil at incidence was found by the method described in Section 5.3, neglecting the "y" pressure plot. From a knowledge of the total lift, the pitching moment, the pressure force normal to the chord line and the direct thrust and its line of action, the distances of the aerodynamic centre aft the quarter-chord point, a, and of the centre of lift aft the mid-chord point, d, were found. Figure 42 shows d/c plotted against α, whilst the theoretical curve (Equation 9 Appendix II) and experimental points for $\left[\frac{\partial\left(\frac{d}{c}\right)}{\partial \alpha}\right]_{\alpha=0}$ against C_J are given in Figure 43 with a range of interpretation indicated for points at $C_J > 1.0$ as described in Section 7.0. The movement of the aerodynamic centre with C_J is shown in Figure 37, where the theoretical curve is obtained from Equation (10) of Appendix II and the experimental points are added up to $C_J = 1.0$.

The experimental values were determined from

$$\frac{a}{c} = \left[\frac{\partial C_{m'}}{\partial \alpha}\right]_{\alpha=0} \Big/ \left[\frac{\partial C_L}{\partial \alpha}\right]_{\alpha=0}$$

where $C_{m'}$ is the pitching moment coefficient with respect to the quarter-chord point.

The values of a/c for jet coefficients above 1.0 are unreliable and have not been recorded because stalling occurs close to $\alpha = 0$. In Figure 44 C_m is plotted against C_L, but these results from the 60° model do not support the empirical relationship tentatively suggested in Reference 1, although there is a tendency to follow a similar general form with the decrease in slope roughly proportional to C_J^2 up to $C_J = 1.0$.

9.0 Ground interference effects

The "ground" consisted of a "duralumin" plate, 0.25 in. thick, stiffened at its long edges with angle section members and extending the full length and breadth of the wind tunnel working section, its rounded leading edge being two chords upstream from the model leading edge. Care was taken to ensure that the "ground" was flat and at zero incidence to the undisturbed airflow through the tunnel when in any of its alternative positions. Tests at zero incidence only were made and the thrust was measured by balance at the three smallest clearances, whilst the pressure lift and pitching moments were found by the method described in Sections 5.1 and 5.3 ignoring the moment contribution from the normal pressures plotted against y.

Values of C_{L_o}, d_o/c and $C_{l_o}/C_{T_{o_{co}}}$ are plotted for values of C_J of 0.5, 1.0, 2.0, 3.0 and 4.0 in Figures 45 to 47, where it can be seen that, with a jet deflection of nearly 60° the effect of ground proximity is appreciable. This result, however, is pessimistic since the "ground" was found to be slightly wider in its centre than the 12.0 in. span model, thus spacing the tunnel walls such that the end clearances were even larger than those normally used for balance measurements. Within the available time limit, repeat tests could not be made with an improved "ground", but the three-dimensional effects due to these gaps and the small aspect ratio must have been large. The induced drag, in particular, must have been considerable with the large lift coefficients of this model (nearly twice those of the 30° model[1], which was tested using the same "ground" and clearances without an excessive ground interference effect).

10.0 Conclusions

The results of the concluding experiments with an elliptical aerofoil having a two-dimensional jet deflected 58.1° from the chord line largely confirm those previously reported in Reference 1, and also support the theory proposed in Reference 2 for a simple jet flap aerofoil with or without incidence. The additional evidence is favourable to the thrust hypothesis in that the measured thrust was greater than the reaction component from the deflected jet. The check which was made on the effects of Reynolds number variation and of the addition of transition wires to the model, gave results similar to those reported in Reference 1. The airflow around the aerofoil was traced by smoke streams and photographic records made. They show that, with the aerofoil at zero incidence, the entrainment of the mainstream by the jet is sufficient to cause the former to rejoin the upper surface after separation at the leading edge, even with a full chord separation bubble. Some of these illustrations are presented together with test results obtained at the same Reynolds number. Unexpected difficulties arose in the determination of the derivatives for the model with incidence owing to the early onset of the stall with this aerofoil; an improved section with non-elliptical trailing edge might have delayed this phenomenon. The tentative, empirical relationship between pitching

moment, lift and jet coefficients proposed in Reference 1 has not been confirmed, although the overall pattern of the C_m - C_L curves is similar to those previously obtained. Lastly, the reduction of lift and thrust and the movement aft of the centre of lift position due to ground interference has been measured and found to be substantial at small ground clearances, but for the reason given, this result is thought to be pessimistic.

REFERENCES

No.	Author(s)	Title, etc.
1	N. A. Dimmock	An experimental introduction to the jet flap. C.P. 344. July, 1955.
2*		
3	J. H. Preston N. L. Sweeting	An improved smoke generator for use in the visualisation of airflow, particularly boundary layer flow at high Reynolds numbers. R. & M. 2023. October, 1943.
4	A. Fage	The airflow around a circular cylinder in the region where the boundary layer separates from the surface. R. & M. 1179. August, 1928.
5	A. Fage V. M. Falkner	Further experiments on the flow around a circular cylinder. R. & M. 1369. February, 1931.
6	B. S. Stratford N. A. Dimmock	Mixing and the jet flap. A.R.C. 18,422. October, 1955.

*See addendum sheet

TABLE I

Test results for the 60° model without transition wires and at zero incidence
($\Omega = 58.1°$)

C_J	U_o ft/s	$\frac{R_N}{10^5}$	C_{L_o}	Λ_o	C_{m_o}	d_o/c aft of mid-chord point %	C_{T_o} from pressure distn.	C_{T_o} from balance measurements	
0.0202	100	4.25	0.239	13.98	-0.0065	2.72			
0.0305	↓	↓	0.377	14.55	-0.0094	2.49			
0.0409			0.502	14.50	-0.0104	2.07			
0.0506			0.645	15.00	-0.0104	1.61			
0.0717			0.861	14.16	-0.0235	2.79			
0.1035			1.116	12.69	-0.0309	2.77			
0.1545			1.444	11.02	-0.0453	3.13			
0.2205			1.737	9.53	-0.0745	4.17			
0.3095	100	4.25	2.222	8.43	-0.0969	4.35			
0	100	4.25						-0.0201	
0.020								-0.0066	
0.030								+0.0011	
0.040								0.0095	
0.050								0.0182	
0.070								0.0290	
0.100								0.0464	
0.15								0.0795	
0.20								0.1123	
0.30								0.1812	
0	100	4.25						-0.0203	
0.10	30.0	1.23	0.910	10.72	-0.0140	1.54			Tests corresponding to flow visualisation records
0.20	30.0	1.28	1.487	8.76	-0.0412	2.77			
0.30	30.0	1.28	1.99	7.62	-0.0867	4.35			
0.30	100	4.25	2.165	8.52	-0.0877	4.05			
0.50	30.0	1.28	2.79	6.58	-0.1250	4.40			
0.75	↓	↓	3.50	5.51	-0.198	5.64			
1.00			4.15	4.89	-0.272	6.57			
1.50			5.41	4.24	-0.473	3.74			
2.00			6.65	3.92	-0.690	10.38			
3.00			8.79	3.45	-1.157	12.93			
4.00	↓	↓	10.75	3.17	-1.590	14.80			
5.00	30.0	1.28	12.345	2.91	-2.036	16.47			
0	30.0	1.28						-0.0294	
0.102	↓	↓						+0.0308	
0.207								0.0989	
0.310								0.1675	
0.514								0.2815	
0.776								0.425	
1.043								0.585	
1.553								0.901	
2.043								1.188	
3.090								1.772	
4.10	↓	↓						2.332	
5.15	30.0	1.28						2.879	
0	100	4.25						-0.0199	
0.309	100	4.25						+0.308	
0	100	4.25						-0.0200	

TABLE II

Test results for 60° model at zero incidence and fitted with transition wires

(υ = 58.1°; Transition wires of 0.034 in. dia. fixed at 0.82 chords from L.E. on upper and lower surfaces)

C_J	U_o ft/s	$\frac{RN}{10^5}$	C_{L_o}	$\mathcal{M}_o$	C_{m_o}	d_o/c aft of mid-chord point %	C_{T_o} from pressure distn.	C_{T_o} from balance measurements
0	100	4.25						-0.0165
0.02	↓	↓	0.433	25.45	-0.0070	1.61		-0.0015
0.03			0.548	21.46	-0.0130	2.37		+0.0049
0.04			0.632	18.60	-0.0137	2.17		0.0113
0.05			0.711	16.72	-0.0085	1.20		0.0170
0.07			0.825	13.86	-0.0174	2.11		0.0287
0.10			1.056	12.43	-0.0255	2.42		0.0468
0.15			1.376	10.79	-0.0365	2.65	0.1074	0.0822
0.20			1.666	9.80	-0.0511	3.07	0.147	0.118
0.30			2.123	8.34	-0.0873	4.11	0.223	0.183
0.40	↓	↓	2.520	7.41	-0.1212	4.81	0.305	0.255
0.50	100	4.25	2.900	6.83	-0.146	5.04	0.355	0.324
0.75	80	3.40	3.71	5.82	-0.167	4.51	0.431	0.417
1.00	70	2.98	4.39	5.17	-0.247	5.63	0.564	0.556
1.50	60	2.55	5.62	4.51	-0.435	7.72	0.858	0.845
2.00	50	2.13	6.92	4.07	-0.647	9.35		1.134
2.50	40	1.70	8.26	3.90	-0.877	10.60		1.431
3.00	40	1.70	9.29	3.64	-1.100	11.82		1.703
3.50	40	1.70	10.33	3.47	-1.341	13.00		1.968
4.00	35	1.49	11.25	3.35	-1.565	13.78		2.240

TABLE III

Test results for the 60° model at incidence

(θ = 58.1°. Transition wires of 0.034 in. dia. fixed at 0.82 chords from L.E. on upper and lower surfaces)

C_J	U_o ft/s	$\frac{R_N}{10^5}$	α degrees	C_L	C_m	d/c aft of mid-chord point %
0.05	100	4.25	-10	-0.337	-0.2693	-79.8
			- 5	+0.209	-0.1436	+67.8
			- 2	0.550	-0.0630	11.43
			0	0.711	-0.0035	1.20
			2	0.383	+0.0473	- 5.36
			5	1.137	0.1167	-10.25
			7	1.304	0.1663	-12.70
			9	1.347	0.1771	-13.02
0.20	100	4.25	-10	0.473	-0.334	63.5
			- 5	1.144	-0.190	16.5
			- 2	1.448	-0.103	7.12
			0	1.666	-0.0511	3.07
			2	1.880	-0.0010	0.05
			4	2.042	+0.0752	- 3.71
			6	2.047	0.1027	- 5.02
			8	1.909	0.0525	- 2.74
0.50	100	4.25	-10	1.535	-0.443	27.6
			- 5	2.259	-0.239	12.6
			- 2	2.632	-0.214	8.08
			0	2.900	-0.146	5.04
			2	3.058	-0.0433	1.42
			3	3.041	-0.0280	0.92
			4	3.013	-0.0265	0.88
1.0	70	2.93	-10	2.77	-0.641	22.0
			- 3	3.54	-0.494	13.4
			- 2	4.21	-0.338	8.10
			0	4.39	-0.247	5.63
			1	4.40	-0.245	5.56
			2	4.37	-0.244	5.62
			3	4.22	-0.264	6.29
2.0	50	2.13	-10	4.32	-1.076	21.2
			- 5	6.09	-0.778	12.5
			- 2	6.66	-0.670	10.0
			- 1	6.81	-0.651	9.52
			0	6.92	-0.647	9.35
			1	7.00	-0.687	9.84
4.0	35	1.49	-10	8.40	-1.783	20.0
			- 5	10.15	-1.522	14.7
			- 2	11.07	-1.501	13.5
			0	11.35	-1.565	13.8
			2	9.92	-1.694	17.2
			4	8.50	-1.710	20.4

APPENDIX I

Notation

Fluid properties

Symbol	Quantity
U_o	Undisturbed velocity relative to the aerofoil
p	Local static pressure
p_o	Static pressure of undistrubed mainstream
ρ	Mainstream density (assuming incompressible flow)
ν	Kinematic viscosity

Geometrical

Symbol	Quantity
a	Distance of aerodynamic centre aft of the quarter-chord point
c	Aerofoil chord
d	Distance of centre of total lift aft of the mid-chord point (see also Figure 48)
d_o	As for "d" but with the aerofoil at zero incidence
x and y	Co-ordinates along and perpendicular to the aerofoil chord line (see Figure 48)
α	Angle of incidence (see Figure 48)
η	Analogous flap angle
θ	Jet deflection angle (see Figure 48)
ψ	An analogous flap size parameter

Forces and moments

Symbol	Quantity
J	Total jet reaction or momentum flux at the nozzle (see Figure 48)
L	Total lift (see Figure 48)
L_o	Total lift at zero incidence
L_p	Pressure lift (see Figure 48)
M	Total pitching moment (see Figure 48)
T_o	Measured thrust at zero incidence (see Figure 48)

APPENDIX I (cont'd)

Force and moment coefficients

Symbol	Quantity
C_{D_o}	"No blow" drag coefficient i.e. when $C_J = 0$
C_{D_f}	Skin friction drag coefficient
C_{D_p}	Pressure drag coefficient
$C_{D_{eff}}$	Effective drag coefficient = $C_J - C_{T_o}$
C_{T_o}	Thrust coefficient, aerofoil at zero incidence
C_{D_J}	Jet drag coefficient
C_J	Jet coefficient
C_L	Total lift coefficient
C_{L_o}	Total lift coefficient, aerofoil at zero incidence
C_{L_p}	Pressure lift coefficient
C_m	Pitching moment coefficient (relative to mid-chord point)
C_m'	Pitching moment coefficient (relative to quarter-chord point)

Miscellaneous

Symbol	Quantity
k	The practical jet shape factor
M_o	Magnification factor, aerofoil at zero incidence
π	3.14159.....

APPENDIX II (cont'd)

Lift at incidence (Section 7.0)

$$C_L = C_{L_o} + \alpha \left[\frac{\partial C_L}{\partial \alpha} \right]_{\alpha=o}$$

$$\left[\frac{\partial C_L}{\partial \alpha} \right]_{\alpha=o} = 2\pi \left\{ 1 + \frac{k}{\sqrt{2\pi}} \cdot C_J^{\frac{1}{2}} + \frac{\pi}{24} \cdot \frac{C_J}{k^2} + \frac{1}{24\pi k} \cdot \left(\frac{\pi C_J}{2} \right)^{3/2} \right\} \quad (8)$$

Longitudinal stability (Section 8.0)

$$\frac{d}{c} = \frac{d_o}{c} + \alpha \left[\frac{\partial \left(\frac{d}{c} \right)}{\partial \alpha} \right]_{\alpha=o}$$

where d is measured aft of the mid-chord point.

$$\left[\frac{\partial \left(\frac{d}{c} \right)}{\partial \alpha} \right]_{\alpha=o} = - \frac{\sqrt{\pi/2}}{4k \sin \theta} \cdot \frac{1}{C_J^{\frac{1}{2}}} \left\{ 1 + 0.6\, C_J - 0.4\, C_J^{3/2} \right\} \quad \ldots \quad (9)$$

$(\alpha/6)^2$ Applicable only when α is small as various terms of the order were omitted in the simplification of the expression.

$$\frac{a}{c} = \frac{k}{4} \cdot \frac{C_J^{\frac{1}{2}}}{\sqrt{2\pi}}$$

where a is measured aft of the quarter-chord point.

APPENDIX II

Working formulae[2]

(For notation see Appendix I and Figure 48)

Jet thrust (Section 3.0)

C_J = Jet coefficient

$$= \frac{\text{gross thrust per unit span } (J)}{\frac{1}{2}\rho U_0^2 c} \quad \ldots \quad \ldots \quad \ldots \quad \ldots \quad (1)$$

and in parametric form

$$C_J = \frac{2\psi^2}{\pi} \cdot k^2 \cdot \frac{2}{1 + \cos\psi} \quad \ldots \quad \ldots \quad \ldots \quad \ldots \quad (2)$$

where ψ defines the size of the simple analogous flap and k is a practical jet shape factor given by

$k^2 = \frac{\eta}{\sin\epsilon}$, η being the angle of deflection of an analogous hinged flap on the equivalent thin aerofoil.

Lift at zero incidence (Section 5.1)

$$C_{L_c} = C_{L_p} + C_J \sin\theta \quad \ldots \quad \ldots \quad \ldots \quad \ldots \quad \ldots \quad \ldots \quad (3)$$

$$C_{L_o} = 2k \sin\theta \sqrt{2\pi}\, C_J^{\frac{1}{2}} \left\{ 1 + \frac{\pi}{48} \cdot \frac{C_J}{k^2} + O(C_J^2) \right\} \quad \ldots \quad \ldots \quad (4)$$

$$\eta_o = \frac{\text{Total lift}}{\text{Jet lift}} = \frac{L_o}{J \sin\theta}$$

$$= 2k \left(\frac{2\pi}{C_J}\right)^{\frac{1}{2}} \left\{ 1 + \frac{\pi}{48} \cdot \frac{C_J}{k^2} + O(C_J^2) \right\} \quad \ldots \quad \ldots \quad \ldots \quad (5)$$

Equations (4) and (5) are derived from the parametric forms for C_J (2) and $_cM_o$ given by

$$_cM_o = \frac{\pi}{\psi}\left(1 + \frac{\sin\psi}{\psi}\right) \quad \ldots \quad \ldots \quad \ldots \quad \ldots \quad \ldots \quad \ldots \quad (6)$$

Centre of lift position (Section 5.3)

$$\frac{d_o}{c} = \frac{\pi}{20} \cdot \frac{C_J}{k^2} \left\{ 1 - \frac{1}{2\pi} \cdot \frac{C_J^{\frac{1}{2}}}{k} - \frac{\pi}{120} \cdot \frac{C_J}{k^2} \right\} \quad \ldots \quad \ldots \quad (7)$$

d_o is measured aft the mid-chord point.

APPENDIX II (cont'd)

Lift at incidence (Section 7.0)

$$C_L = C_{L_0} + \alpha \left[\frac{\partial C_L}{\partial \alpha} \right]_{\alpha=0}$$

$$\left[\frac{\partial C_L}{\partial \alpha} \right]_{\alpha=0} = 2\pi \left\{ 1 + \frac{k}{\sqrt{2\pi}} \cdot C_J^{\frac{1}{2}} + \frac{\pi}{24} \cdot \frac{C_J}{k^2} + \frac{1}{24\pi k} \cdot \left(\frac{\pi C_J}{2} \right)^{3/2} \right\} \quad (8)$$

Longitudinal stability (Section 8.0)

$$\frac{d}{c} = \frac{d_0}{c} + \alpha \left[\frac{\partial \left(\frac{d}{c} \right)}{\partial \alpha} \right]_{\alpha=0}$$

where d is measured aft of the mid-chord point.

$$\left[\frac{\partial \left(\frac{d}{c} \right)}{\partial \alpha} \right]_{\alpha=0} = - \frac{\sqrt{\pi/2}}{4k \sin \theta} \cdot \frac{1}{C_J^{\frac{1}{2}}} \left\{ 1 + 0.6\, C_J - 0.4\, C_J^{3/2} \right\} \quad \ldots \quad (9)$$

$(\alpha/6)^2$ Applicable only when α is small as various terms of the order were omitted in the simplification of the expression.

$$\frac{a}{c} = \frac{k}{4} \cdot \frac{C_J^{\frac{1}{2}}}{\sqrt{2\pi}}$$

where a is measured aft of the quarter-chord point.

FIG. 1

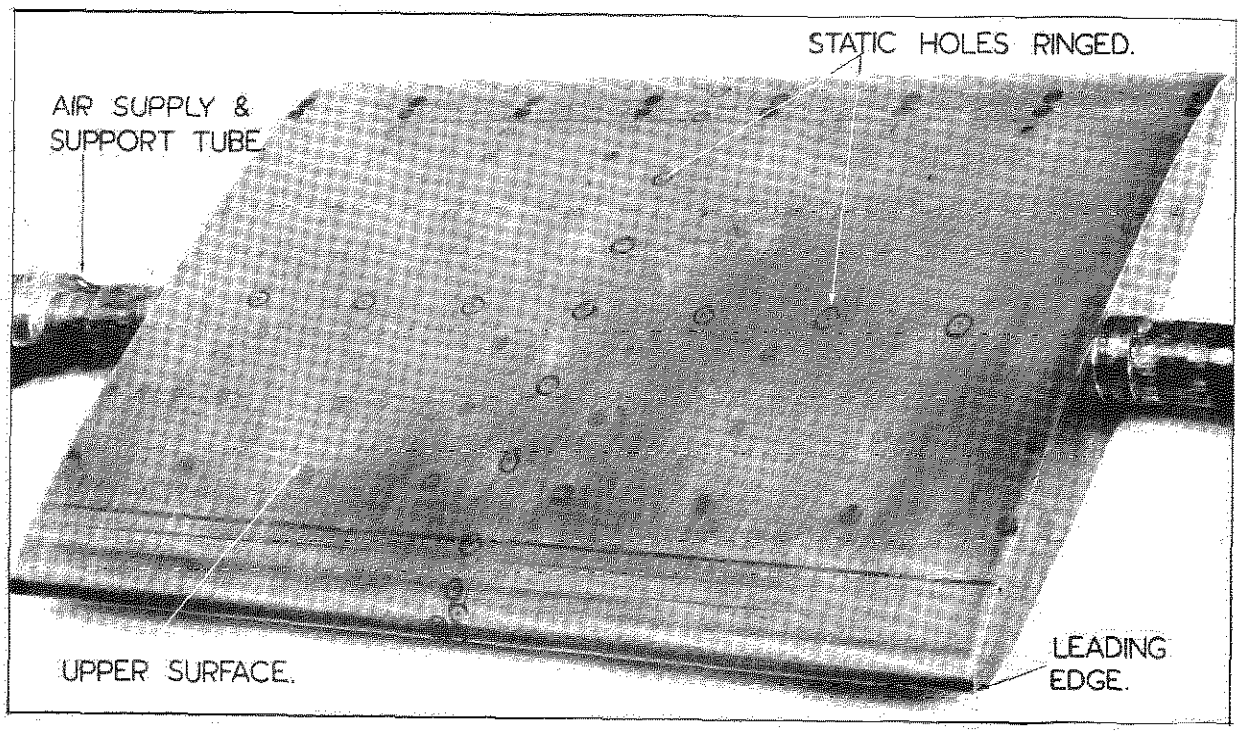

(a) THE MODEL - EXTERNAL.

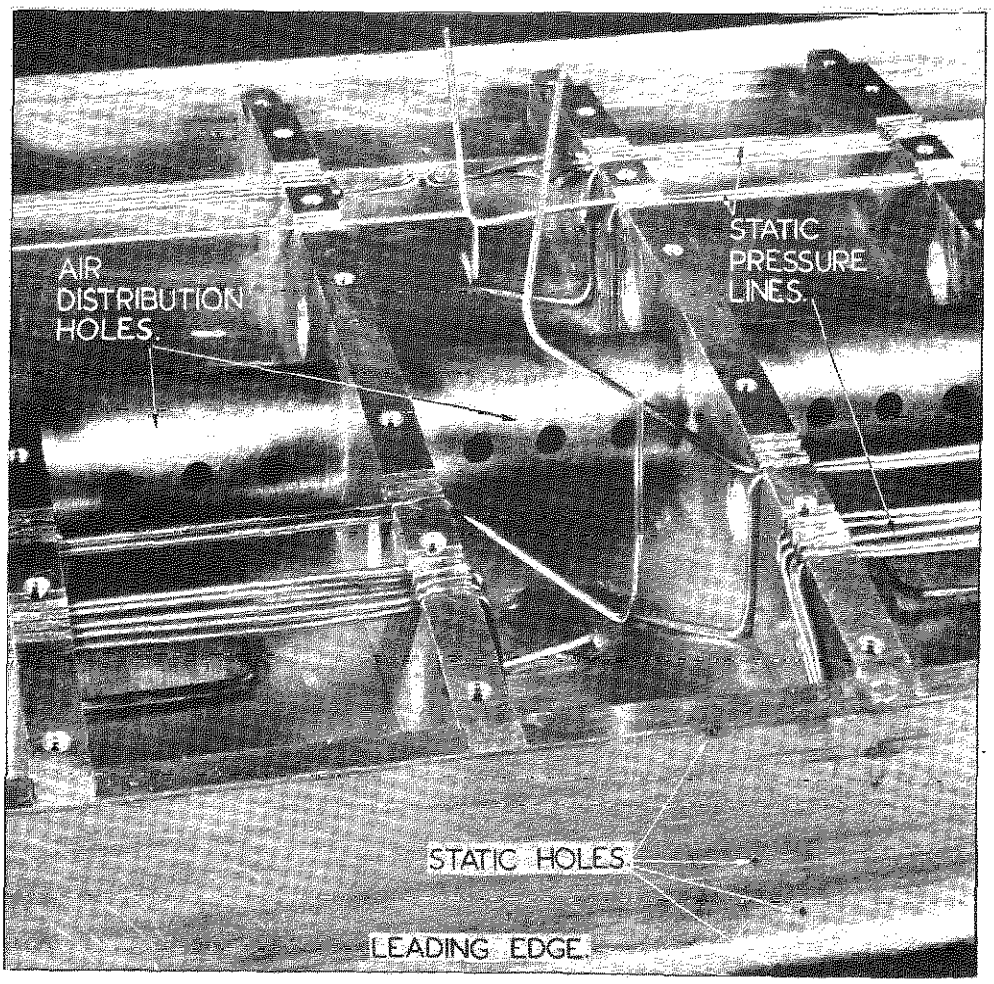

(b) VIEW SHOWING THE CONSTRUCTION OF THE MODEL.

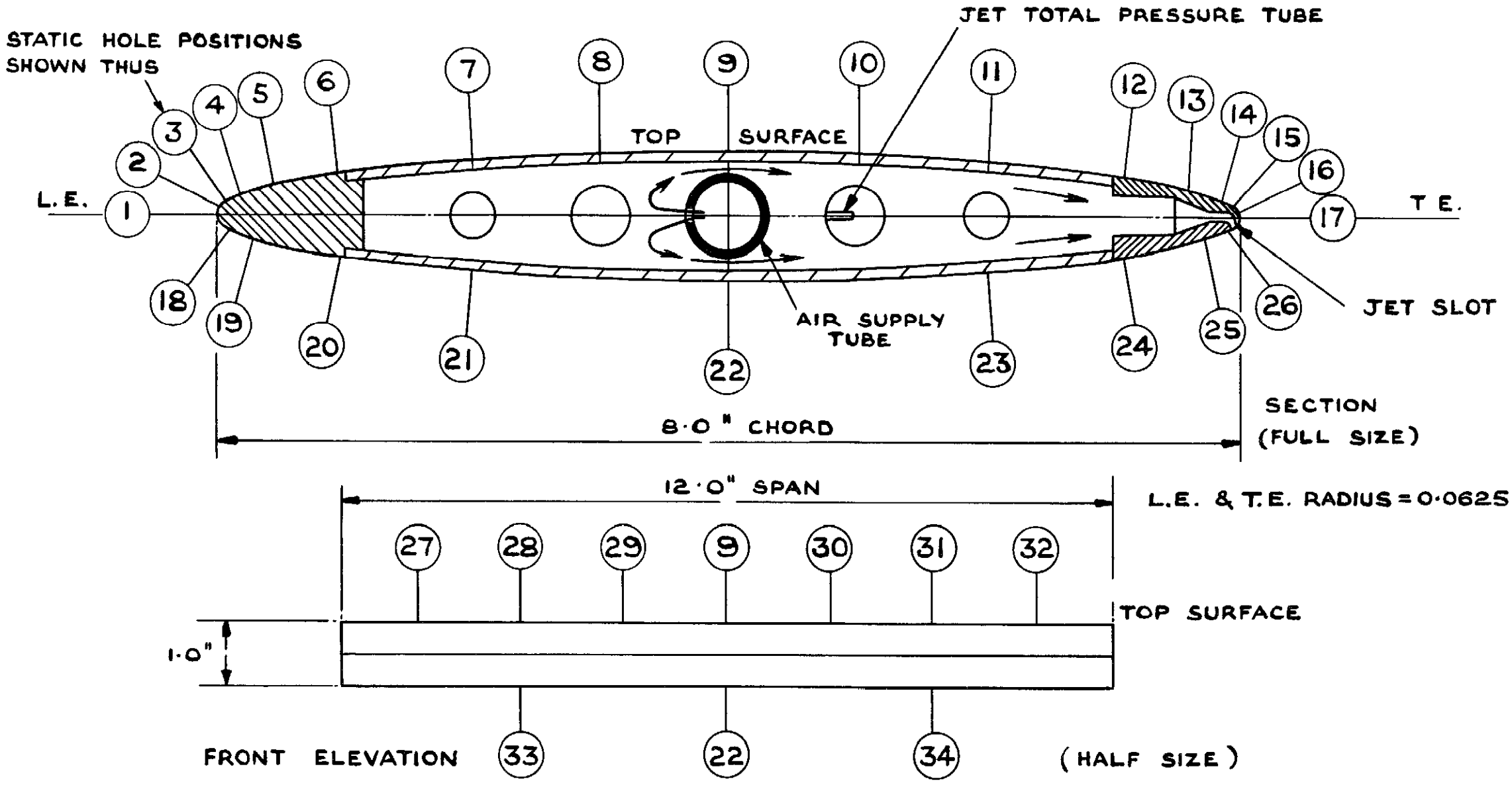

SECTION OF MODEL—12·5% THICK ELLIPSE.

FIG. 2

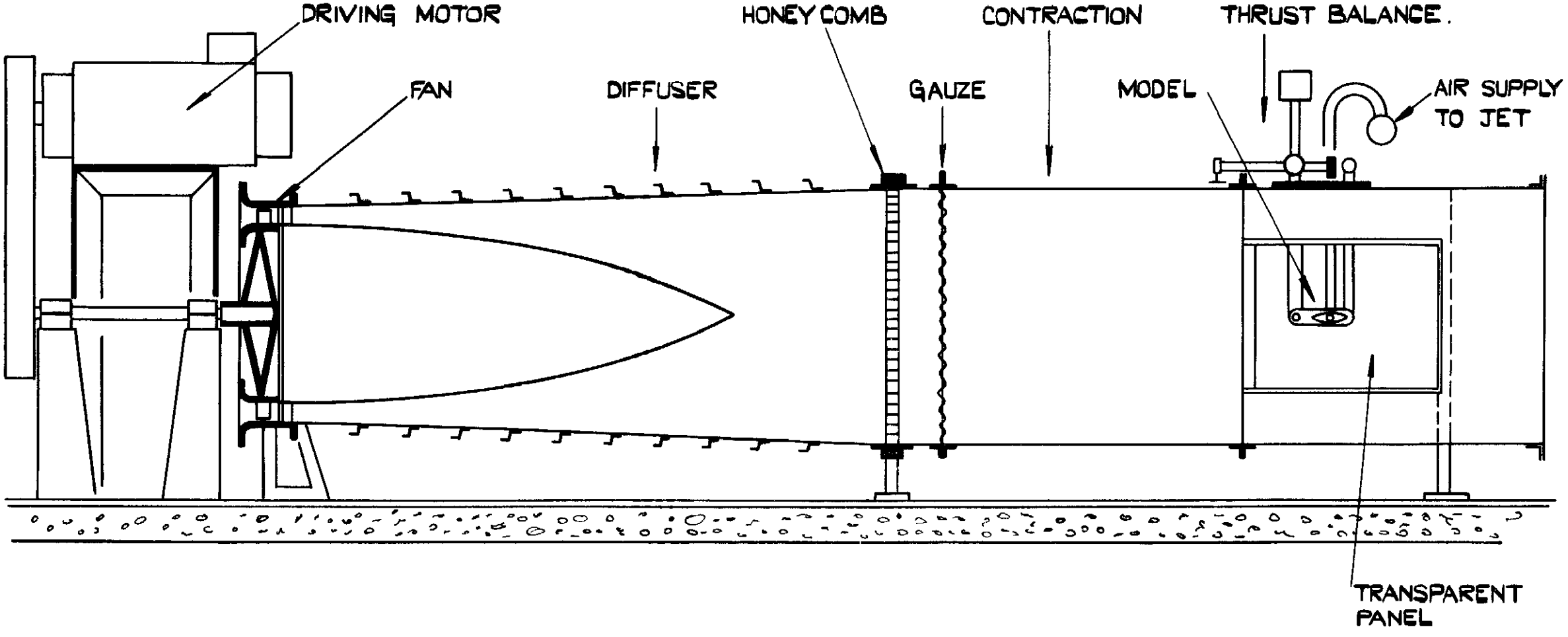

ARRANGEMENT OF WIND-TUNNEL.

FIG.3

FIG. 4

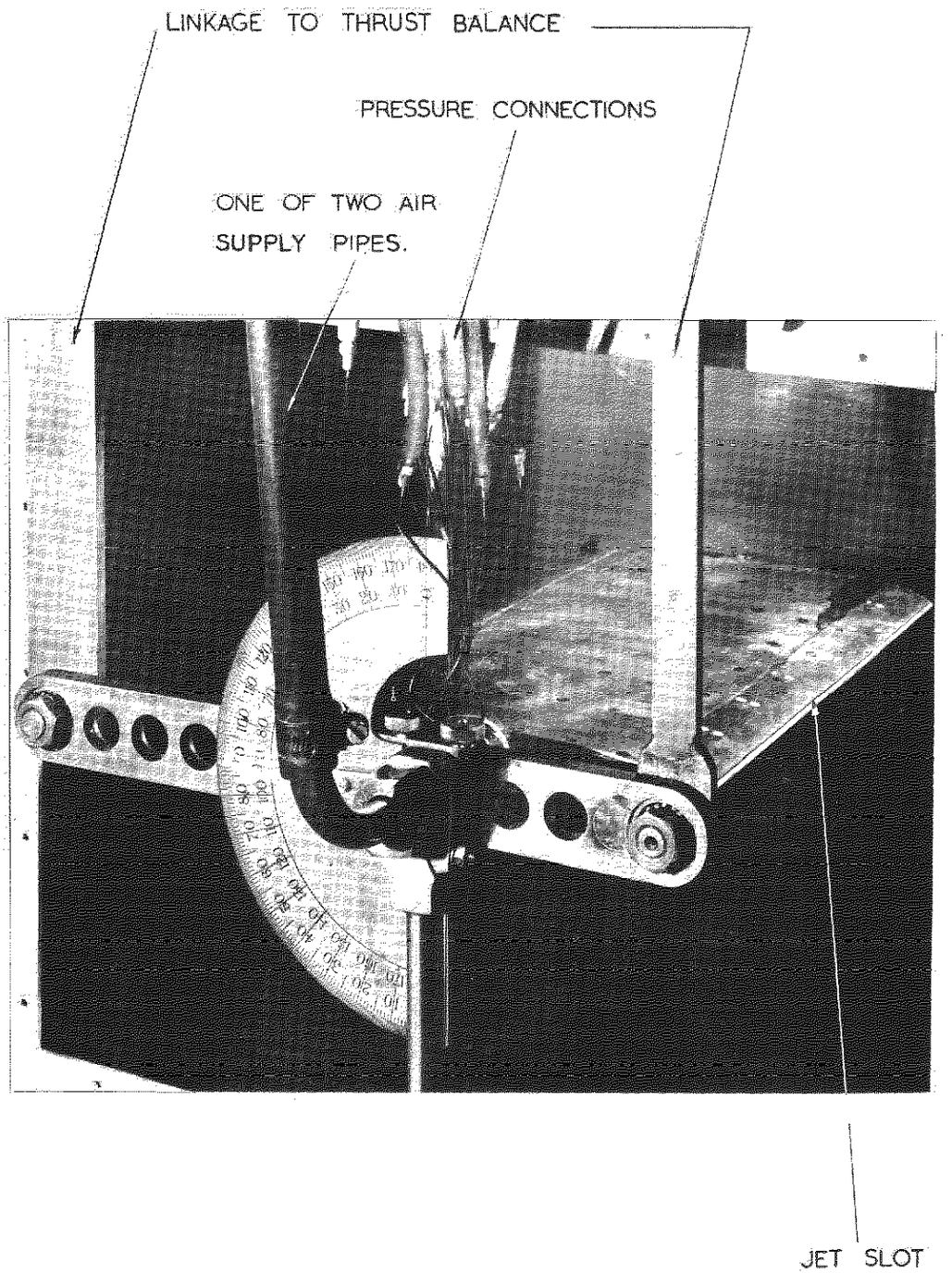

WORKING SECTION WITH MODEL.

FIG.5

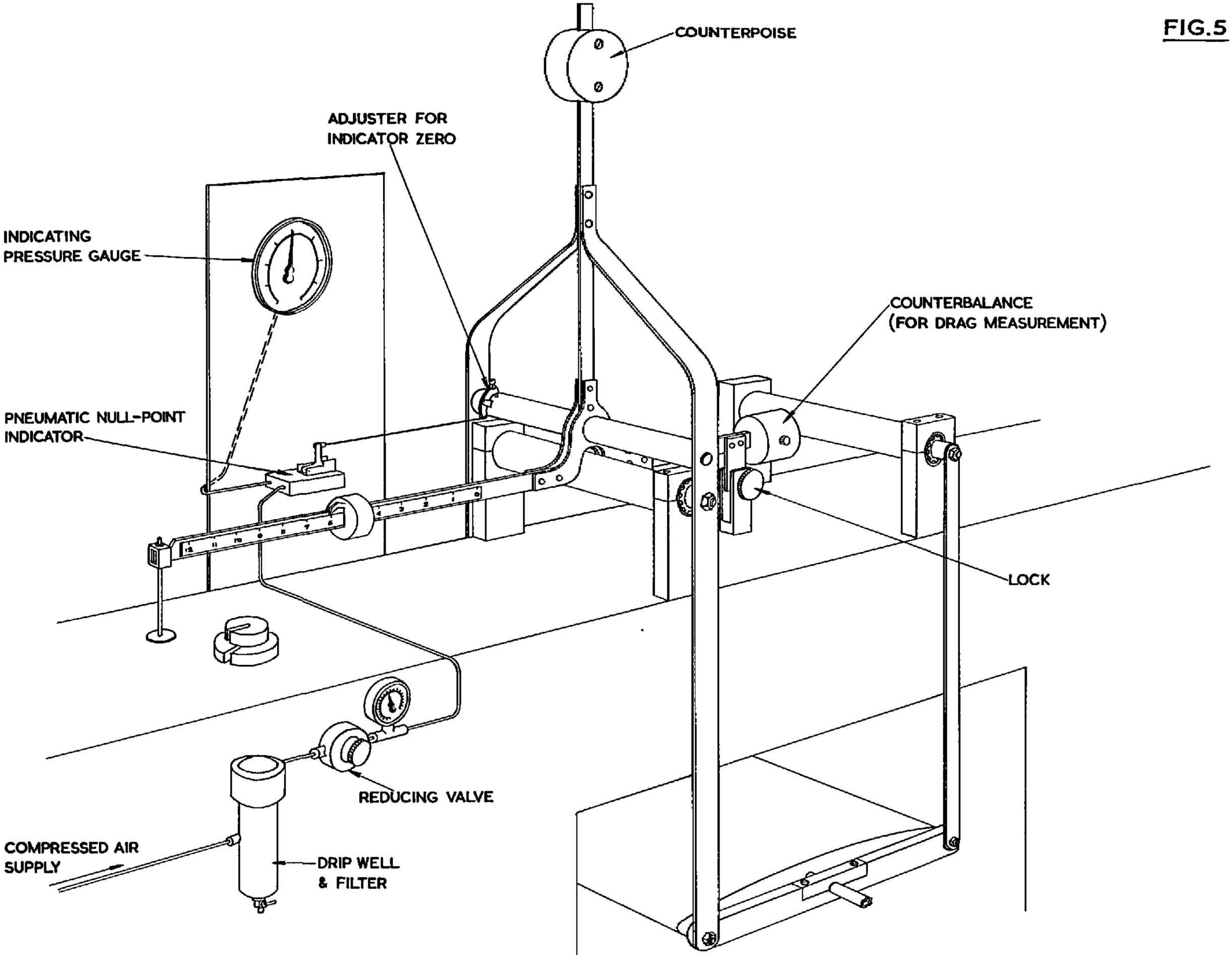

THE THRUST BALANCE

FIG. 6

AVERAGE WIDTH OF SLOT = 0·0231 INS.

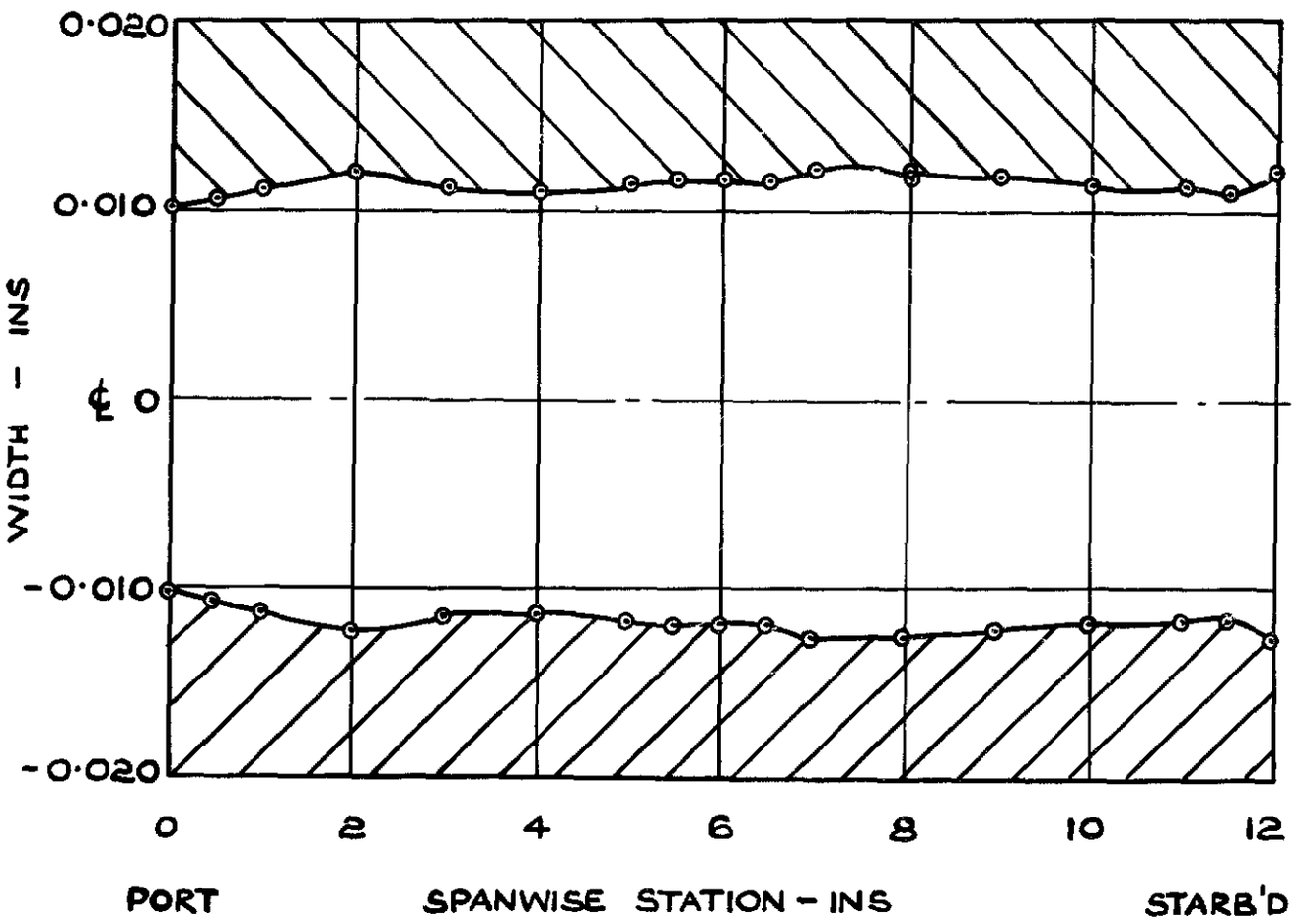

VARIATION OF JET SLOT.

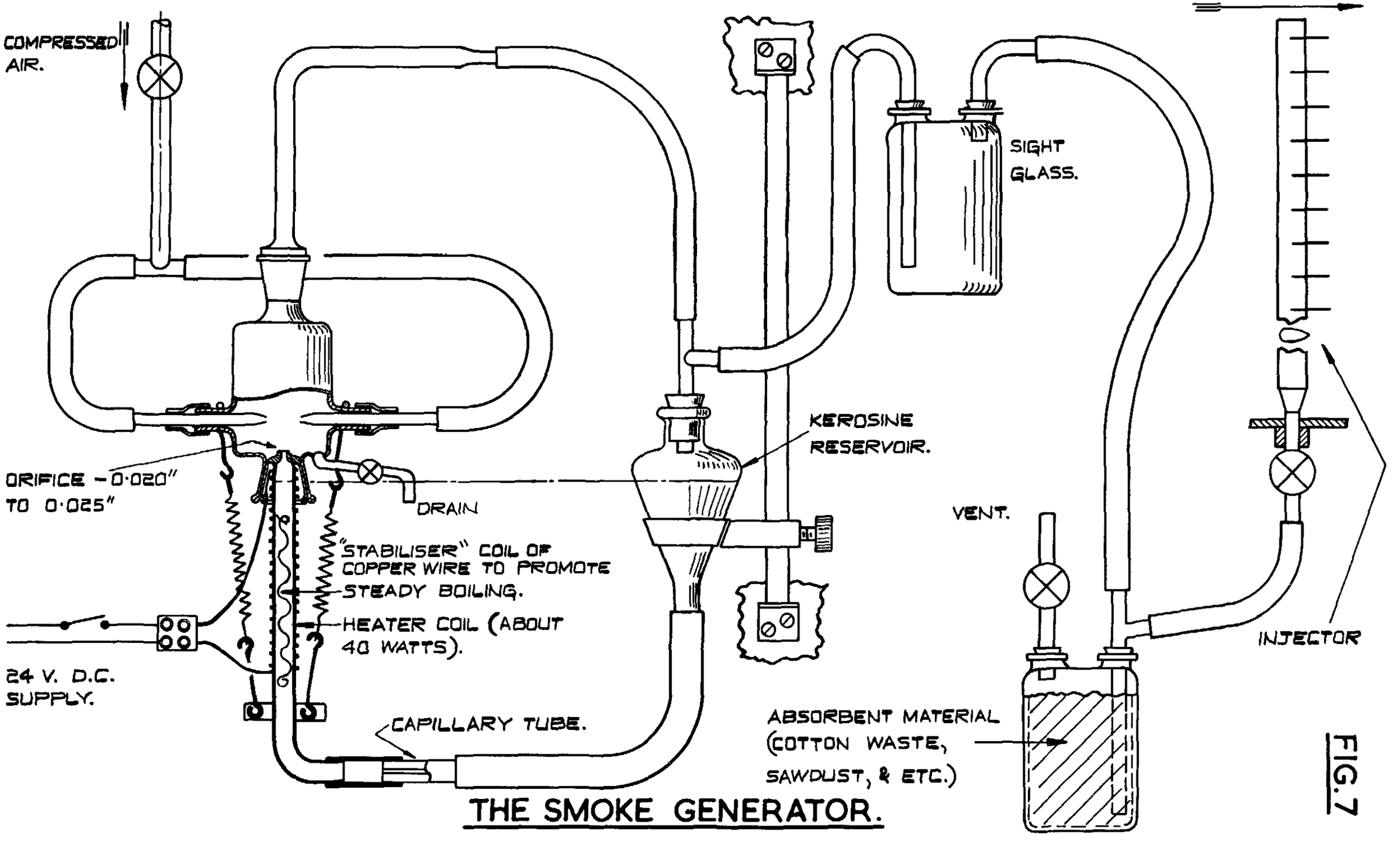

THE SMOKE GENERATOR.

FIG.7

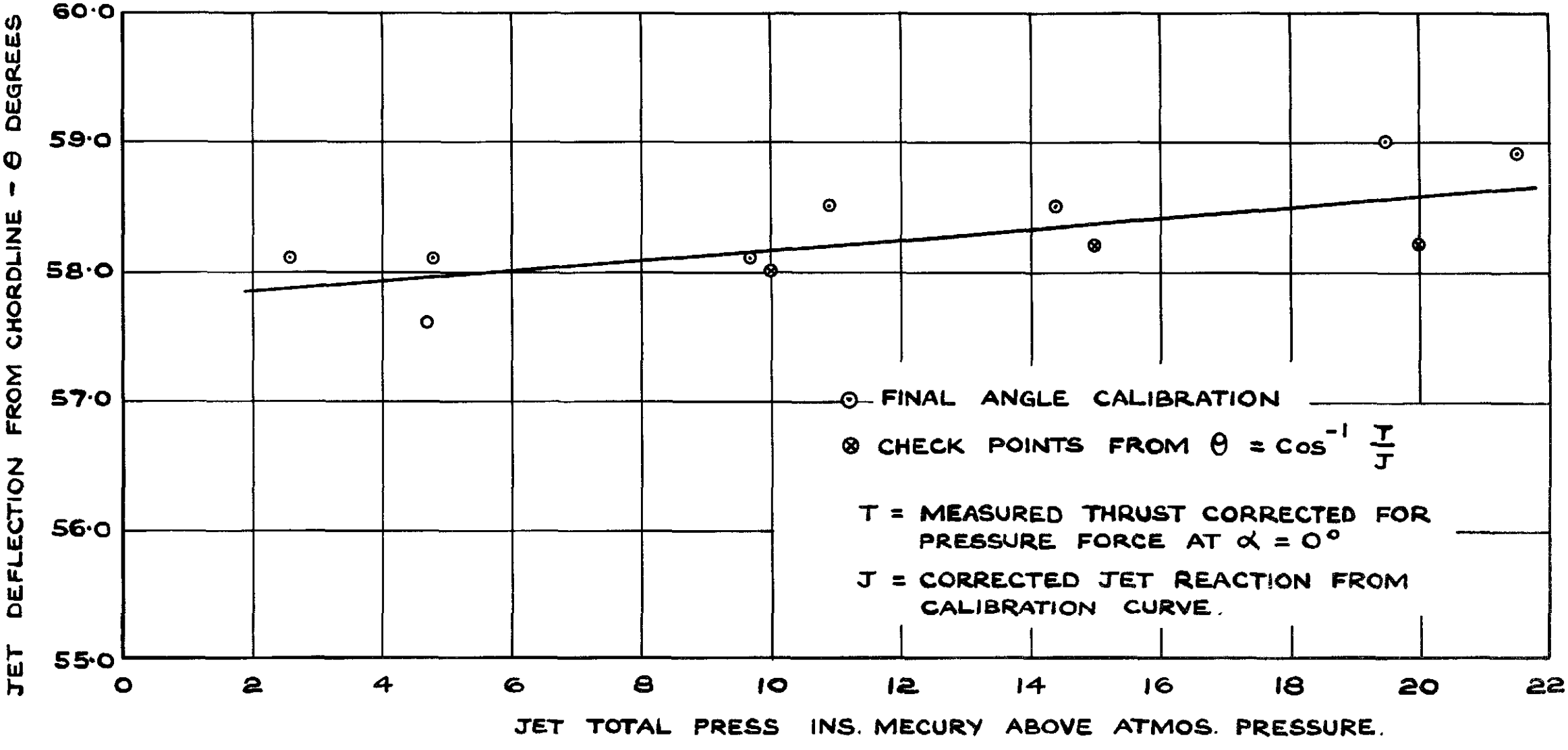

VARIATION OF JET DEFLECTION ANGLE WITH JET TOTAL PRESSURE.

FIG. 8

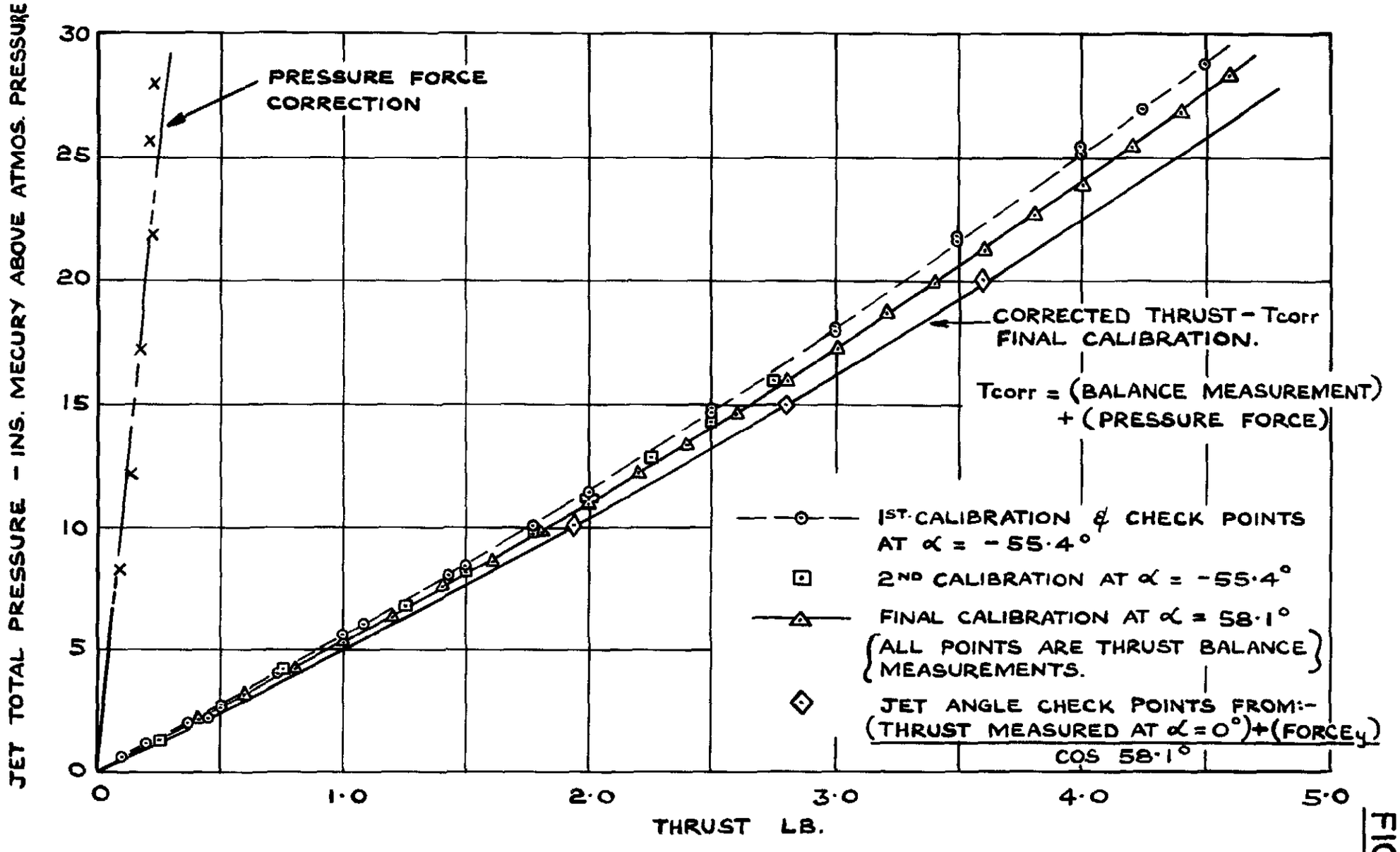

THRUST CALIBRATION CURVES FOR MODEL WITH JET DEFLECTED 58·1°

FIG. 9

FIG. 10

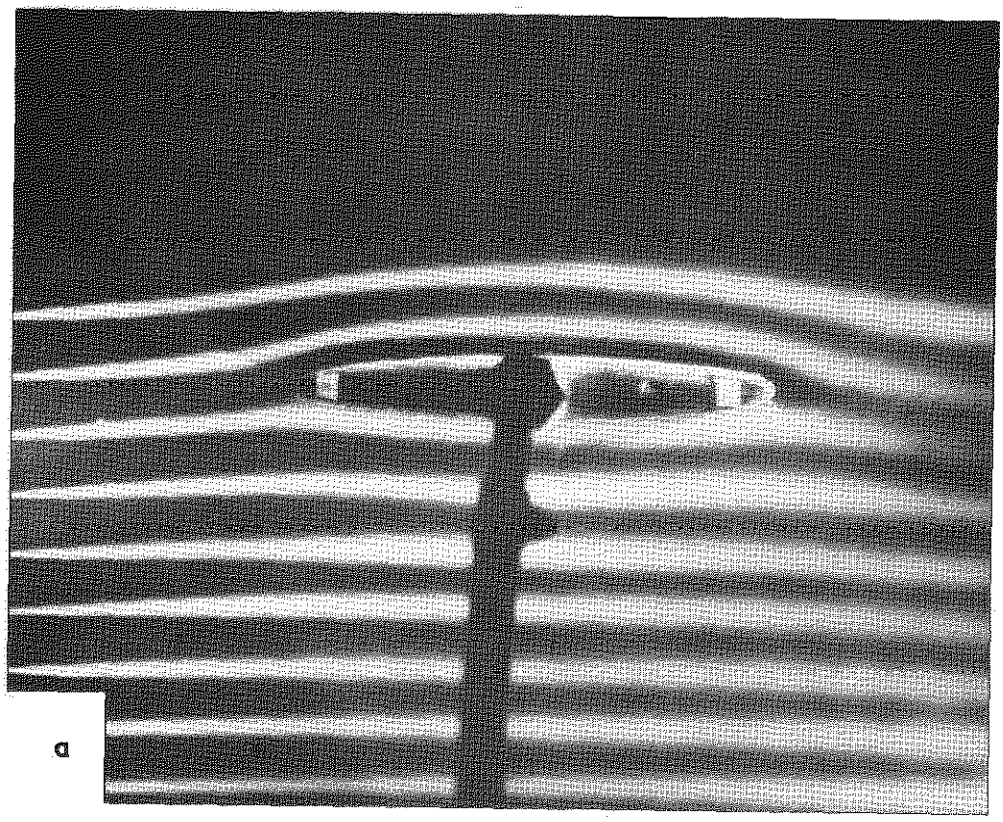

a

$C_J = 0{\cdot}10 \qquad C_{L_O} = 0{\cdot}91$

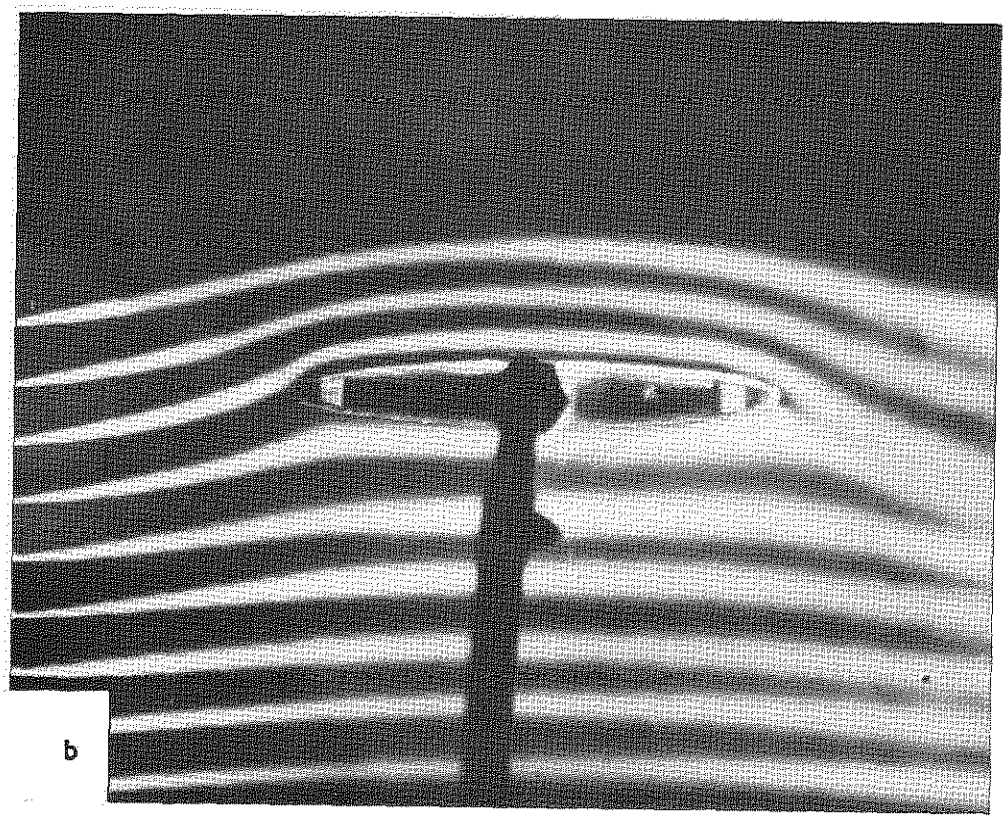

b

$C_J = 0{\cdot}30 \qquad C_{L_O} = 1{\cdot}99$

THE FLOW PATTERN

FIG. 11

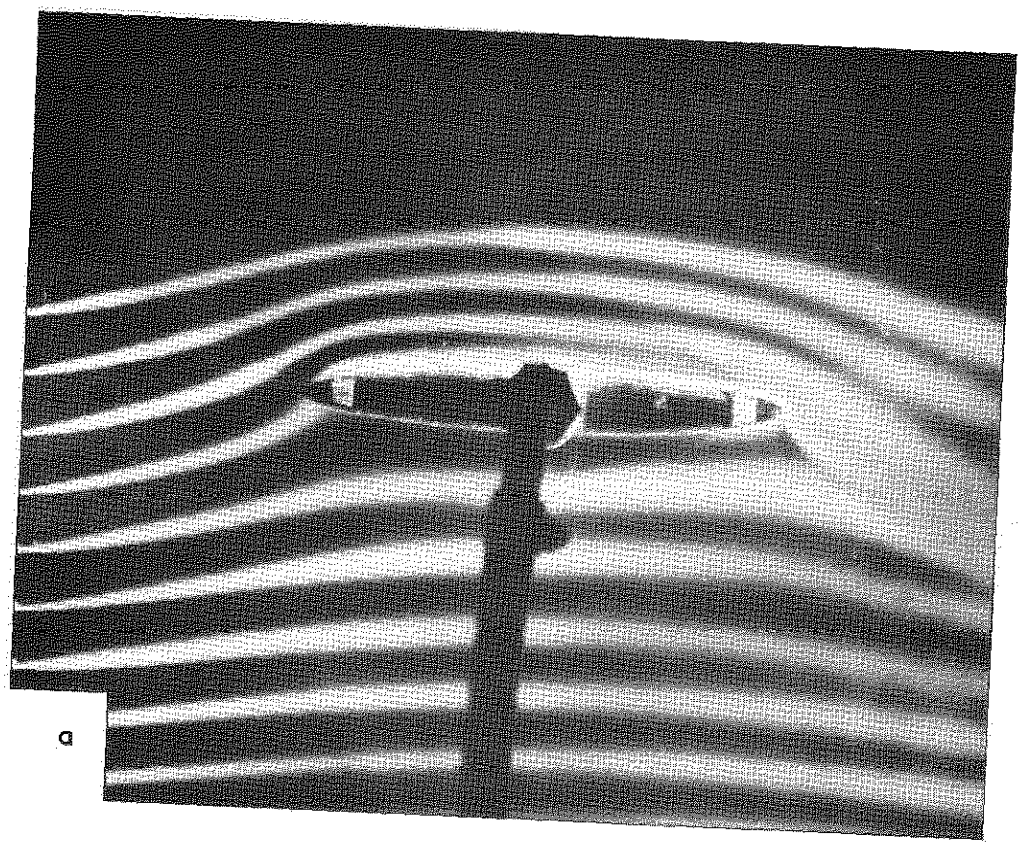

a

$C_J = 0.50 \quad C_{L_0} = 2.79$

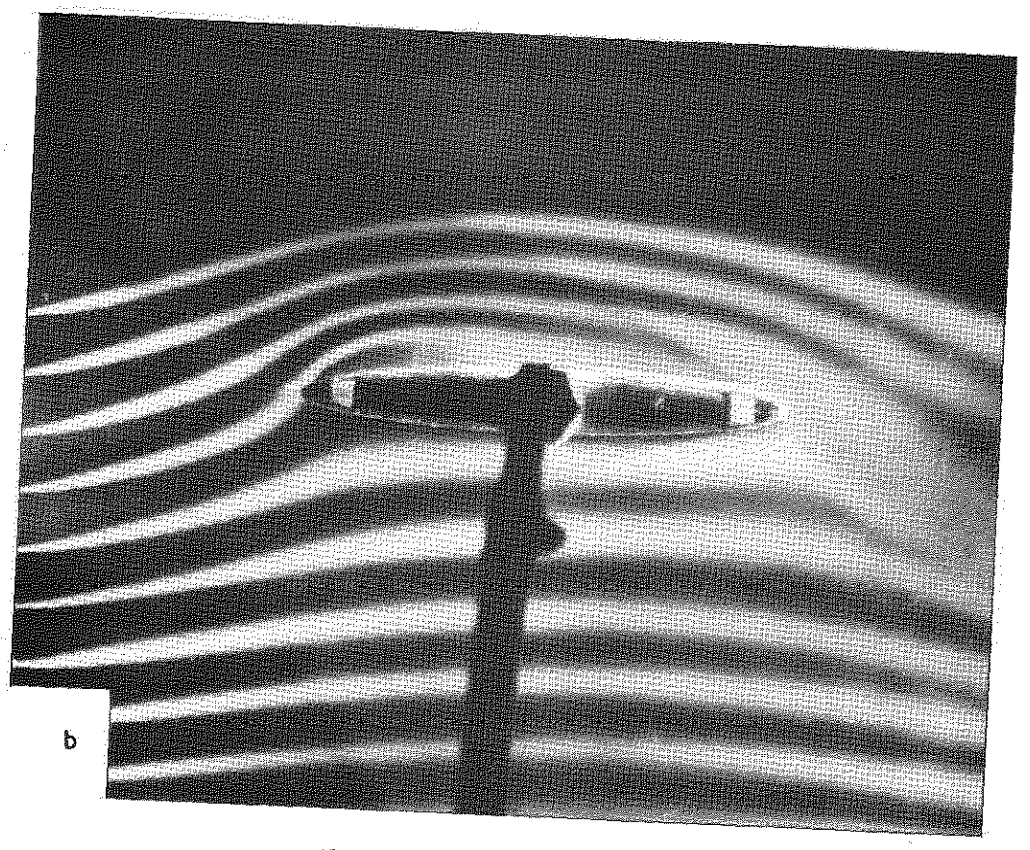

b

$C_J = 0.75 \quad C_{L_0} = 3.50$

THE FLOW PATTERN

FIG. 12

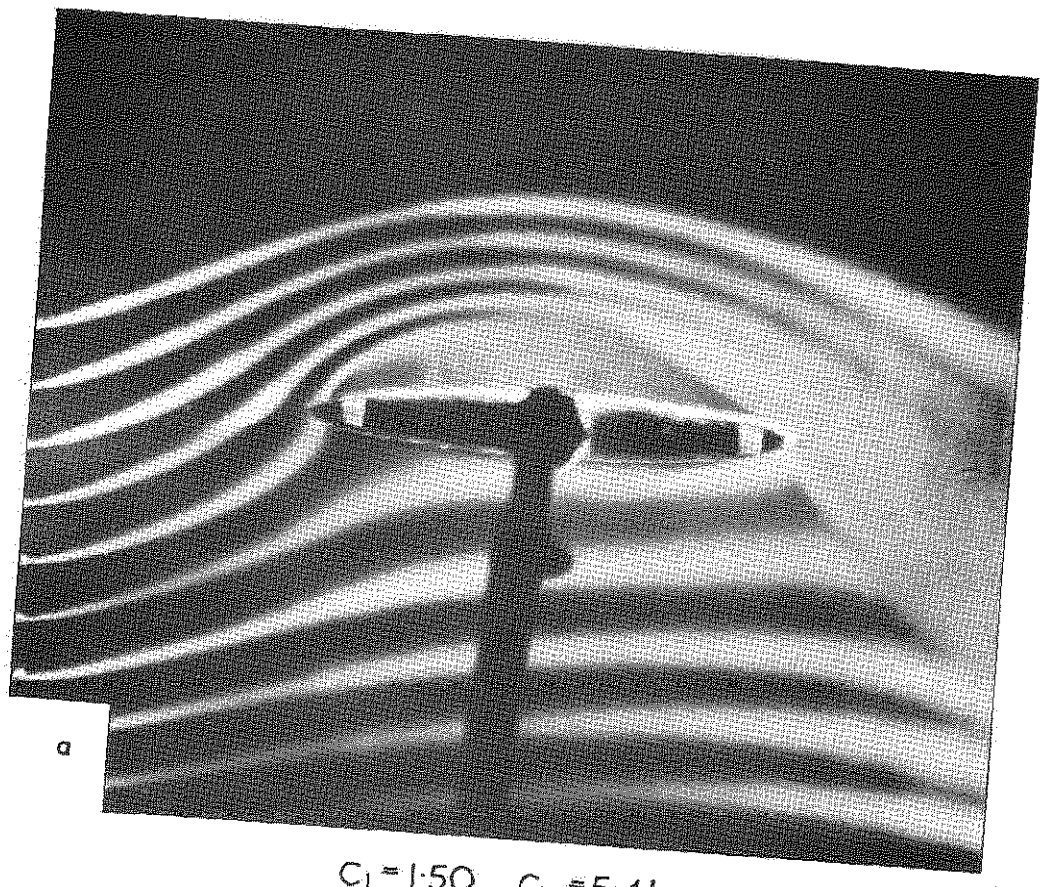

a

$C_J = 1.50 \quad C_{L_0} = 5.41$

b

$C_J = 5.00 \quad C_{L_0} = 12.35$

THE FLOW PATTERN

FIG. 13

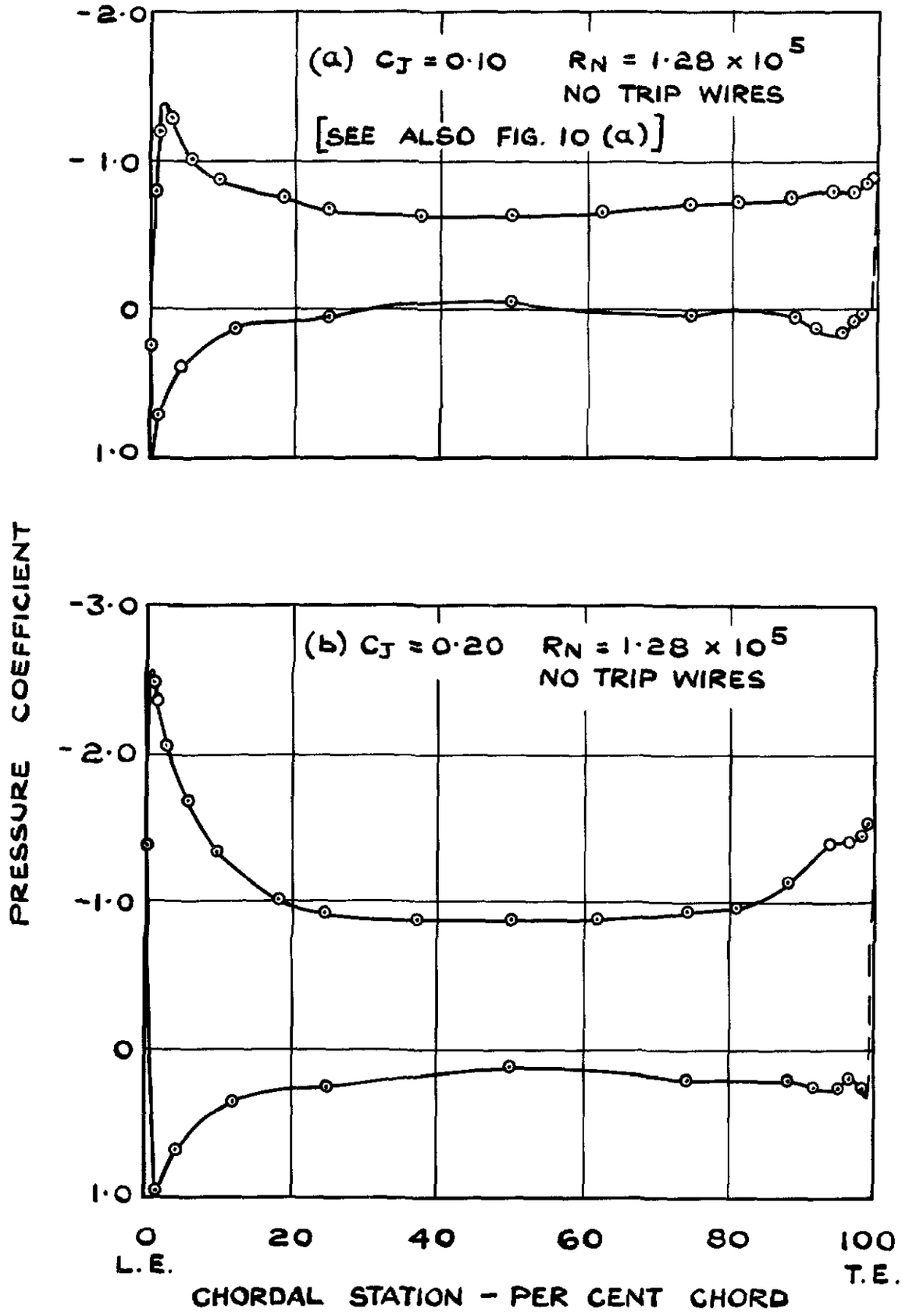

PRESSURE DISTRIBUTION AT ZERO INCIDENCE.

FIG. 14.

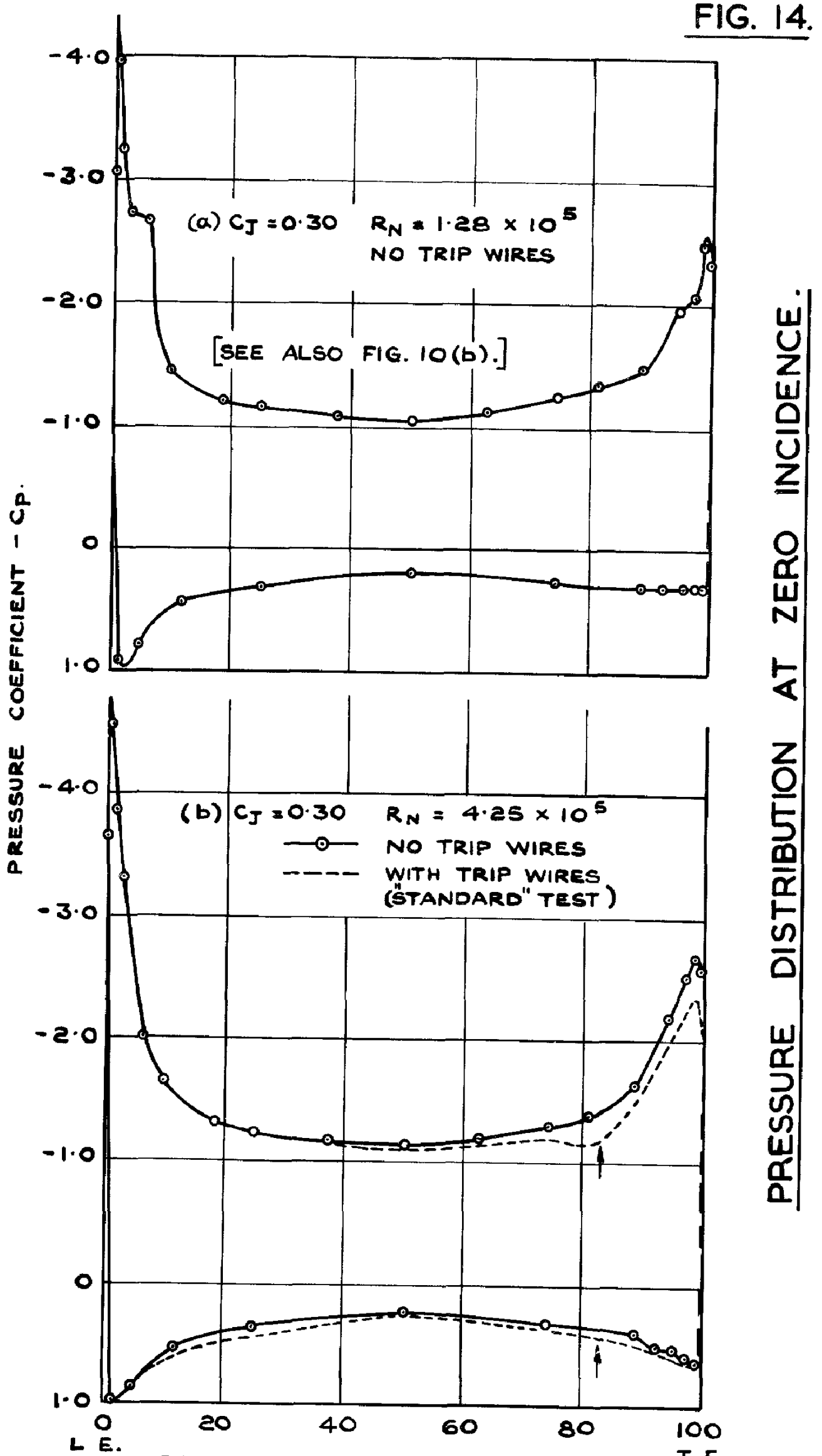

PRESSURE DISTRIBUTION AT ZERO INCIDENCE.

FIG. 15

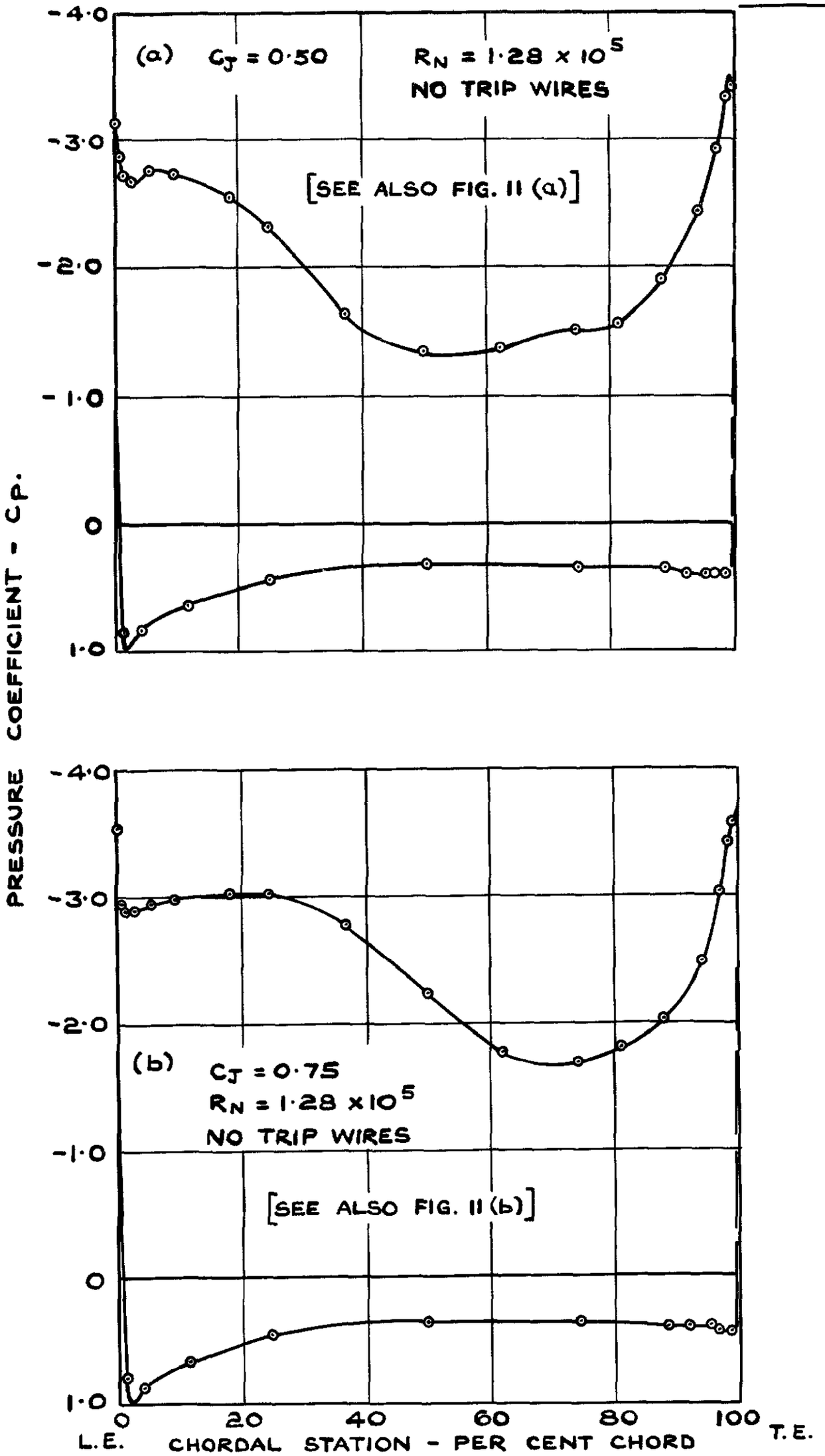

PRESSURE DISTRIBUTION AT ZERO INCIDENCE

FIG. 16

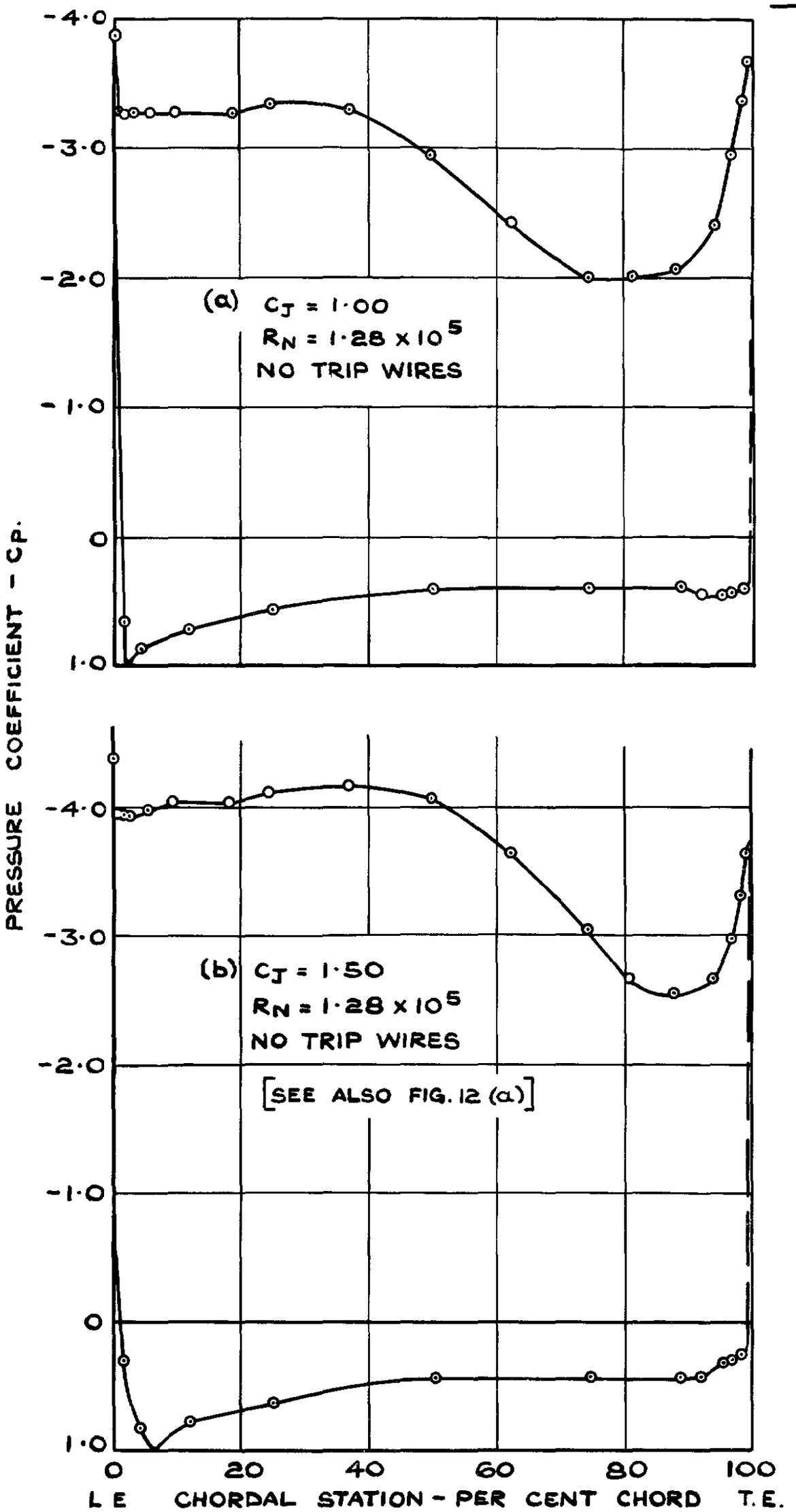

PRESSURE DISTRIBUTIONS AT ZERO INCIDENCE.

FIG. 17

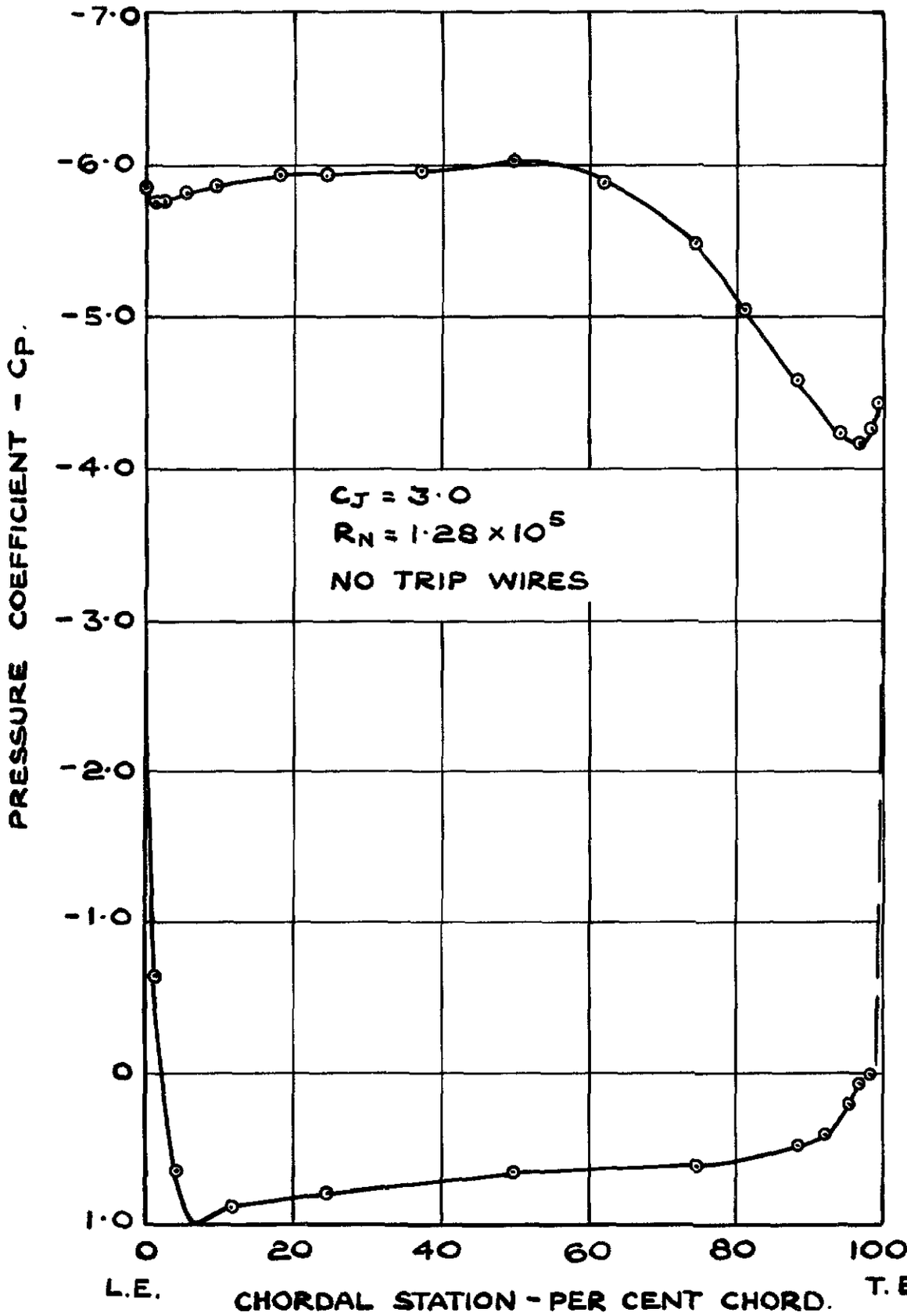

PRESSURE DISTRIBUTION AT ZERO INCIDENCE

FIG. 18

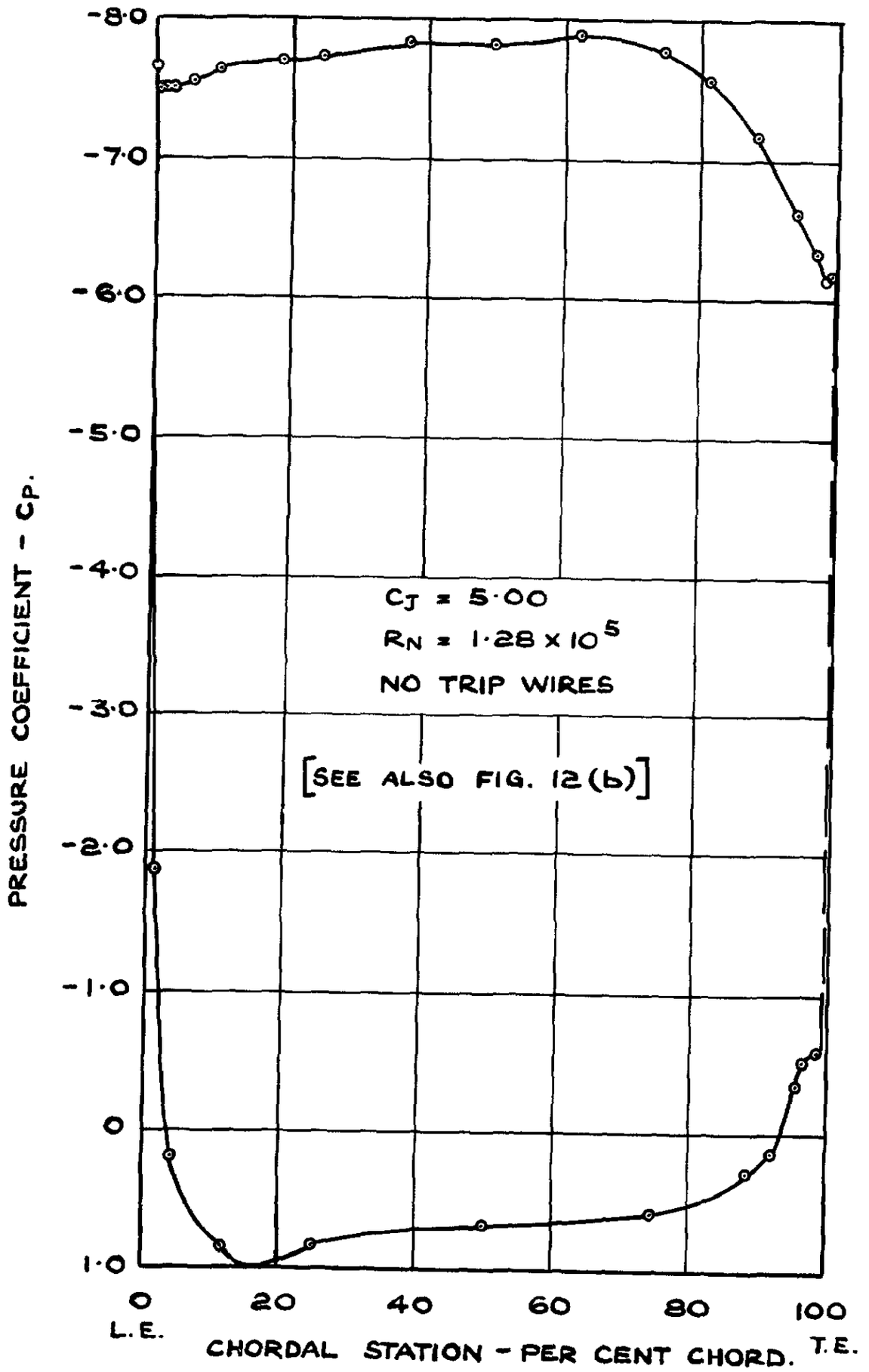

PRESSURE DISTRIBUTION AT ZERO INCIDENCE.

FIG. 19

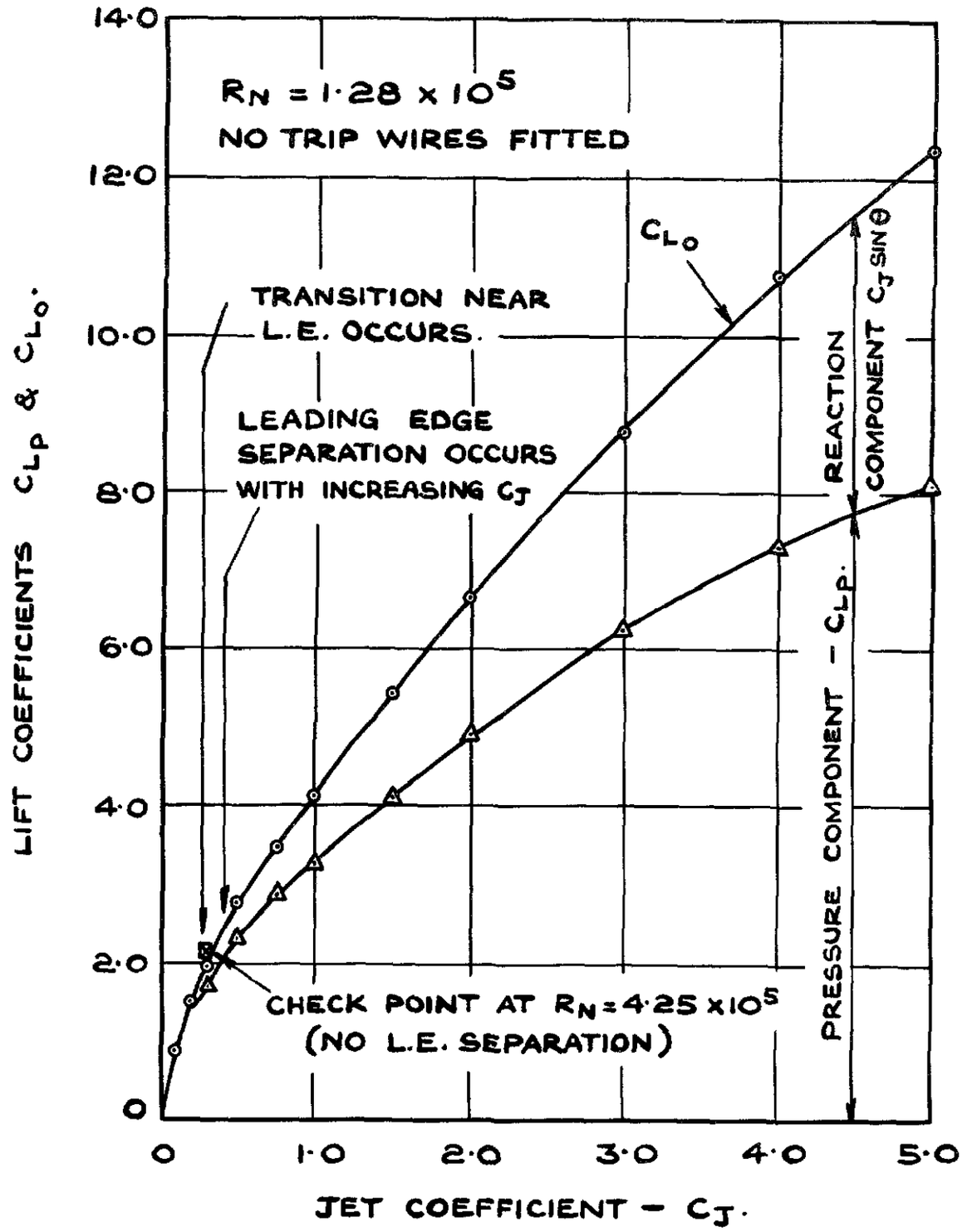

LIFT AT ZERO INCIDENCE.

FIG. 20

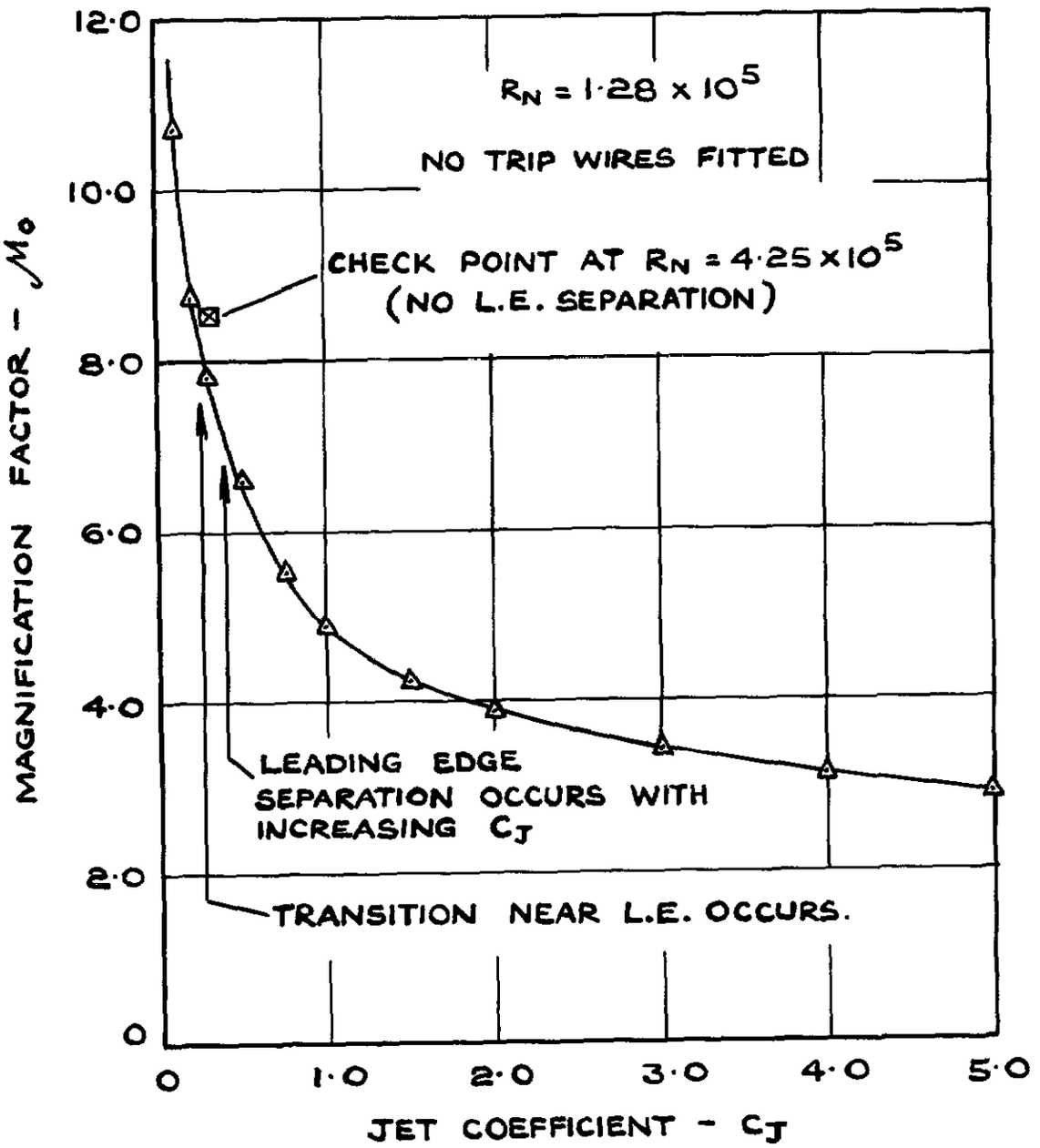

VARIATION OF M_o WITH C_J

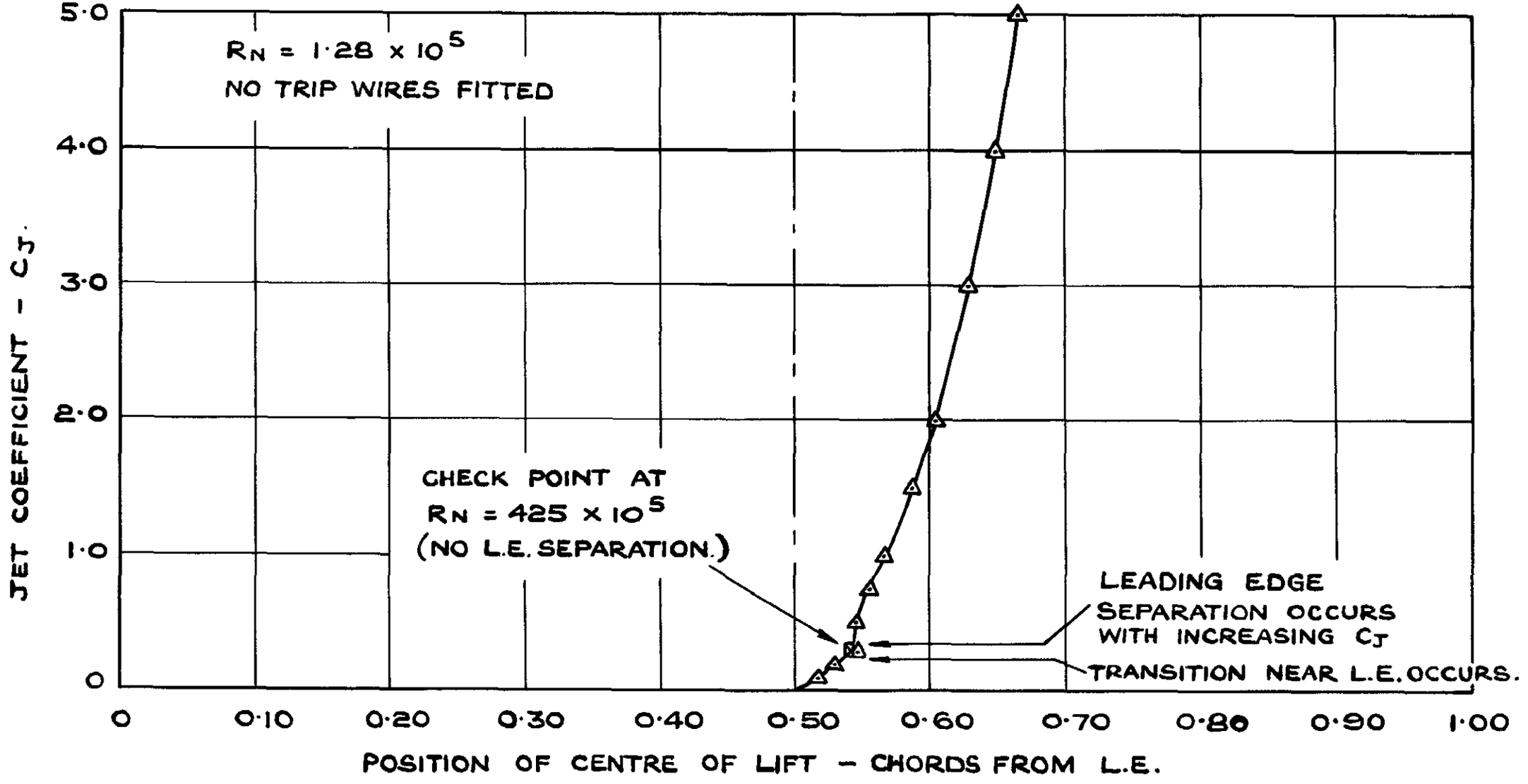

THE CENTRE OF LIFT AT ZERO INCIDENCE.

FIG. 21

FIG. 22

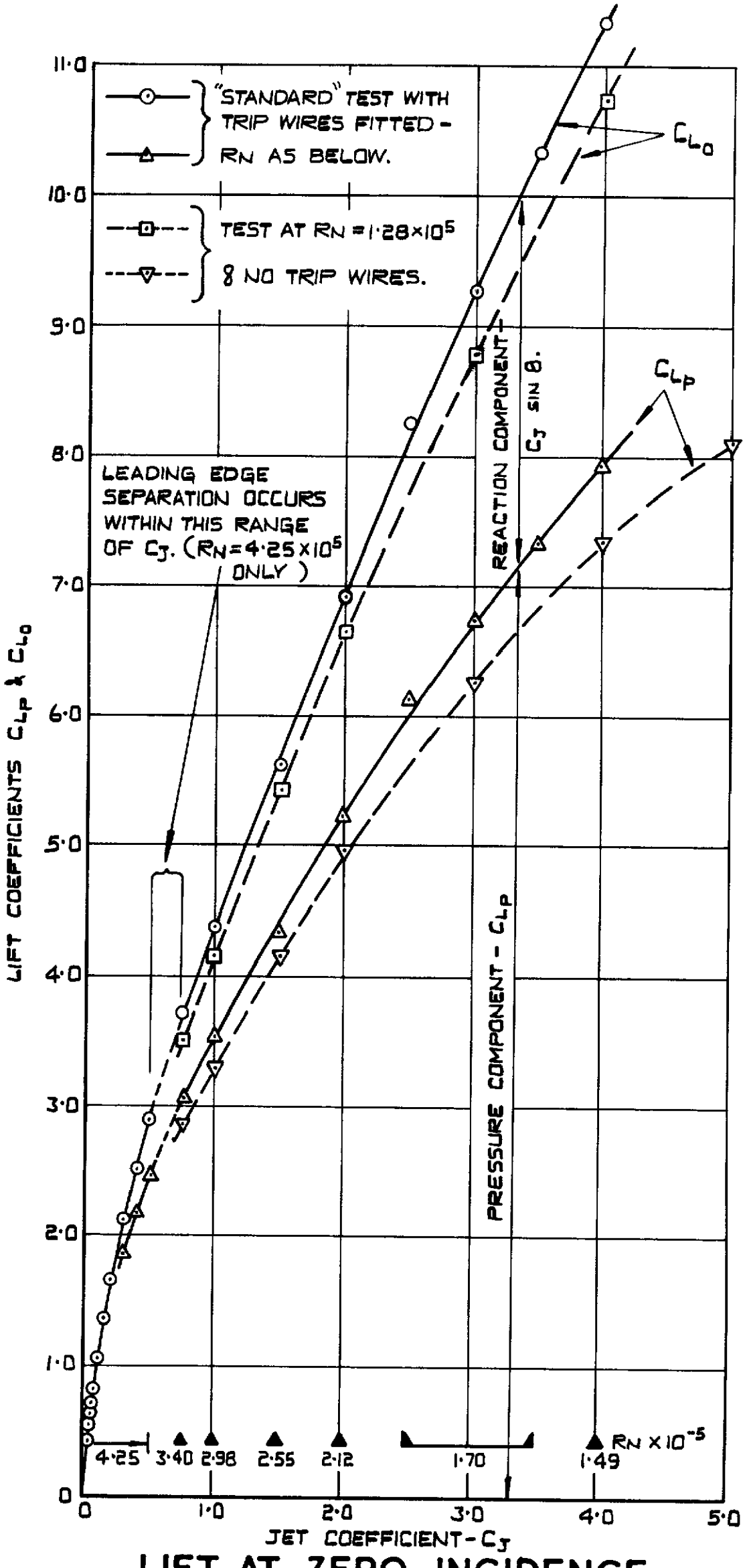

LIFT AT ZERO INCIDENCE.

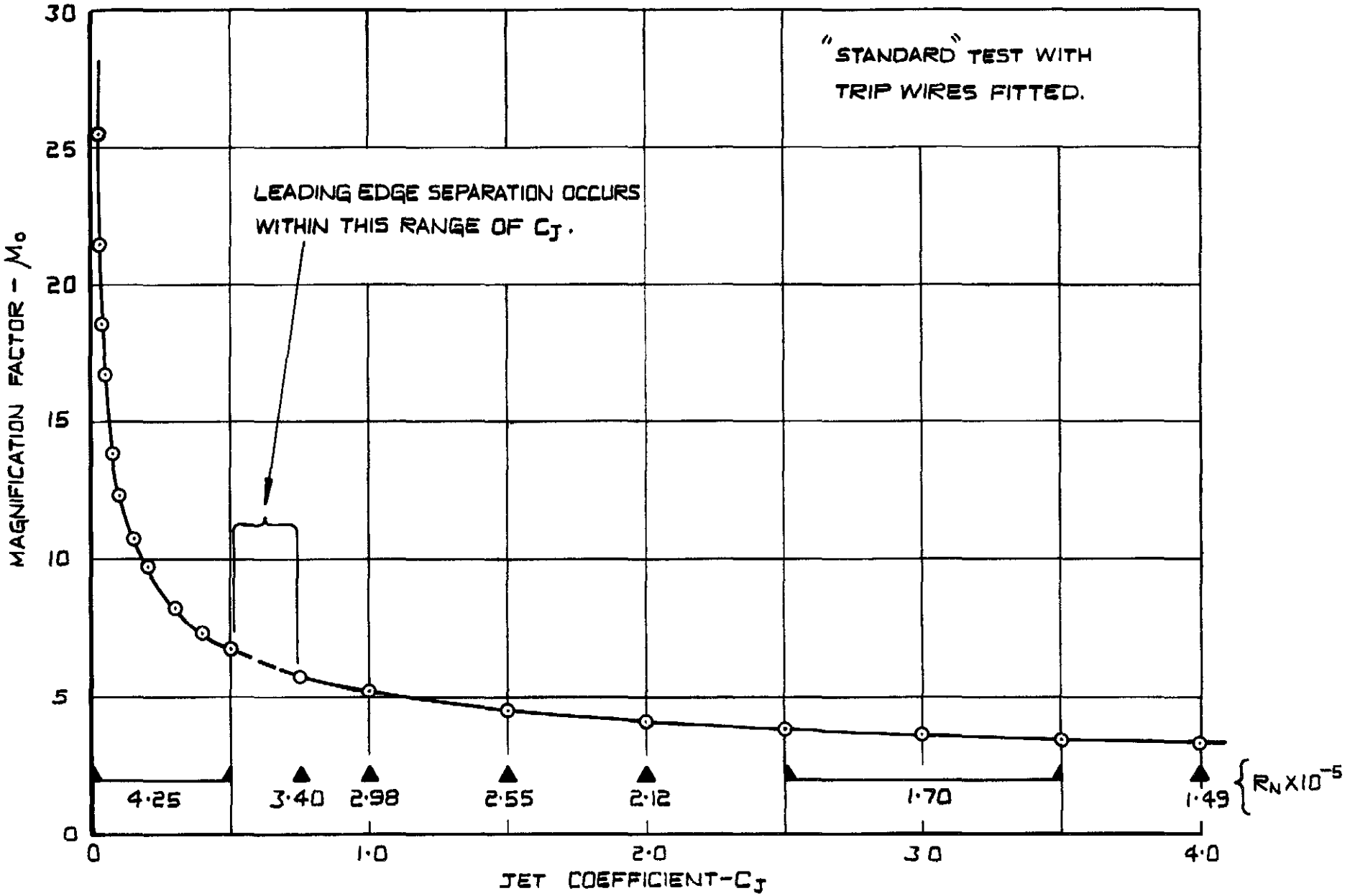

VARIATION OF Mo WITH C_J

FIG.23

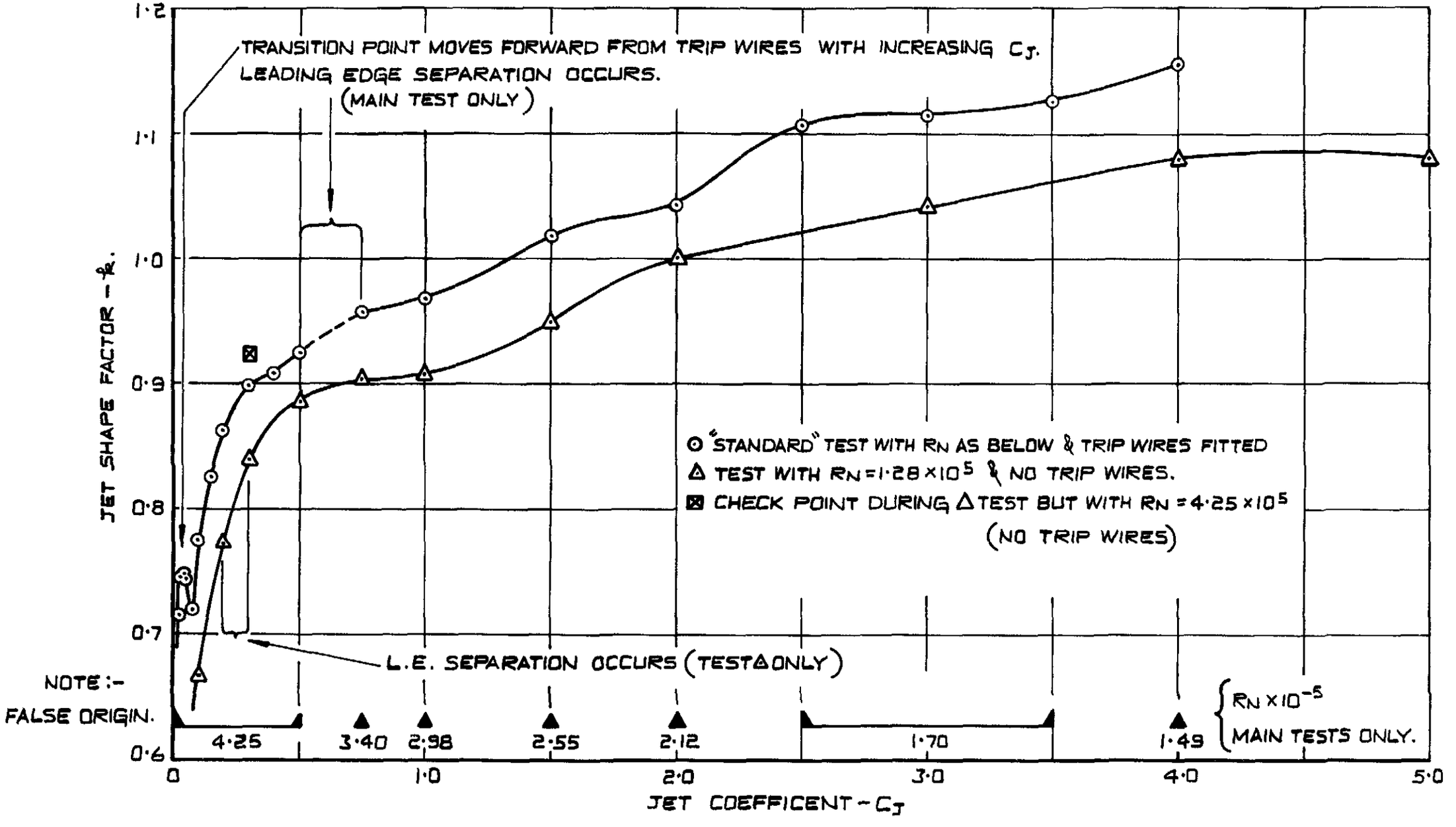

THE EXPERIMENTAL VALUE OF k.

FIG.24

FIG. 25

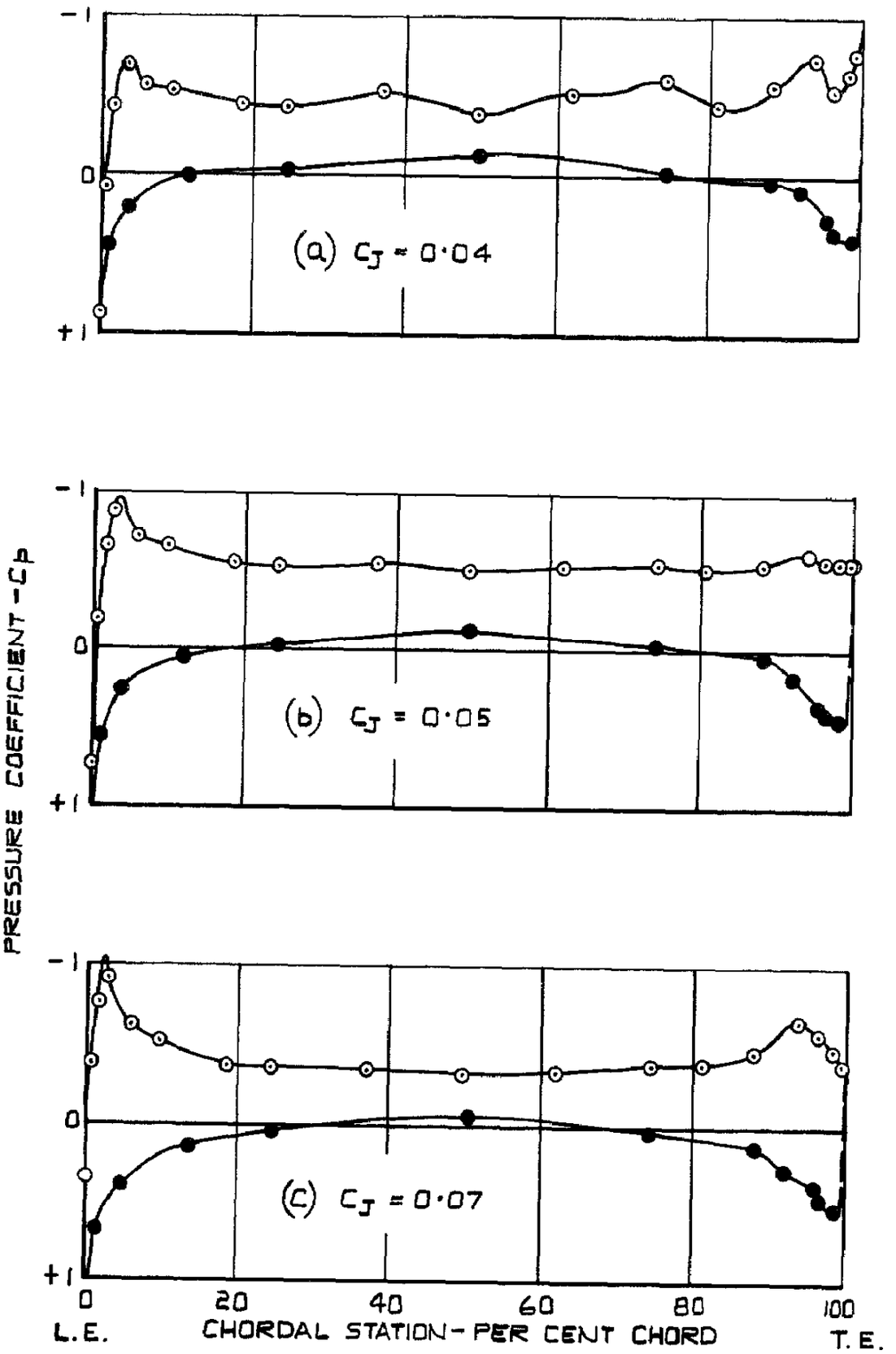

$R_N = 4·25 \times 10^6$;
NO TRIP WIRES FITTED.

PRESSURE DISTRIBUTION AT ZERO INCIDENCE.

FIG. 26

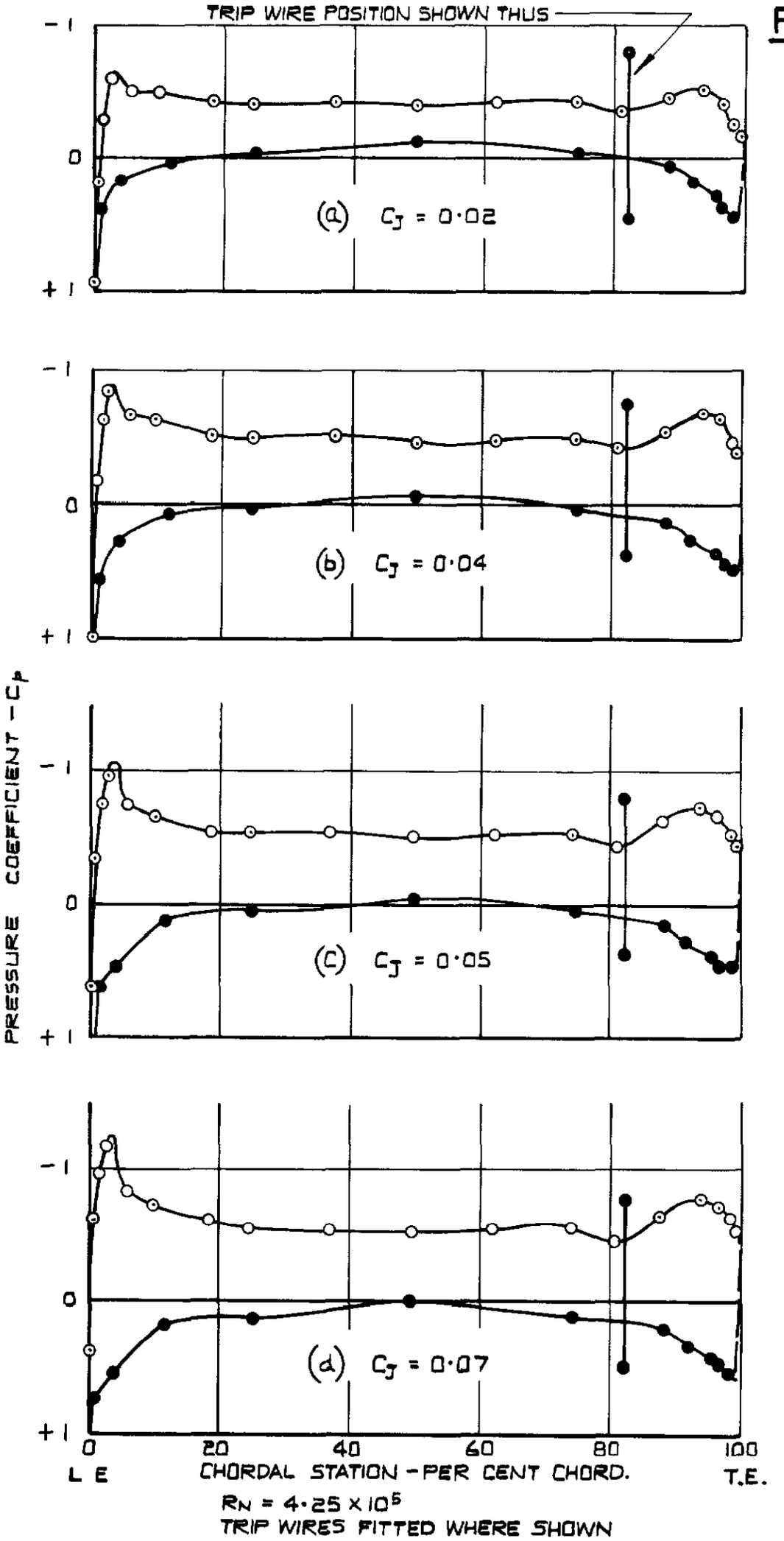

$R_N = 4·25 \times 10^5$

TRIP WIRES FITTED WHERE SHOWN

PRESSURE DISTRIBUTION AT ZERO INCIDENCE.

FIG. 27

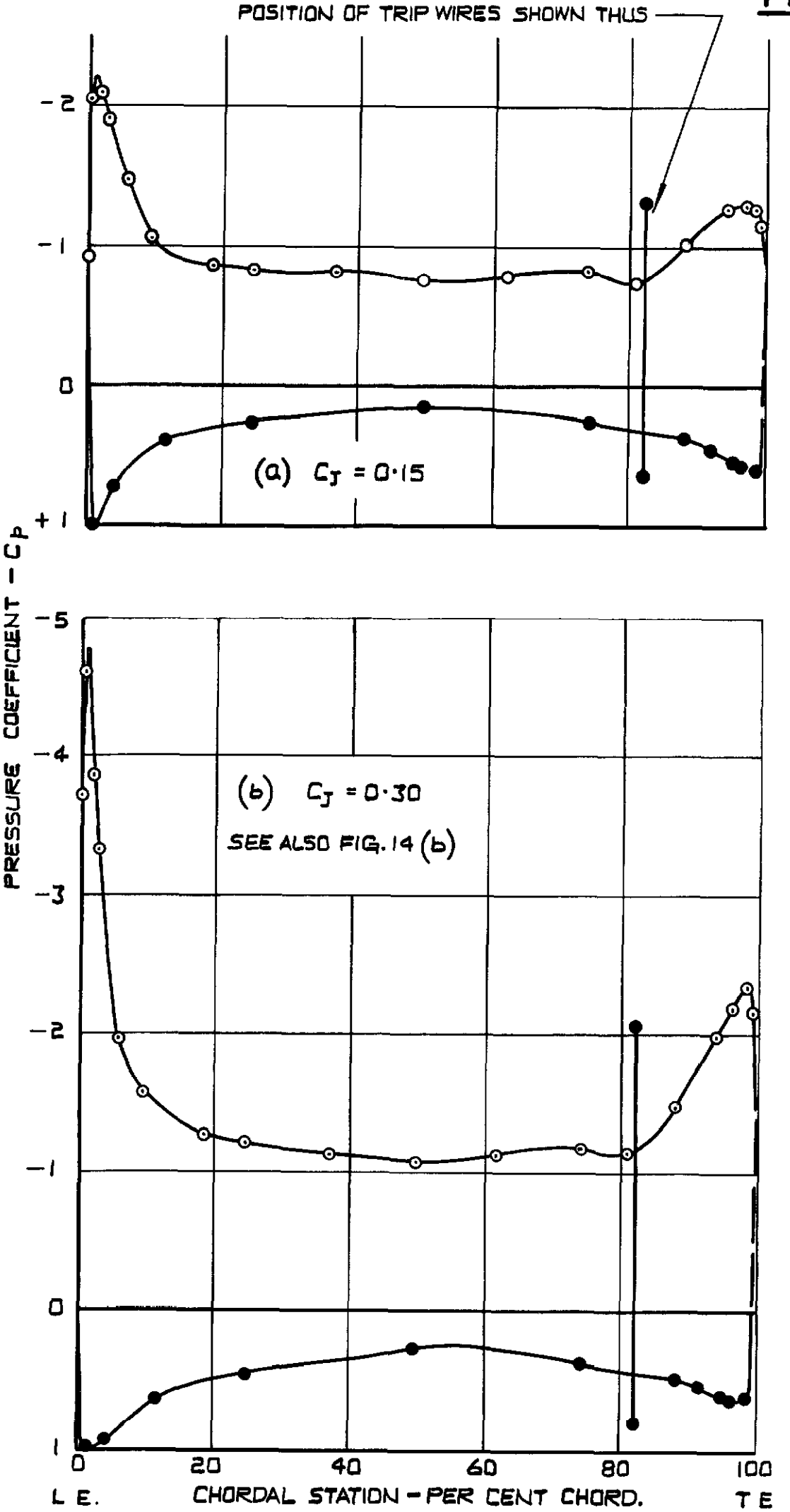

$R_N = 4·25 \times 10^5$
TRIP WIRES FITTED WHERE SHOWN

PRESSURE DISTRIBUTION AT ZERO INCIDENCE.

FIG.28

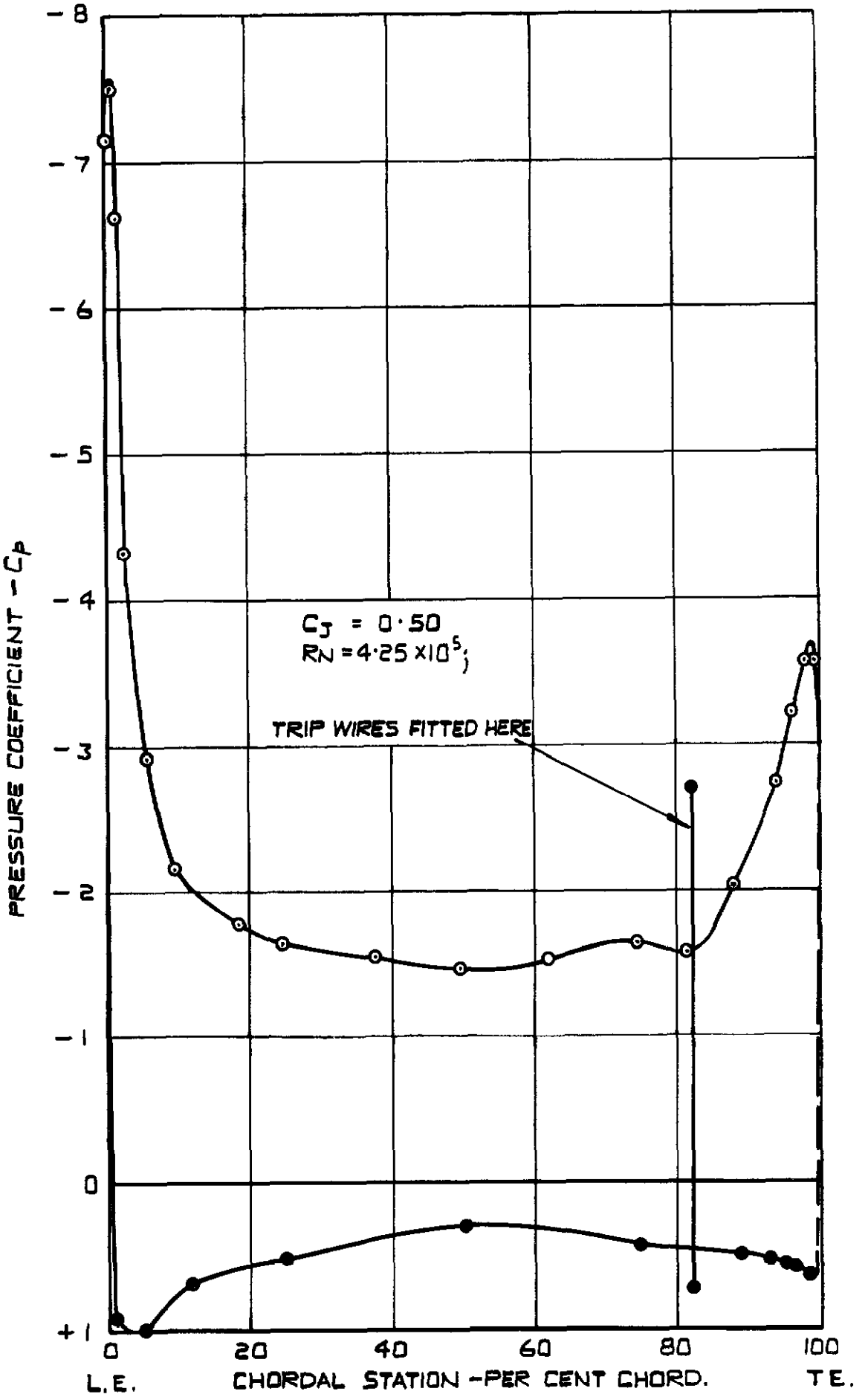

PRESSURE DISTRIBUTION AT ZERO INCIDENCE.

FIG.29

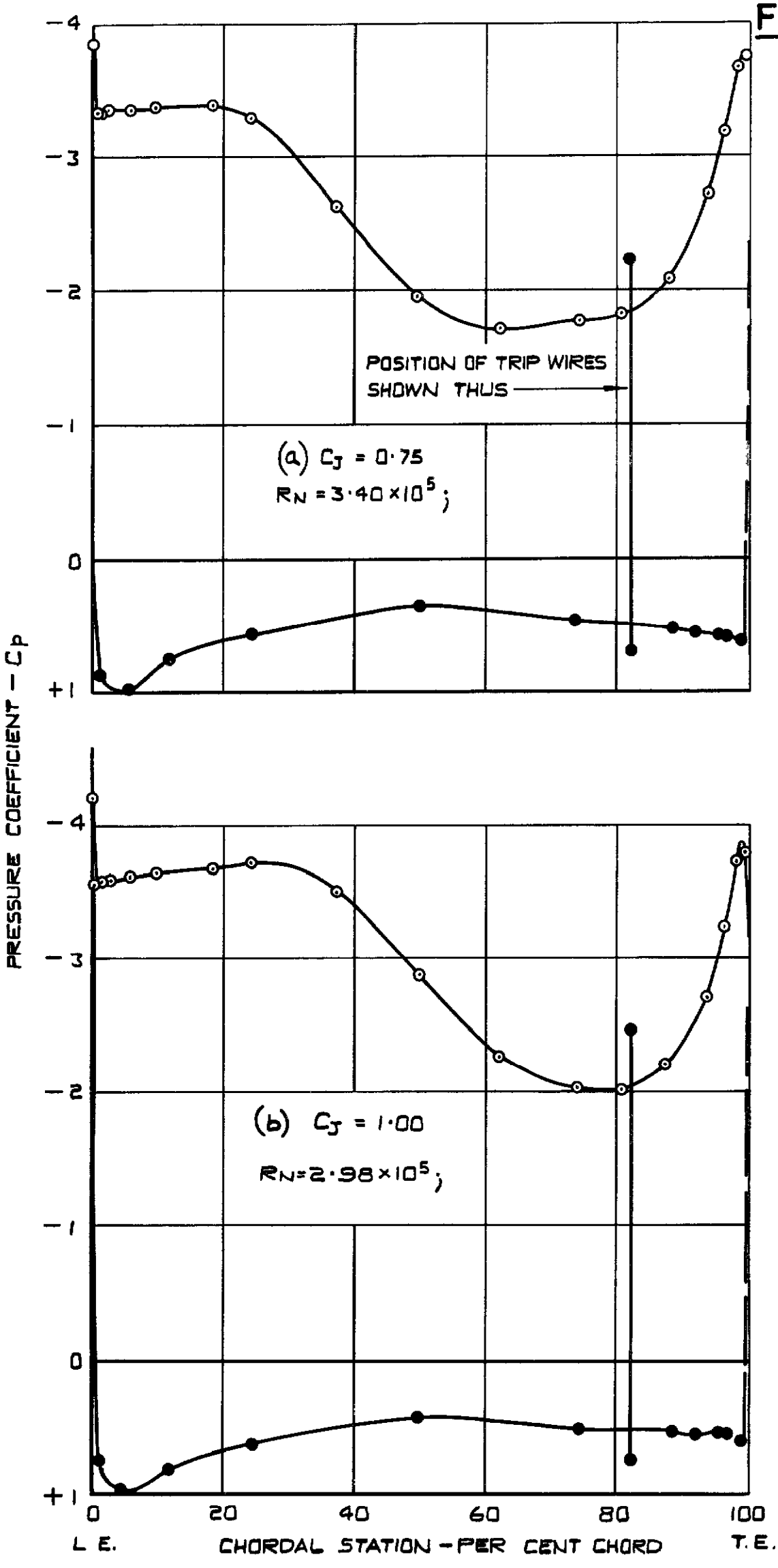

PRESSURE DISTRIBUTION AT ZERO INCIDENCE.

FIG. 30

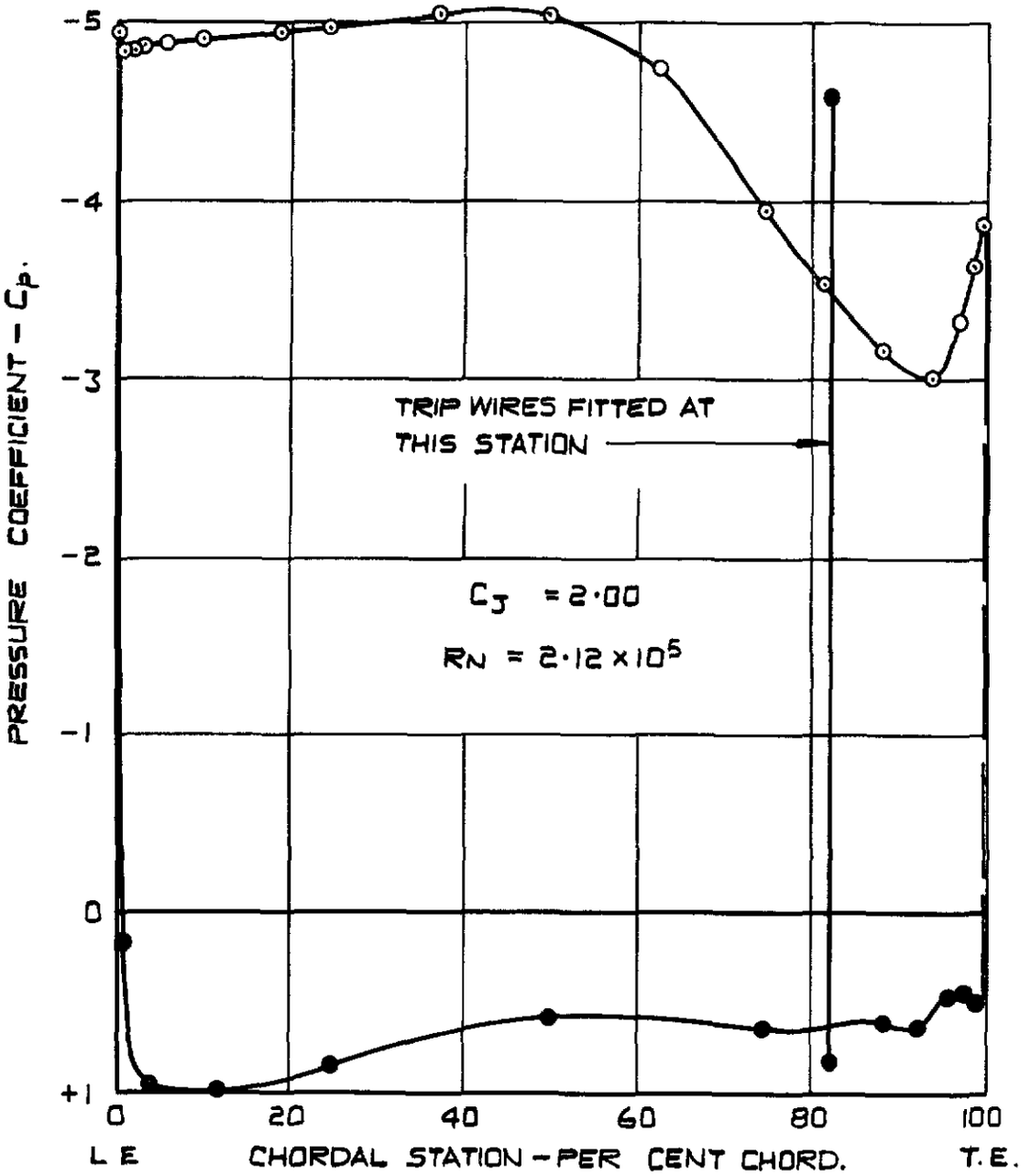

PRESSURE DISTRIBUTION AT ZERO INCIDENCE.

FIG.31

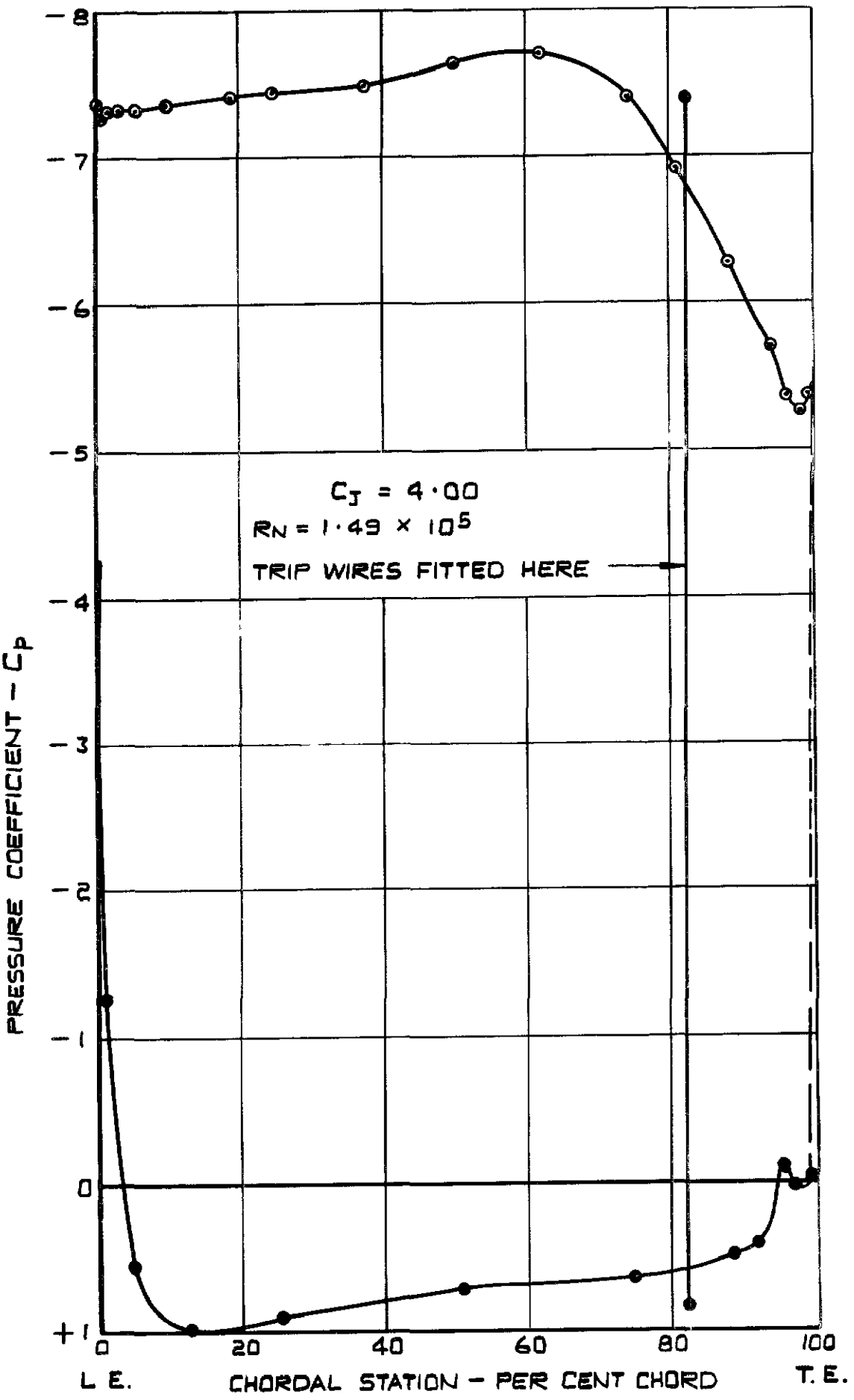

PRESSURE DISTRIBUTION AT ZERO INCIDENCE.

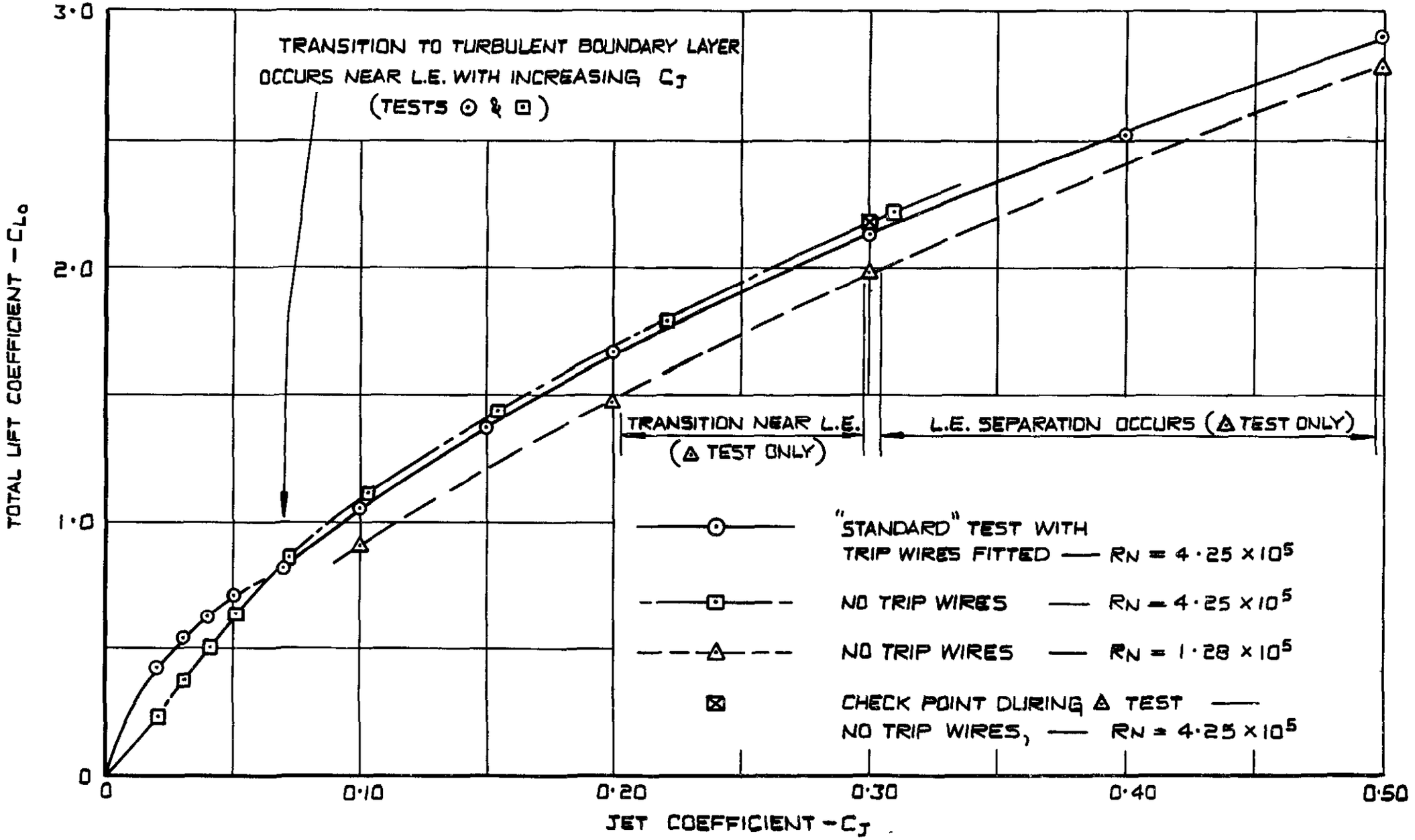

THE EFFECT OF REYNOLDS NUMBER & TRIP WIRES ON C_{L_o}

FIG. 32

FIG. 33

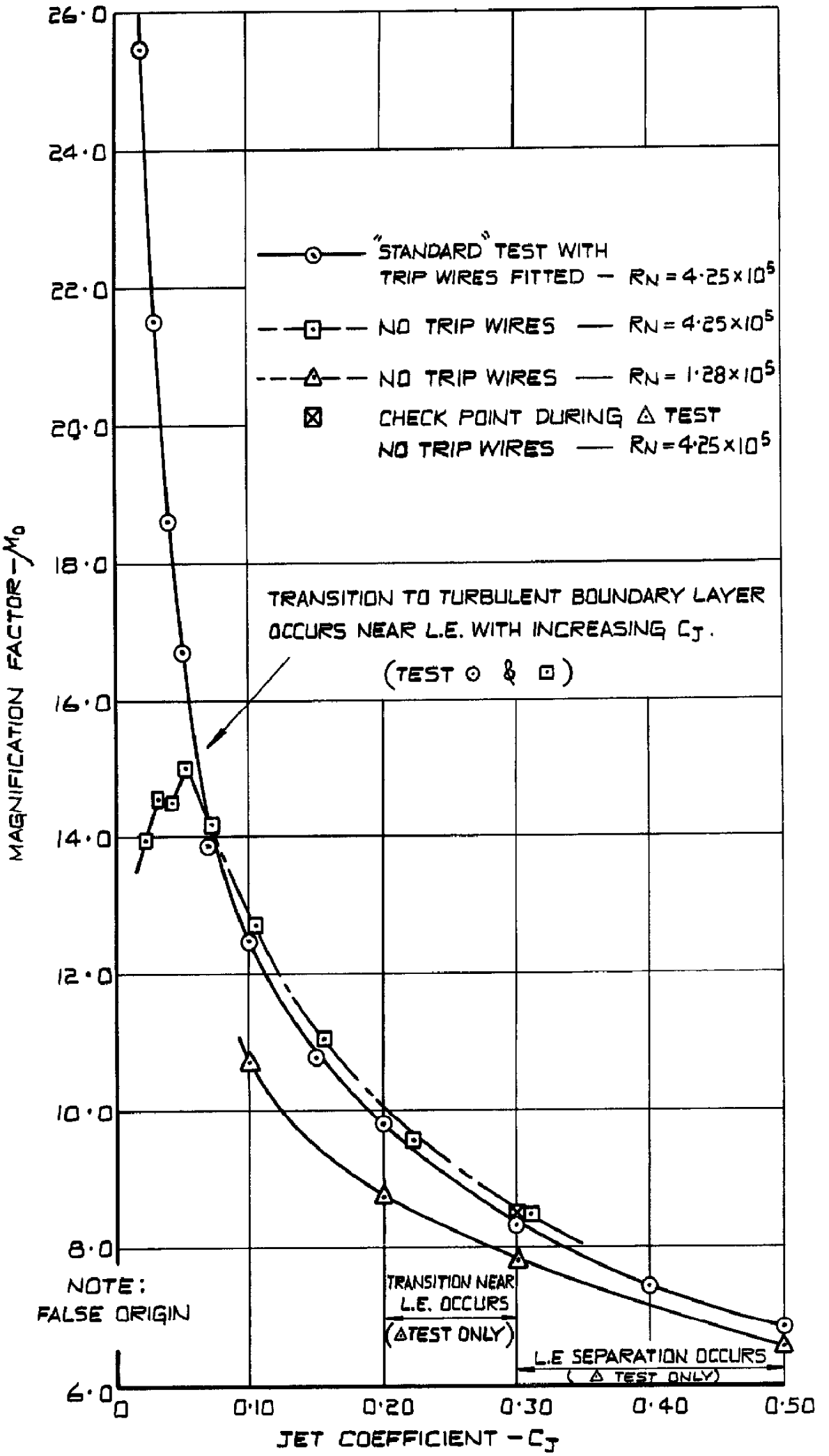

THE EFFECT OF REYNOLDS NUMBER & TRIP WIRES ON M_0

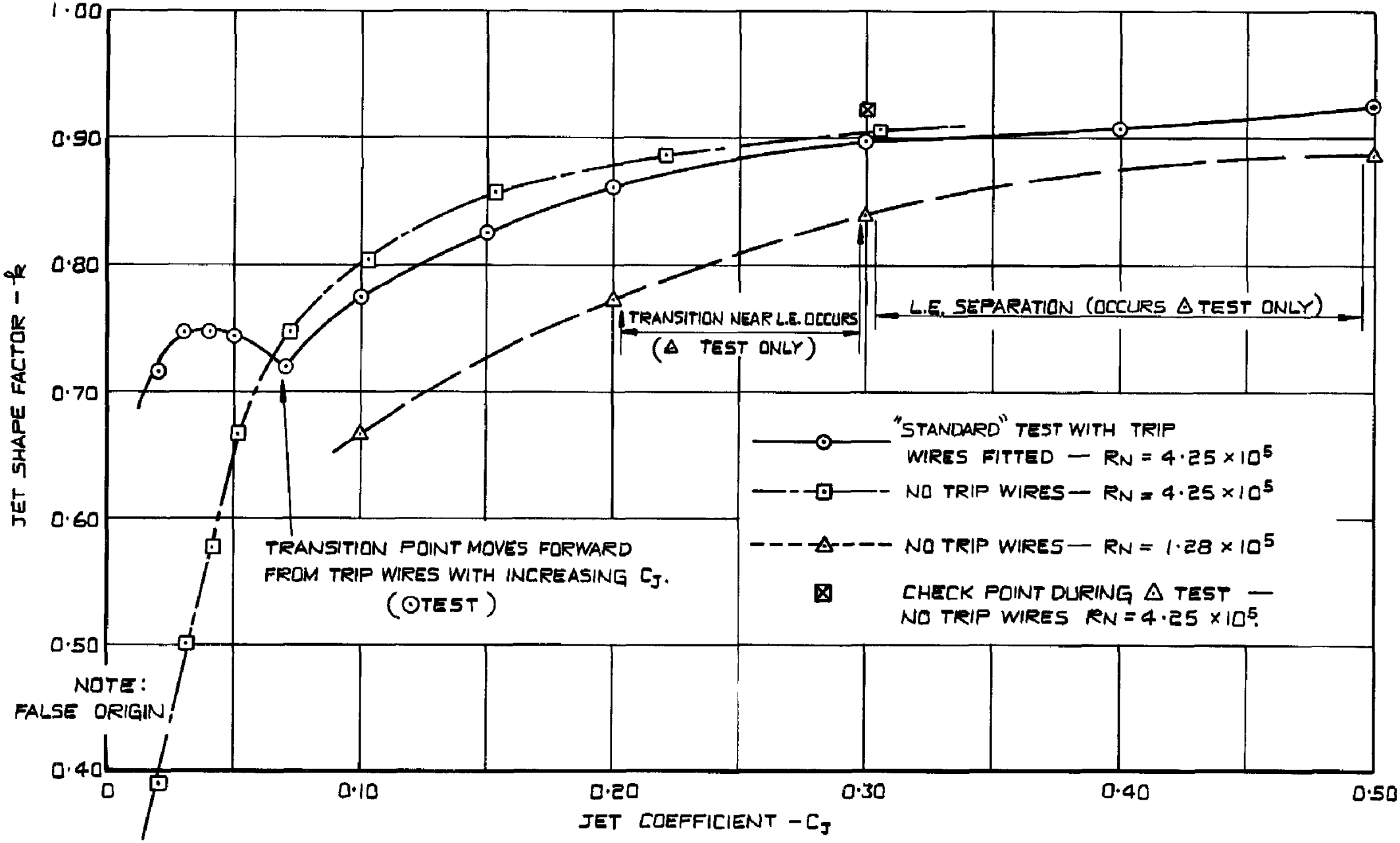

THE EFFECT OF REYNOLDS NUMBER & TRIP WIRES ON k.

FIG. 34

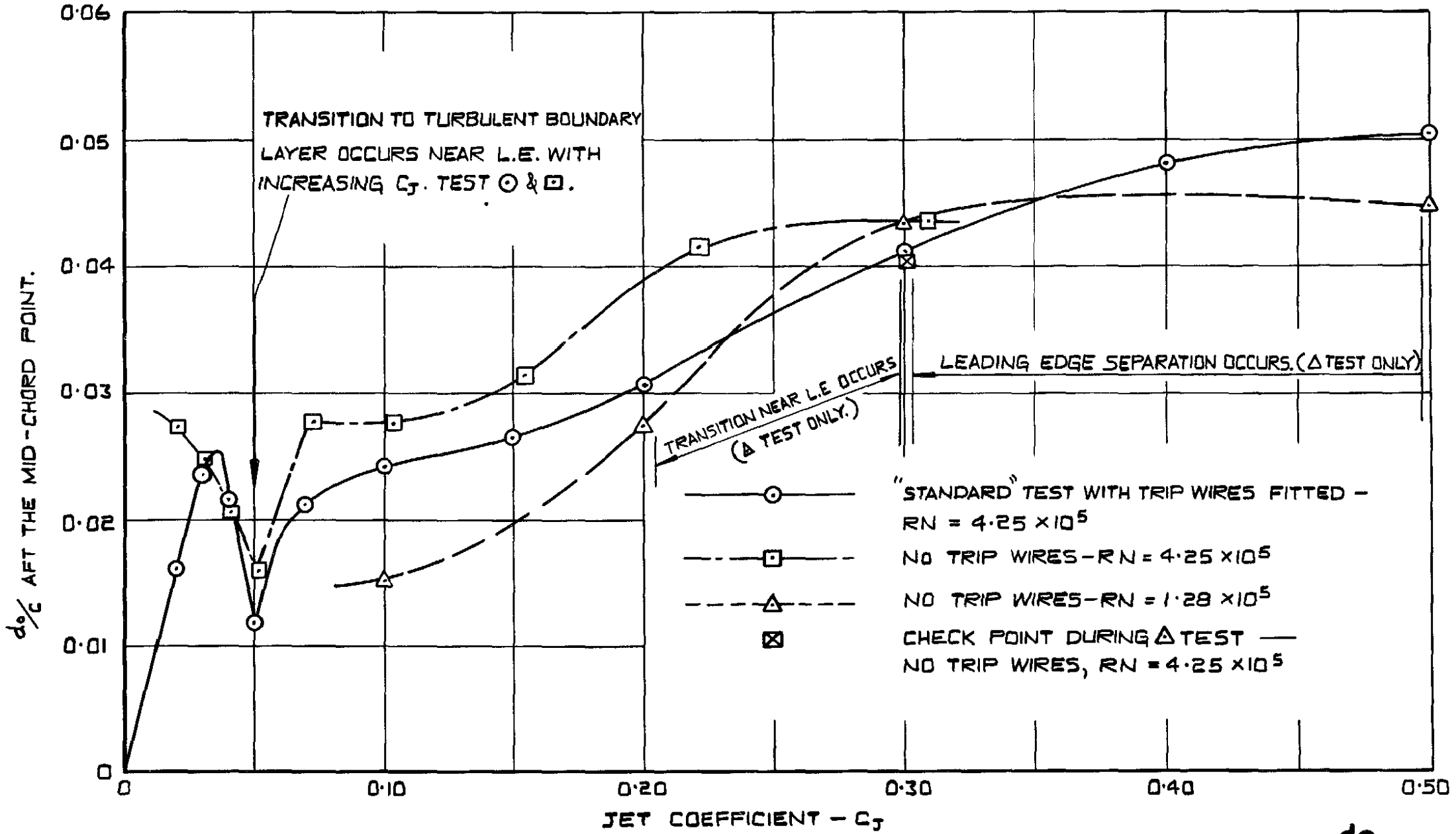

THE EFFECT OF REYNOLDS NUMBER & TRIP WIRES ON $^{do}/_{c}$

FIG 35

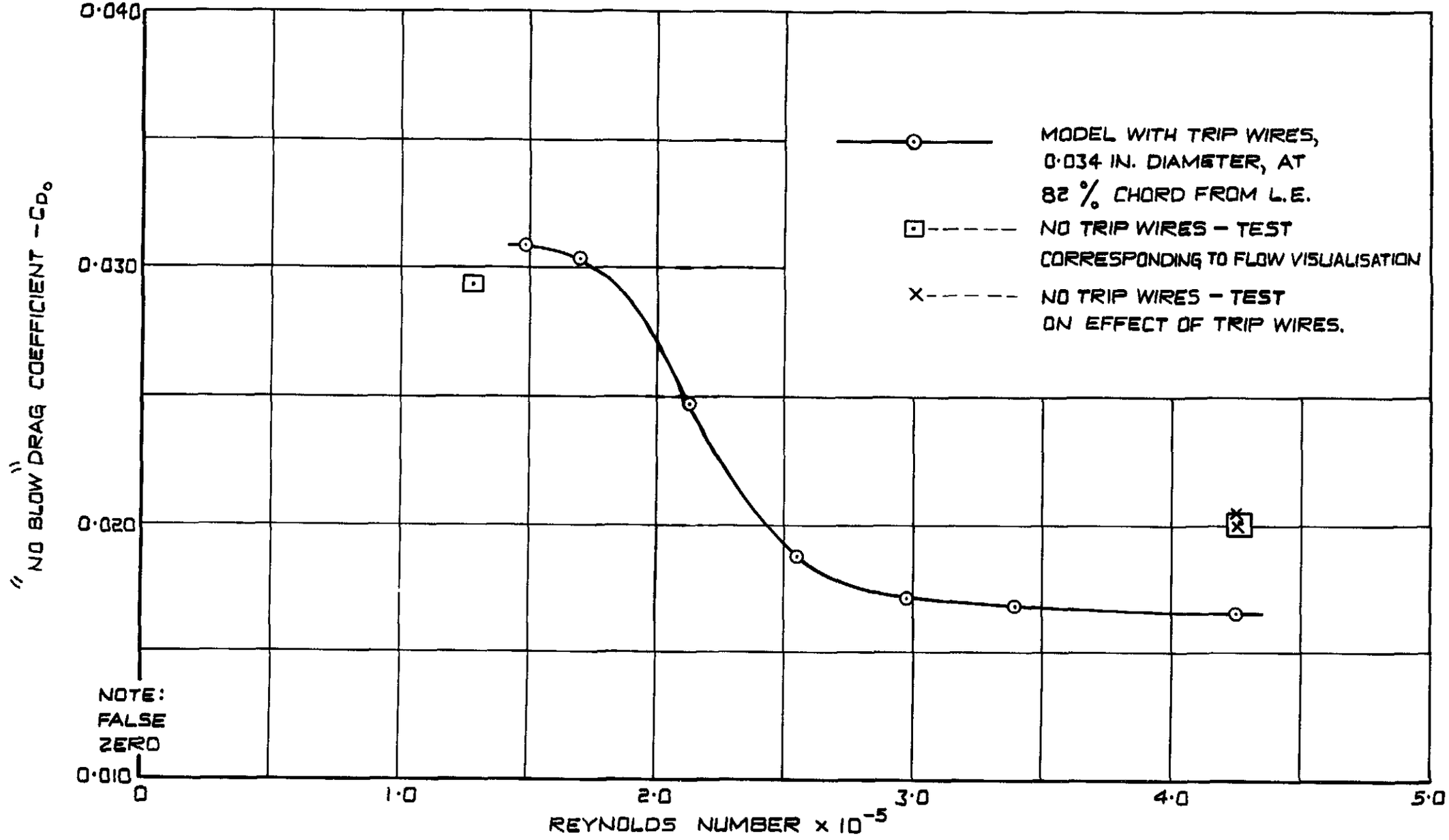

REYNOLDS NUMBER EFFECT ON BASIC MODEL DRAG.

FIG.36

FIG. 37

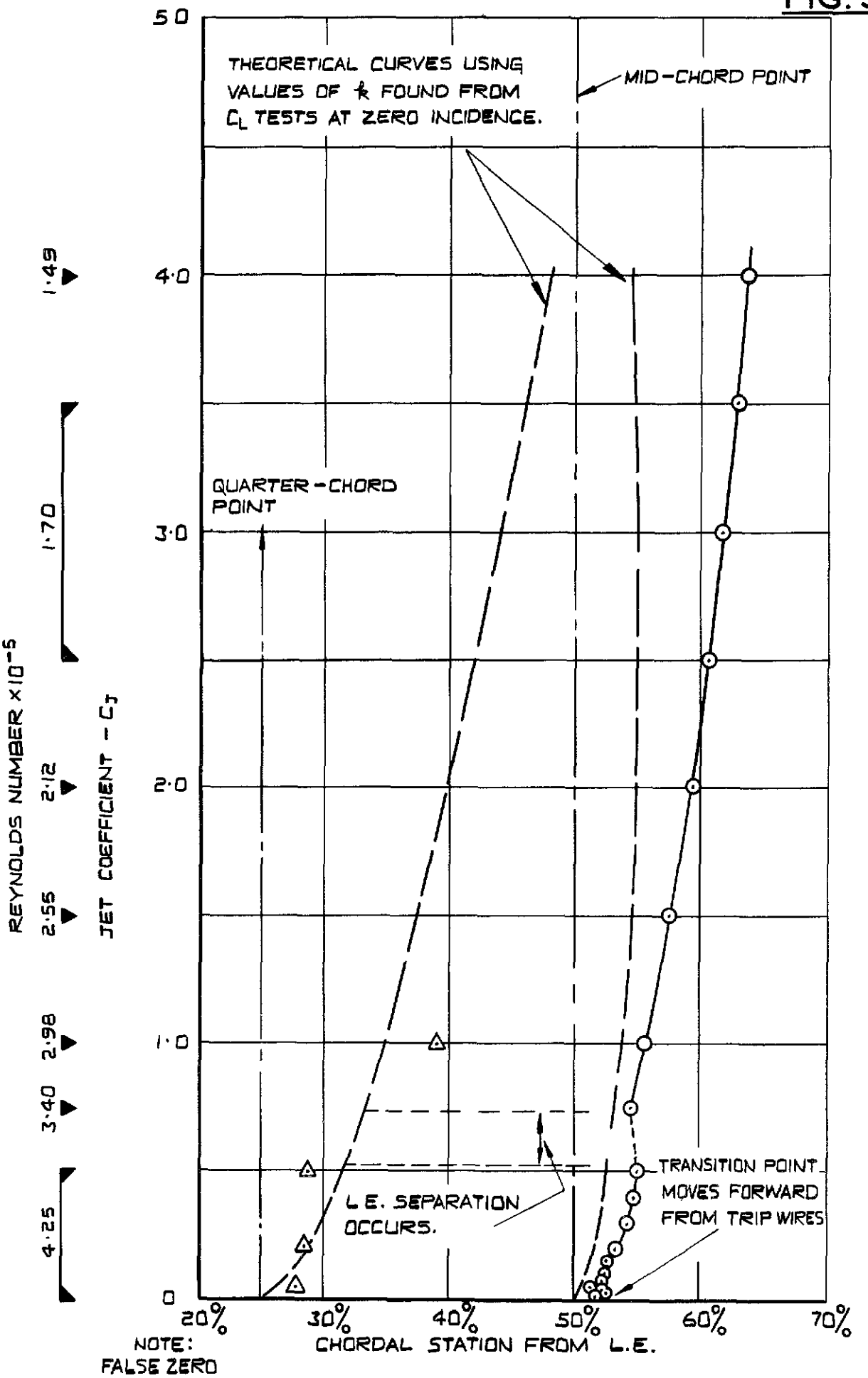

AERODYNAMIC CENTRE AND CENTRE OF LIFT.

FIG. 38

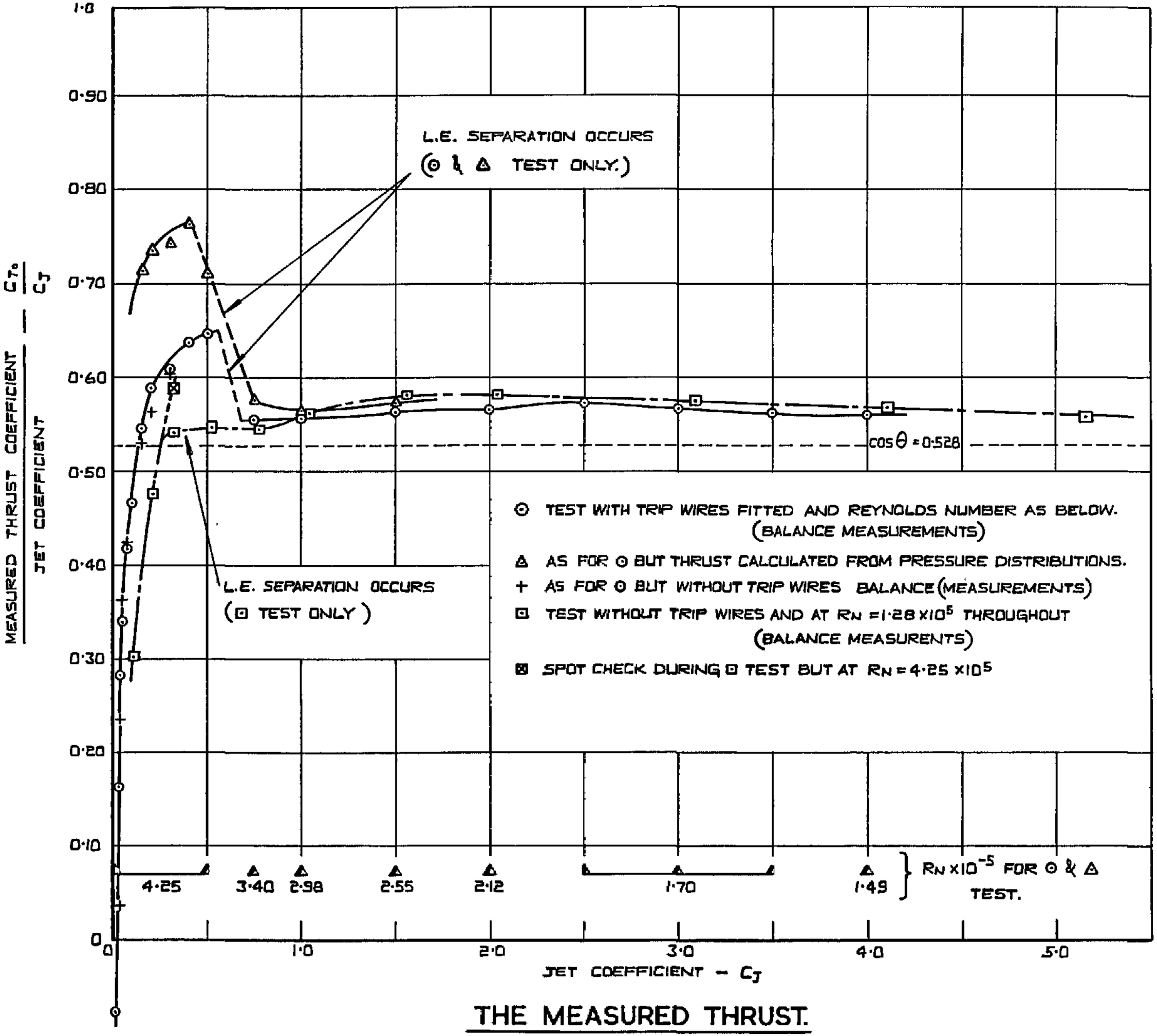

THE MEASURED THRUST.

FIG. 39

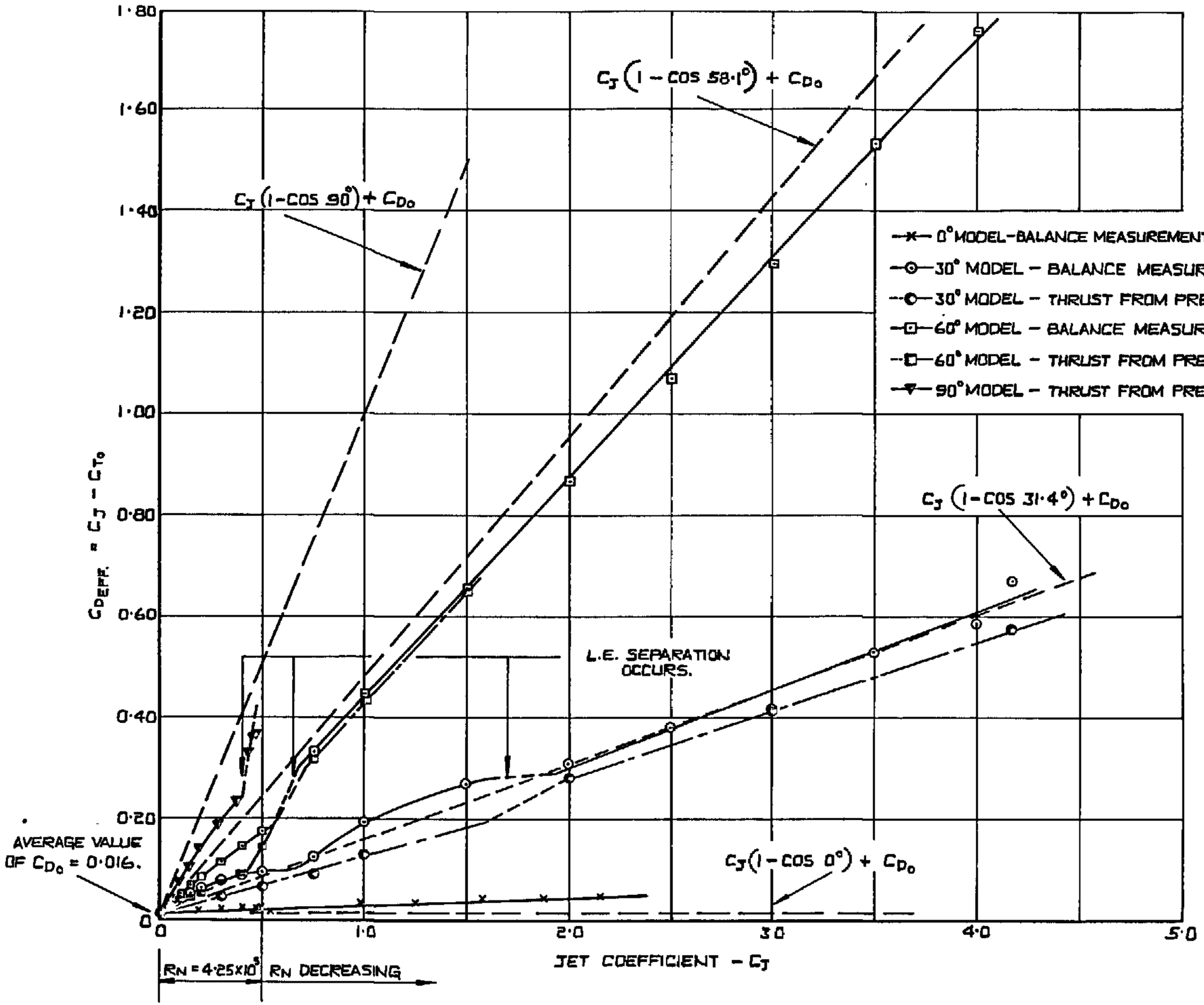

THE EFFECTIVE DRAG COEFFICIENT FOR 0°, 30°, 60°, & 90° MODELS.

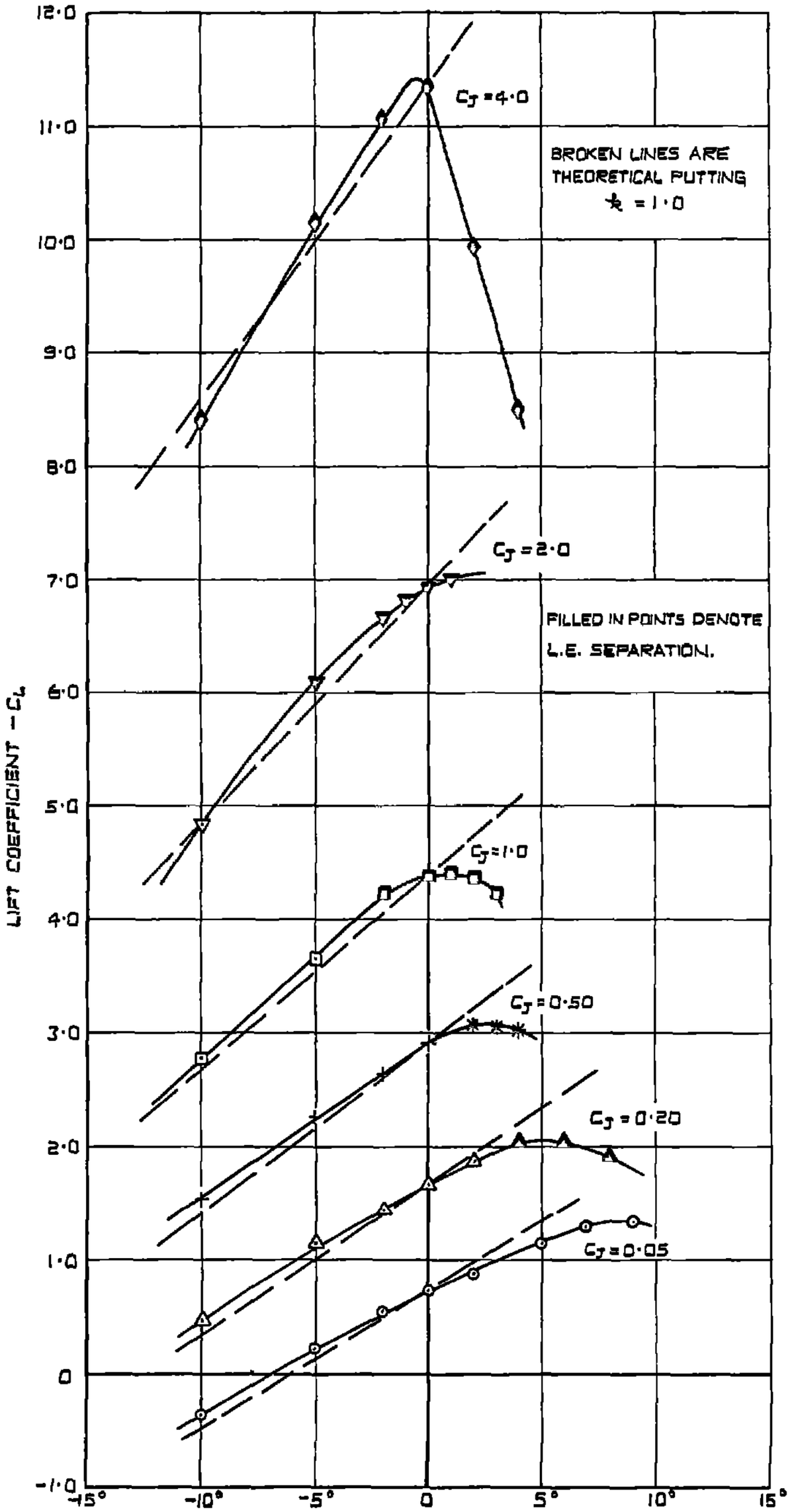

THE LIFT AT INCIDENCE.

FIG. 40

FIG. 41

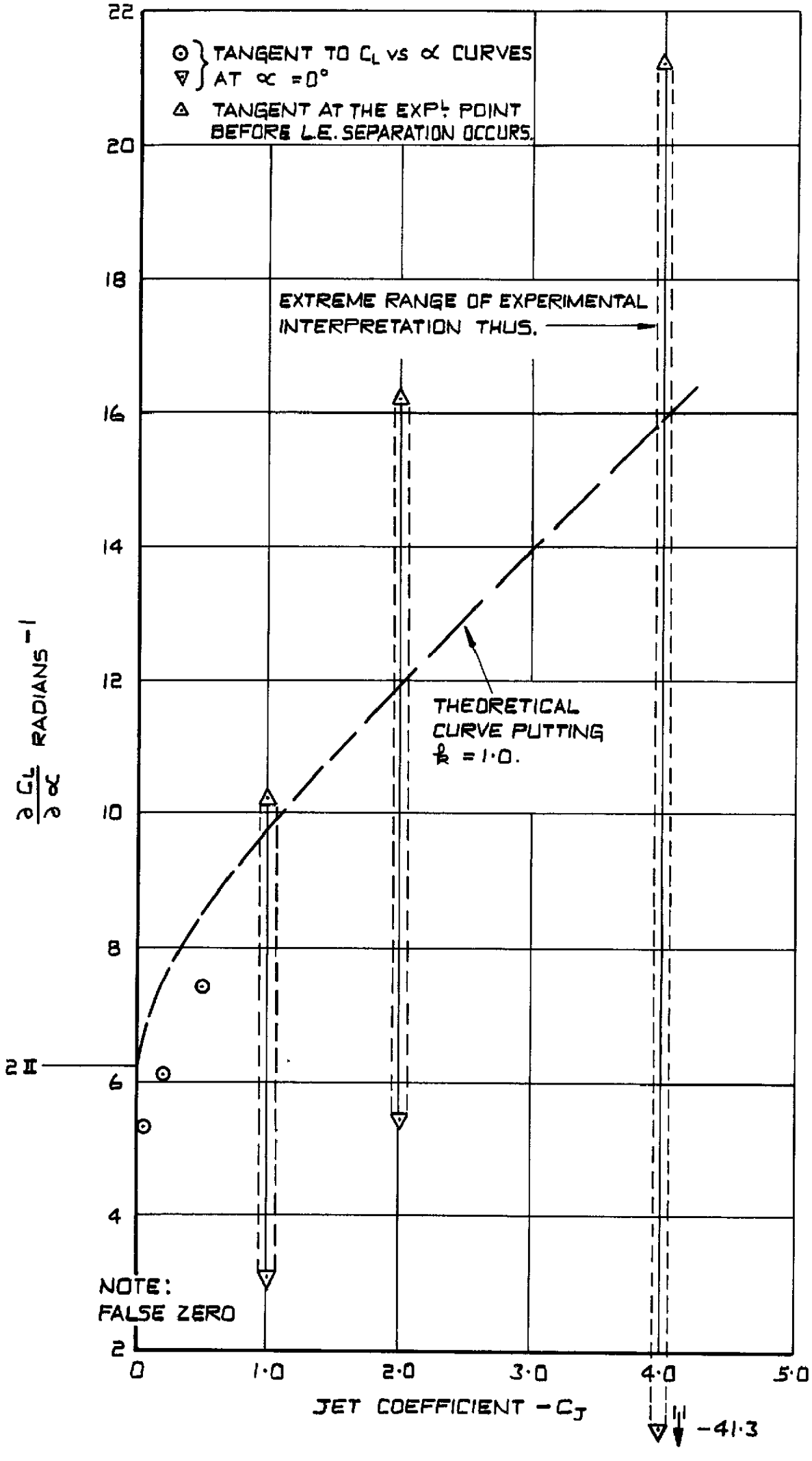

VARIATION OF LIFT CURVE SLOPE WITH C_J.

FIG.42

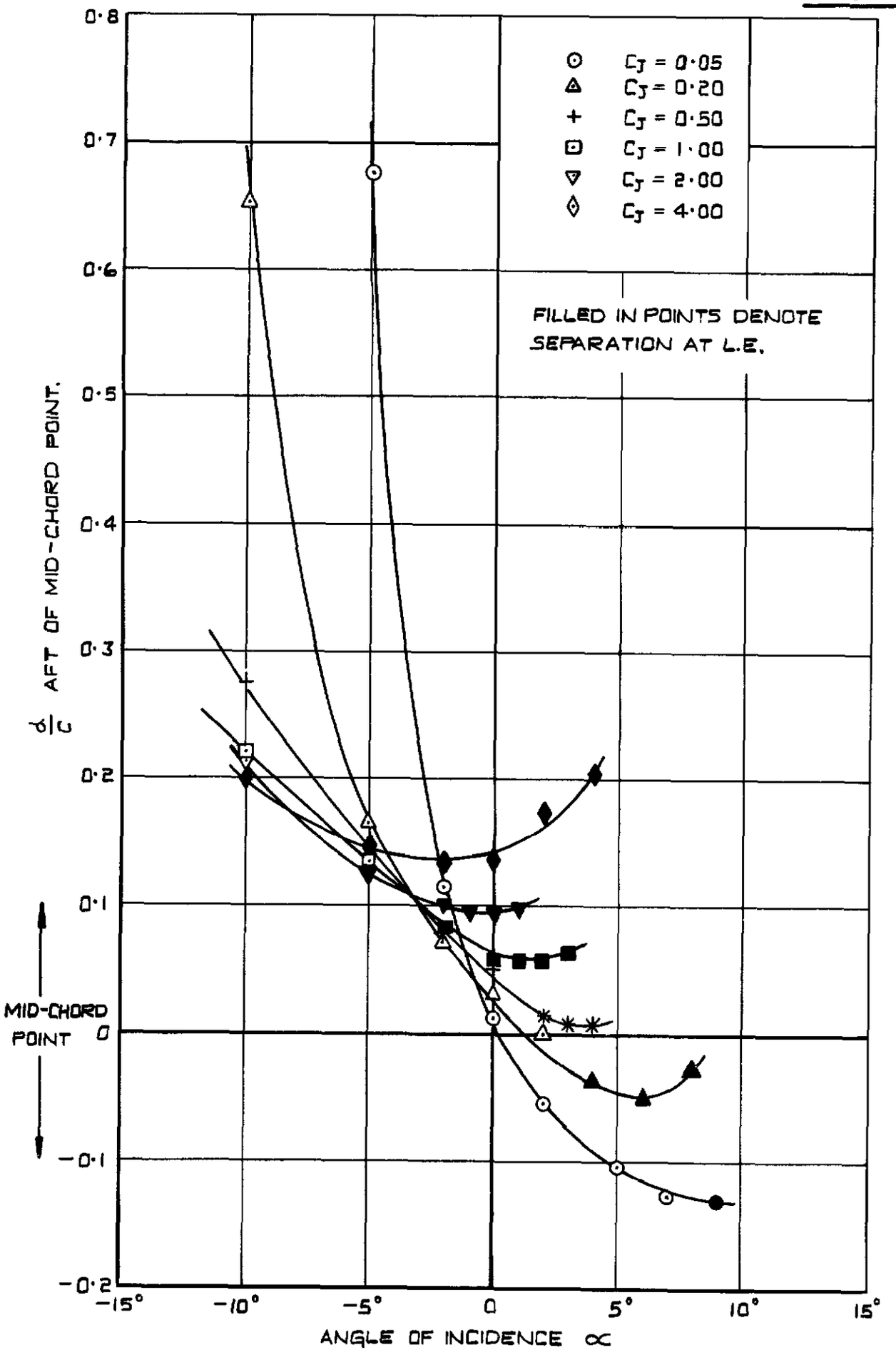

CENTRE OF LIFT – VARIATION WITH INCIDENCE

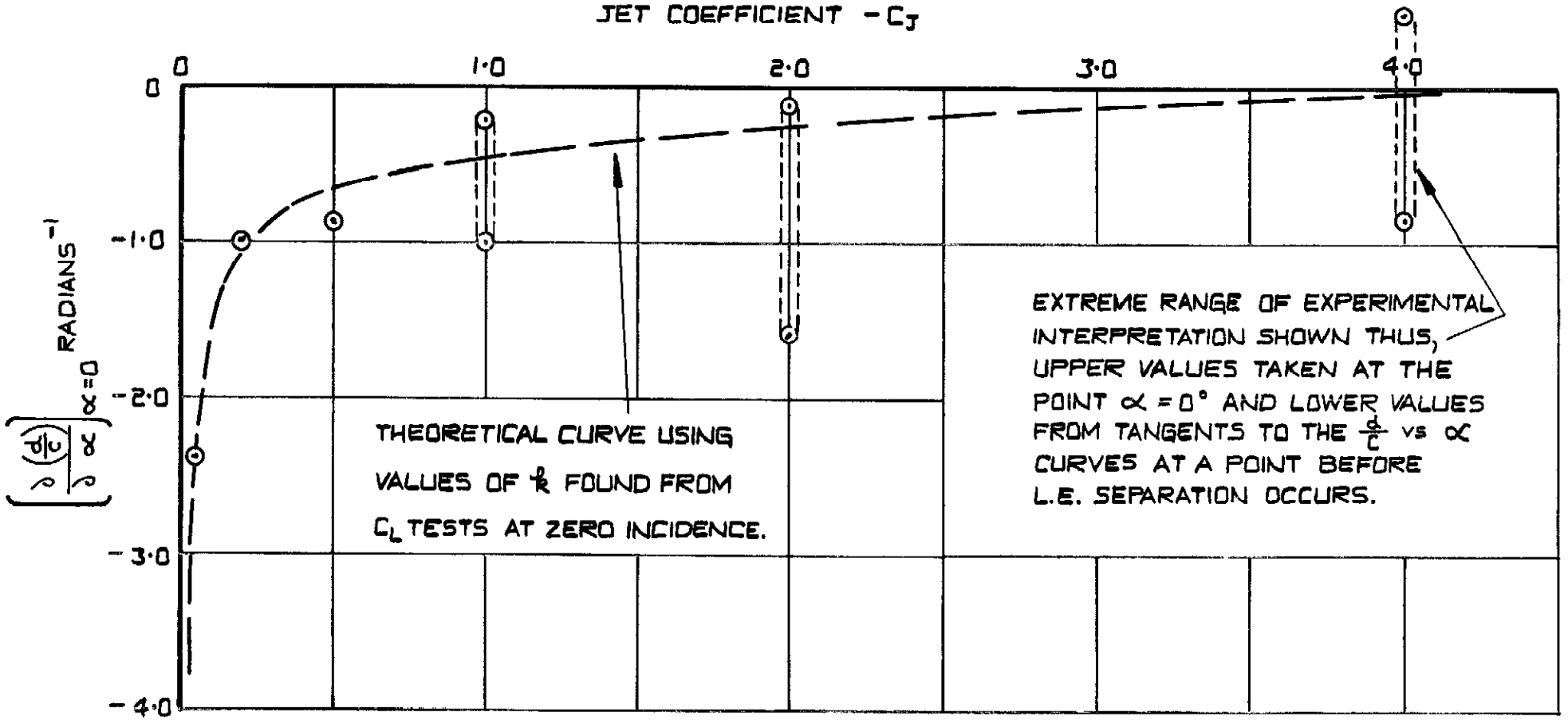

CENTRE OF LIFT MOVEMENT WITH INCIDENCE

FIG. 43

FIG. 44

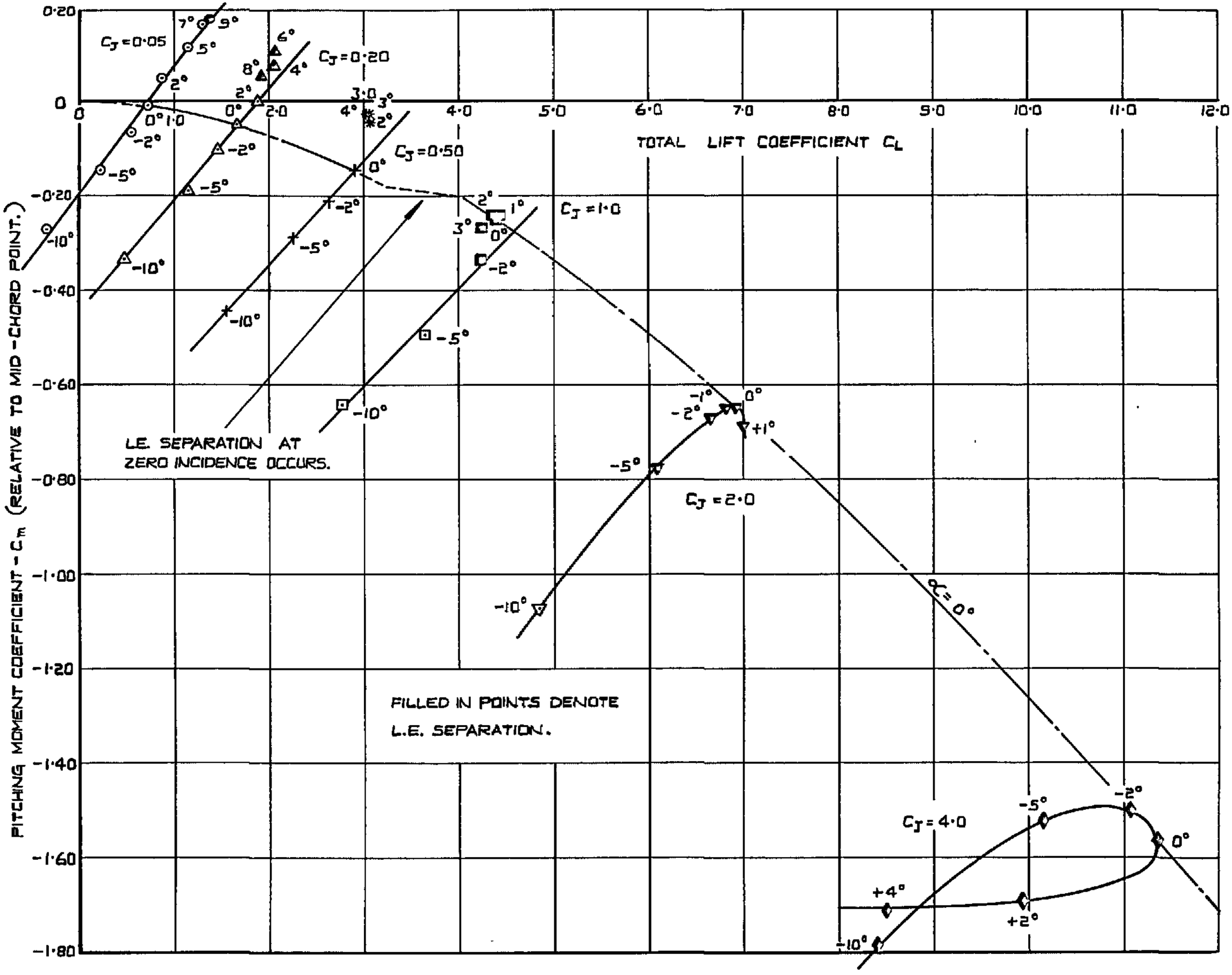

LIFT & PITCHING MOMENT RELATIONSHIP.

FIG. 45

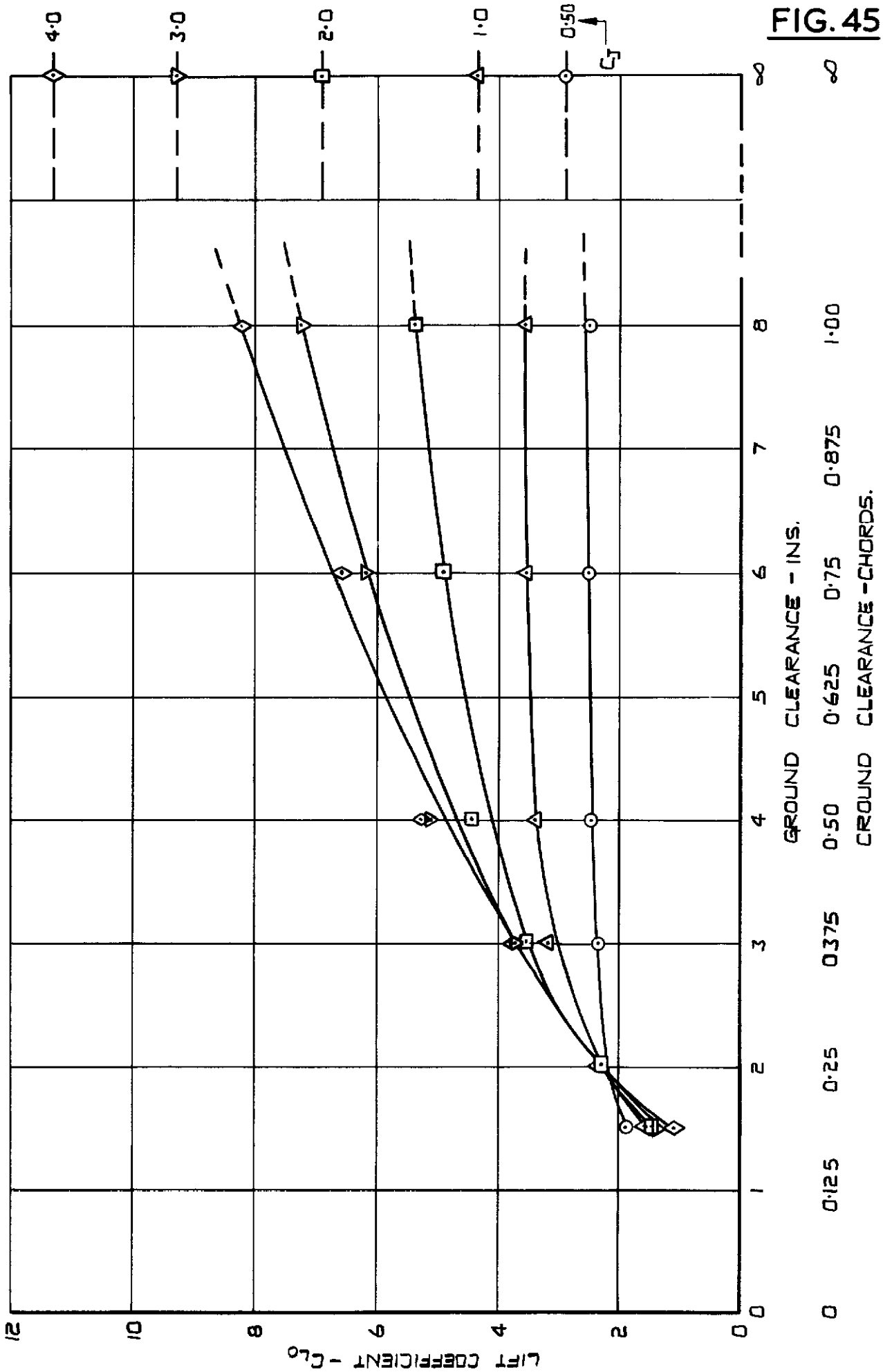

GROUND INTERFERENCE EFFECT ON LIFT COEFFICIENT AT ZERO INCIDENCE

FIG. 46

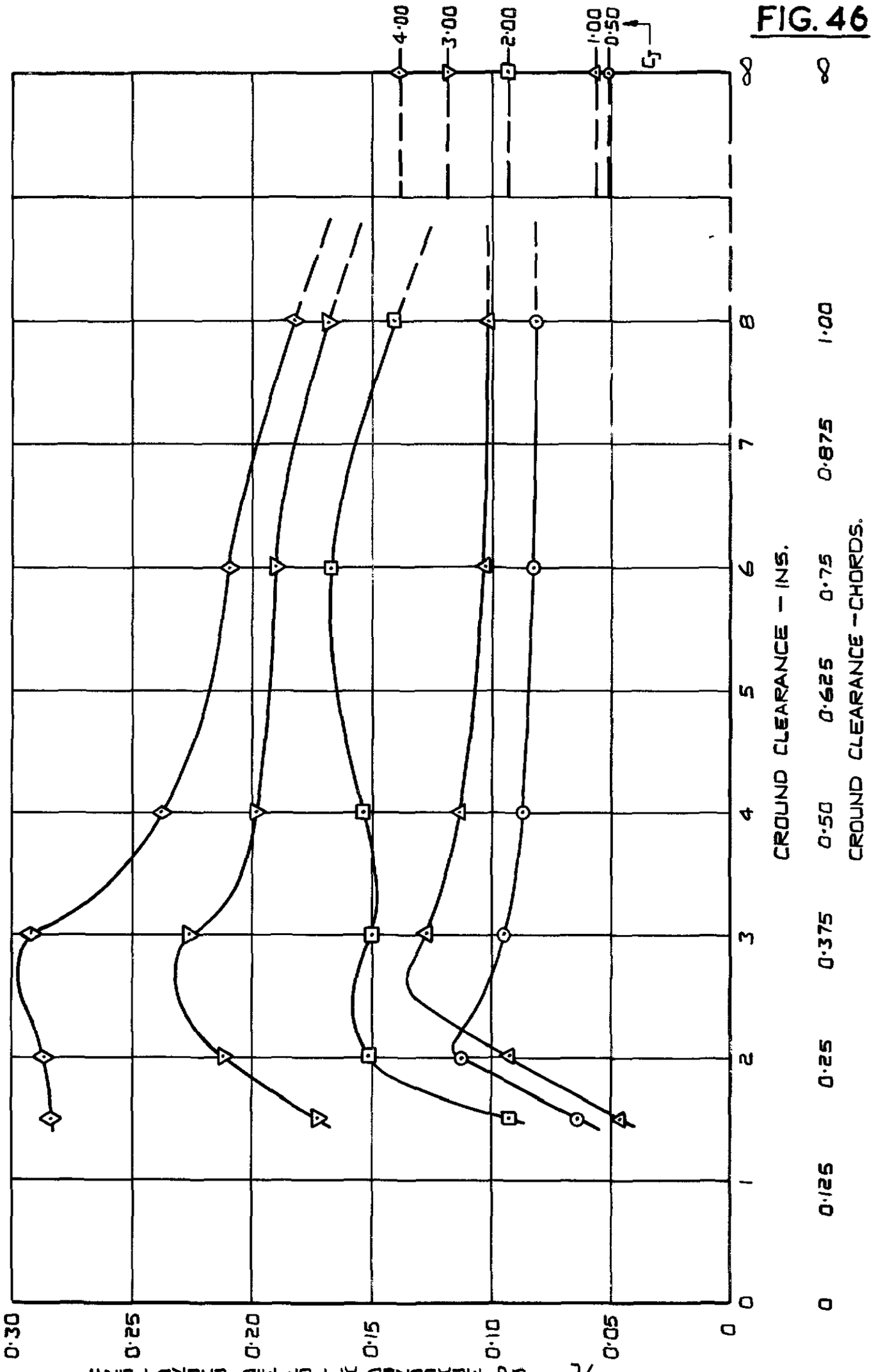

GROUND INTERFERENCE EFFECT ON CENTRE OF LIFT POSITION AT ZERO INCIDENCE.

FIG. 47

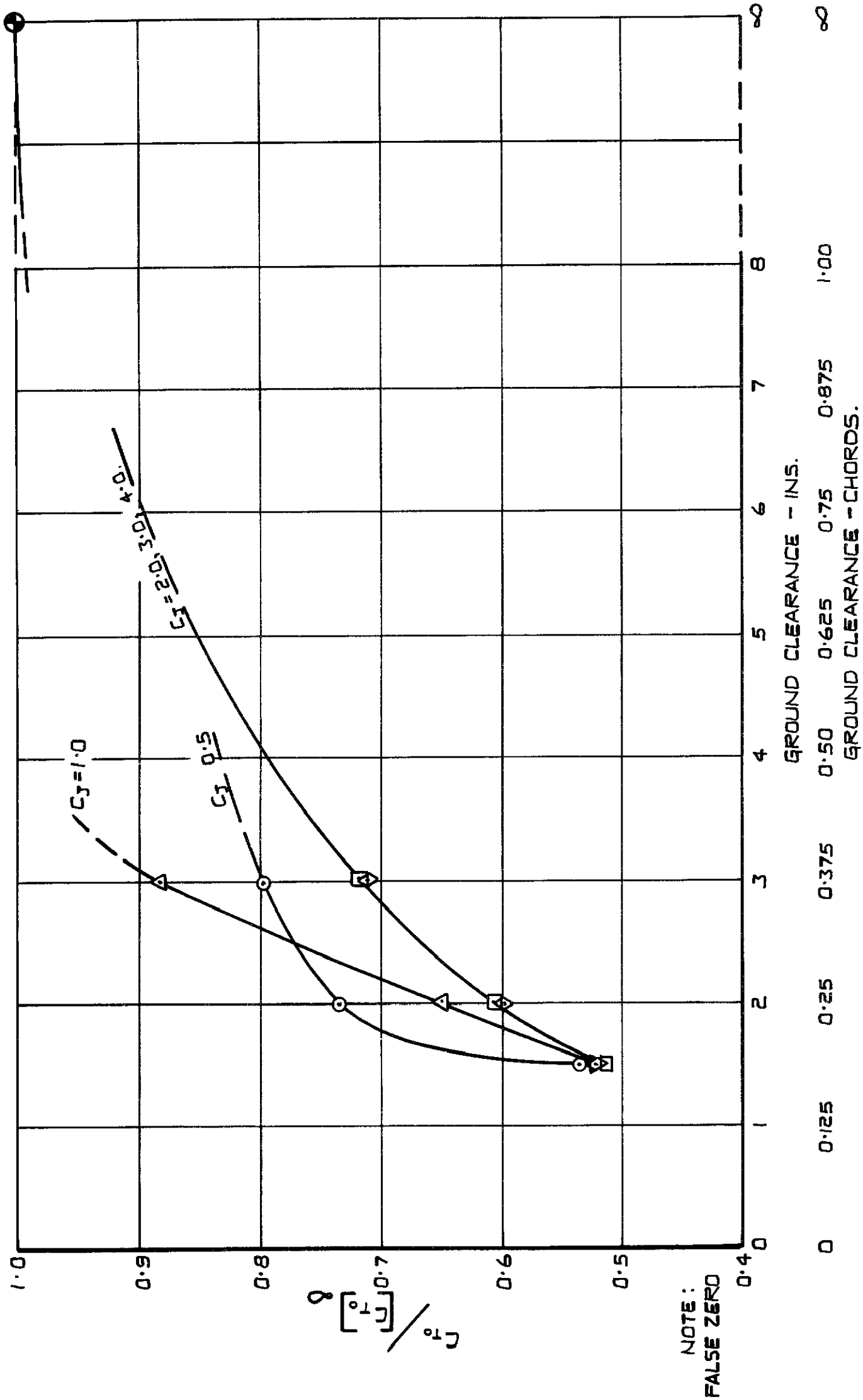

GROUND INTERFERENCE EFFECT ON THRUST.

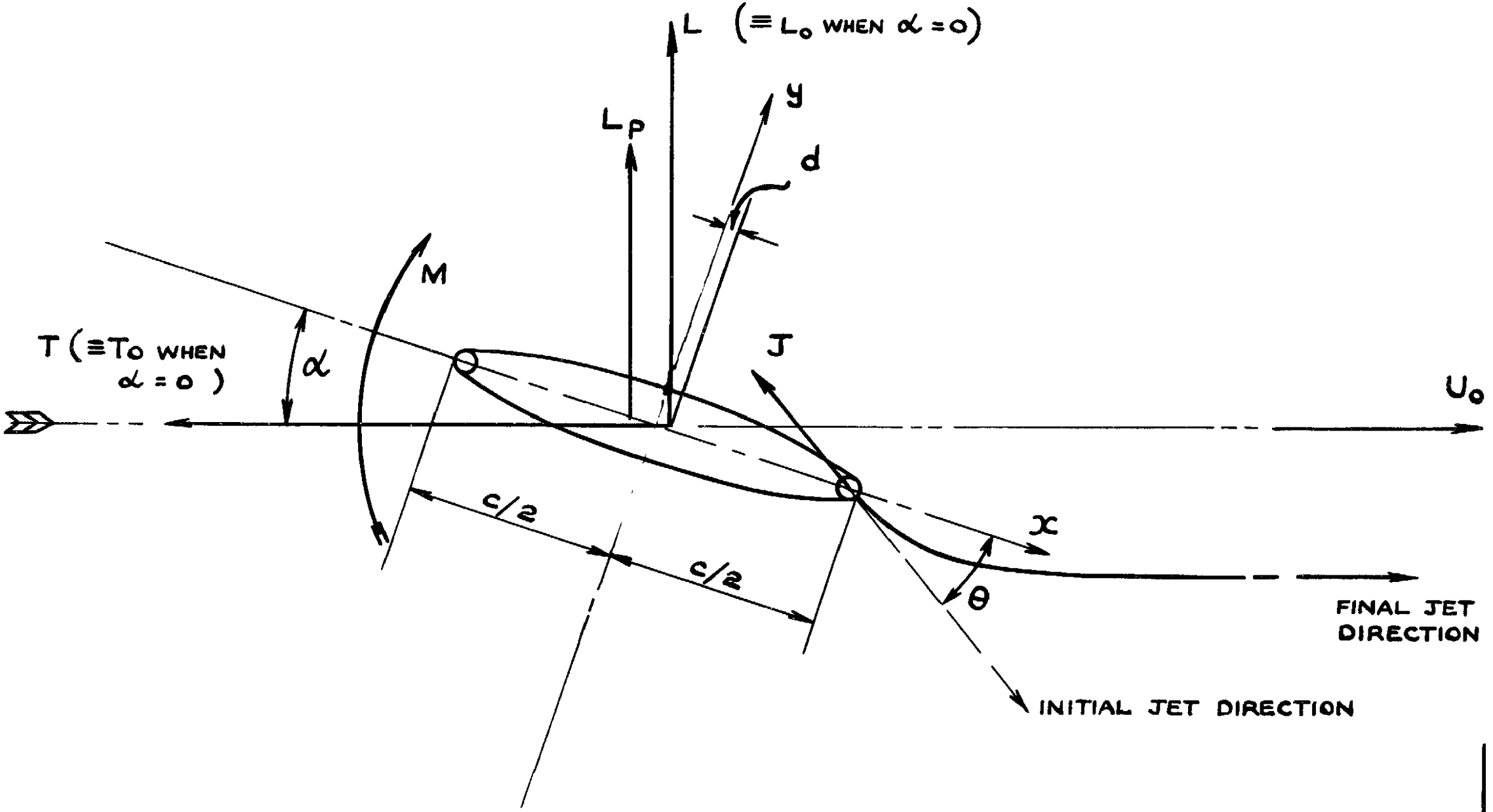

FIG. 48

NOTATION — SEE ALSO APPENDIX I

Printed and published by
HER MAJESTY'S STATIONERY OFFICE

To be purchased from
York House, Kingsway, London W.C.2
423 Oxford Street, London W.1
13A Castle Street, Edinburgh 2
109 St Mary Street, Cardiff
39 King Street, Manchester 2
Tower Lane, Bristol 1
2 Edmund Street, Birmingham 3
80 Chichester Street, Belfast
or through any bookseller

Printed in Great Britain

S.O. Code No. 23-9010-45